ISSN 1349-113X
JAXA-SP-05-035E

JAXA Special Publication

Computational Fluid Dynamics of Multiphase Flows in Solid Rocket Motors

Toru SHIMADA, Yu DAIMON, and Nobuhiro SEKINO

March 2006

Japan Aerospace Exploration Agency

Computational Fluid Dynamics of Multiphase Flows in Solid Rocket Motors

By

Toru SHIMADA*, Yu DAIMON*,
and
Nobuhiro SEKINO**

Abstract : This booklet provides practical information on the computational fluid dynamics of the multiphase flows in solid rocket motors with descriptions of mathematical modeling, simulation methods, computer codes, and many numerical experiments. Combustion flows of metallized composite propellants in solid rocket motors are multiphase flows consisting of particles and gas. In this booklet, descriptions are given concerning the mathematical modeling of the gas-particle interaction and its sensitivity on various parameters, simulation methods of gas-particle multiphase flows, such as, the Eulerian-Eulerian, the Eulerian-Lagrangian, and the Eulerian-hybrid methods, and the modeling method of combustion and breakup of particles, and so on. Computer programs, SPECS (Solid Propulsion Enhanced Code Series), coded along with these techniques are also introduced to the readers. Moreover, many examples of numerical experiments are provided on the verification of the mathematical modeling and numerical methods.

Key words : Computational fluid dynamics, Multiphase flow, Solid rocket motor

Nomenclature

A, B	=	coefficients in phase-interaction term in Eulerian-Eulerian method
A', B'	=	coefficients in phase-interaction term in Eulerian-Lagrangian method
$\mathbf{A}$, $\mathbf{B}$	=	Jacobian matrices of convection fluxes in i- and j-directions, respectively
$\hat{\mathbf{A}}$, $\tilde{\mathbf{A}}$	=	Jacobian matrices
$A_{i,j}$	=	cell-projected area
A_t	=	throat area
A_b	=	burning surface area
c^*	=	characteristic discharge velocity
c_p	=	specific heat of gas at constant pressure
c_v	=	specific heat of gas at constant volume
C_c	=	slip coefficient of Cunningham
C_D	=	drag coefficient
C_{D0}	=	incompressible drag coefficient

* Japan Aerospace Exploration Agency
** IHI Aerospace Co., Ltd.

C_{pp} = specific heat of particle
D = diameter
D_{43}, D_m = mass-averaged particle diameter
D_p = particle diameter
D_t = throat diameter
$\mathbf{E}, \mathbf{F}, \mathbf{G}$ = convective flux vectors
e = total energy per unit volume, or base of natural logarithm
e_n = internal energy per unit volume
$\vec{f}$ = force vector acting on a particle
$\vec{F}$ = force vector acting on particles per unit volume
$\vec{F}_C$ = contact force between particles
$\vec{F}_D$ = fluid dynamic force
$\vec{F}_G$ = gravity and inertial force
h = heat transfer coefficient
H = total enthalpy
I = unit matrix
k_B = Boltzmann constant
Kn = Knudsen number
ℓ = mean particle distance
L = reference length, characteristic length of flow
m = mass
$\dot{m}$ = mass flow rate, mass change rate due to combustion per particle per unit time
M = Mach number
$\tilde{M}$, = mean molecular weight
M_g = molecular weight
M_k = total mass of particles in k-th particle group
M_{prop} = propellant mass
M_p = total mass of particle
$\vec{n}$ = normal vector
n_p = particle number density
N_p = number of particle phases in Eulerian-Eulerian method, or number of representative particles (groups) in Eulerian-Lagrangian method
N_{Tk} = total number of real particles represented by the k-th representative particle
Nu = Nusselt number
p, q = computation space local coordinates
p = static pressure
Pr = Prandtl number
q = heat transfer to a single particle from gaseous phase
$\mathbf{Q}$ = vector of conserved variables
Q = energy amount received by the particle-phase per unit volume from gaseous phase
Q_C = convective heating
$Q_{C,nu}$ = non-uniformity contribution in convective heating
Q_R = radiative heating
r = radial coordinate

$\dot{r}_b$ = linear burning rate
r_p = radius of particle
R = gas constant, or initial distance between particle and vortex center
$\tilde{R}$ = universal gas constant
$\bar{R}$ = effective gas constant of phase-equilibrium gas-particle flow
Re = Reynolds number
S = surface area
$\mathbf{S}$ = source term vector
S_{ref} = projected area of sphere
S_{sur} = surface area of sphere
St = Stokes number
T = temperature
T_f = film temperature
t = time
t_{cr} = residence time of particle in nozzle
u = velocity component in x direction
$\vec{U}_s$ = slip velocity
$\vec{u}$, $\vec{U}$ = velocity vector
v = velocity component in y direction
V = volume
$Vol_{i,j}$ = volume of cell
w = velocity component in z direction
$\dot{w}$ = mass generation of the Eulerian-phase alumina due to combustion of the Lagrangian-phase aluminum droplet
We = Weber number
We_c = critical Weber number
X = molar fraction of chemical species
Y_{Al} = aluminum mass fraction

∇_I, ∇_J = backward differences in i- and j-directions, respectively
α = volume fraction, or aluminum mass fraction in propellant
α_g = thermal diffusivity
β = mass fraction of alumina in initial large droplet
χ = ratio of gas density to true density of particle
δ = average particle distance, or shape factor of distribution function
Δ_I, Δ_J = forward differences in i- and j-directions, respectively
ε = total energy per unit mass
ε_p = total energy of particle phase per unit mass, or emissivity of particle
ϕ = ratio of speed of particle to that of gas, or probability density function of particle diameter, or volume fraction of alumina in a particle
γ = specific heat ratio of gas
$\bar{\gamma}$ = effective specific heat ratio of phase-equilibrium gas-particle flow
κ = ratio of specific heat of particle to that of gas
λ = thermal conductivity of gas

ρ = density
ρ_{Al} = aluminum bulk density in the Eulerian phase
σ = Stefan-Boltzmann constant, or variance
σ_{Al} = true density of aluminum
$\sigma_{Al_2O_3}$ = true density of alumina
σ_m = particle true density
σ_p = propellant density
σ_t = surface tension of droplet
μ = gas viscosity coefficient
ν = kinematic viscosity
ν_A, ν_B = spectral radii of A and B, respectively
ν_S = spectral radius
π = the ratio of a circle's circumference to its diameter
θ = angle
$\bar{\tau}$ = stress tensor
τ_f = characteristic flow time
τ_V = velocity-relaxation time
τ_T = temperature-relaxation time
ω = angular velocity
Ω = inspection volume
ψ = loading ratio (=ratio of particle bulk density to gaseous-phase density), or ratio of aluminum mass in alumina cap which finally remains after combustion to all aluminum mass in propellant
Ψ = rate of particle temperature to gas temperature

Subscript

0 = initial, or incompressible
b = burning surface
c = combustion chamber
m = particle material
g = gas
i, j = index for grid points
L = left-side at cell interface
n = normal direction
p = particle
R = right-side at cell interface
t = throat, or tangential direction
∞ = free stream

Superscript

$*$ = critical value
k = k-th particle group
n = number of time step, or exponent of particle combustion model
T = transposed matrix

Contents

1. Introduction

The understanding of flow phenomena of gases and particles inside solid-propellant rocket motors (SRM) is very important in the design of SRM from various standpoints. It is essential to the understanding and the prediction of acoustic instabilities and erosive burning in SRM that the burning rate responds to the pressure and the velocity of combustion gas flow. The information on the internal flow properties is therefore required to assess these combustion characteristics. Such information is also necessary as thermal and mechanical boundary conditions in the thermal stress analyses of the propellant grain. Meanwhile, in order to estimate the ablating surface recession rate of thermal protection system (TPS) materials, it is required to know diffusion velocities of mass and heat across the boundary layer, as well as impinging particle influx. The propulsion performance is evaluated and optimization of nozzle contour is conducted putting together the above-mentioned aspects.

1.1. Combustion of Metallized Composite Solid Propellant

In this study we deal with a type of composite solid propellant consisting of ammonium perchlorate (AP), aluminum, and hydroxyl-terminated polybutadiene (HTPB). Such composite propellant is a complex material of which oxidizer particles (AP) and metal fuel (aluminum) are cured with polymerization of fuel-binder material (HTPB). The most fundamental portion of solid-propellant combustion is that of such an inhomogeneous system, and is very complicated physico-chemical phenomenon. The combustion products of AP/HTPB/Al composite propellant typically make the mass fraction structure shown in Fig. 1. The Al_2O_3 shows the value exceeding 30% due to its large molecular weight and it is still about 8% of a molar fraction.

The mechanism of combustion of metallized propellants has been studied widely.[1] When the composite propellant surface is heated by the hot gas from the igniter, thermal decomposition of the oxidizer (AP particles) and the binder is promoted and the decomposition gas reacts to form a diffusion flame at the position apart from the combustion surface. Furthermore, the heat of flame is fed back to the propellant surface, and combustion is maintained. As the burning surface approaches to aluminum particles which are covered with aluminum oxide skin, they are heated and come to expose themselves to the binder vapor soon.

Aluminum particles which come out to the surface do not fly away immediately, but adhere to the decomposing binder surface. The melting point of aluminum is 933K, which is close to the burning-surface temperature. The aluminum, therefore, reaches to the melting point on the burning surface. Simultaneously, the oxide skin is torn so that liquid aluminum flows out and then particles collide to coalesce into larger one. Some particles coalesce further and agglomerate to form droplets of 100 to 200 micrometers depending on combustion pressure, burning rate, and diameters of aluminum, AP, etc.

If the temperature becomes as high as the boiling point (2750K @ 1atm) of aluminum and if the vapor is ignited, aluminum droplets leave from the surface floating and burning in the combustion gas. Some fraction of the total aluminum leaves as agglomerated droplets and the rest leaves as isolated particles. Burning droplets are enveloped in the detached sparkling flame of the temperature of about 3800K, and generate the smoke of particulates (droplets) of Al_2O_3 as a combustion product. On the surface of an aluminum particle, the portion which aluminum oxides gather is formed and is called an "alumina cap". The aluminum droplets become smaller as the combustion proceeds. The remnants which finally formed the alumina cap serve as alumina particles and are exhausted from a nozzle. Typically aluminum droplets are thought to go through such a process in an SRM chamber.

Generally, it is supposed that the 80-90% of aluminum in the propellant become fine particles (alumina smoke) of submicron order in size, and that the remainder will serve as alumina particles of which diameters varies from a few to several tens of micrometers. A sketch of burning aluminum droplets in SRM chamber is shown in Fig. 2.

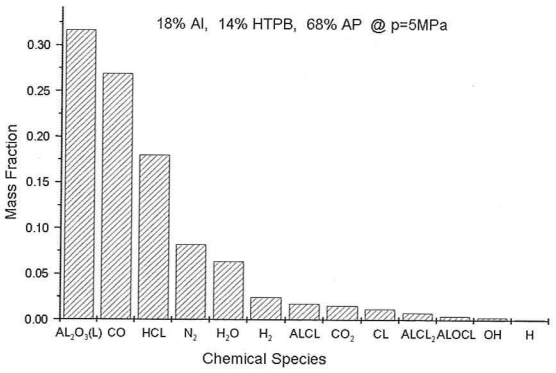

Fig. 1 Typical chemical equilibrium composition of SRM combustion gas

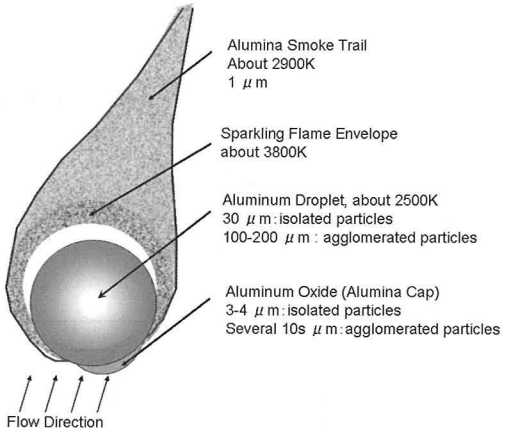

Fig. 2 Sketch of a burning aluminum droplet in SRM

1.2. Multiphase Flow in Solid Rocket Motors

It is a general feature of multiphase flow that micro-scale phenomena at phase interfaces affect fluid-dynamic phenomena of macro scale. In the case of multiphase flow in SRM, particle combustion, particle-gas momentum and energy exchanges, and particle-particle interaction are the former phenomena, and, on the other hand, the flow phenomenon in SRM-scale multiphase flow is the latter.

Let us investigate some typical features of multiphase flow in SRM through a case study of the model motor with the throat diameter of 0.19m, and the nozzle-exit area ratio 37 shown in Fig. 3. Here, a typical metallized composite propellant of an AP/HTPB/aluminum system (aluminum 18%) is assumed. The velocity and the temperature of a particle which are calculated in case of quasi-one-dimensional equilibrium flow are shown in Fig. 3. In this equilibrium flow, there are no lags between two phases in both velocities and temperatures. The chemical composition of the gas is frozen throughout the flow field by that of the chemical equilibrium state in the combustion chamber.

In the calculation, the drag force and the heat transfer acting on four kinds of particles (Al: 50 μm, 200 μm, Al_2O_3: 1 μm, 4 μm) when they pass one piece at a time independently through the gas flow are considered. The particle diameters do not change during the flight in the SRM. The aerodynamic drag coefficient and the Nusselt number for a sphere are estimated with the compressibility and the rarefied gas effects added to the incompressible fluid dynamics estimates.

It is understood from Fig. 3 that the difference between the phases enlarges as the particle diameter D_p increases. Furthermore, in order to grasp the character of multiphase flow of in SRM, several quantities are evaluated. The average particle distance δ is defined as

$$\delta = n_p^{-1/3}, \tag{1}$$

where the particle number density is denoted by n_p, assuming that the mixture ratio (mass flux ratio) is constant and all the particles are of the same size. The volume fraction α_p of the particle phase is the volume which particle phase occupies per unit volume of the multiphase mixture. Note that the values of n_p, α_p are dependent of the particle size.

The (momentum) Stokes number St is the ratio of the velocity-relaxation time between phases τ_v and a characteristic flow time τ_f,

$$St = \frac{\tau_V}{\tau_f}. \tag{2}$$

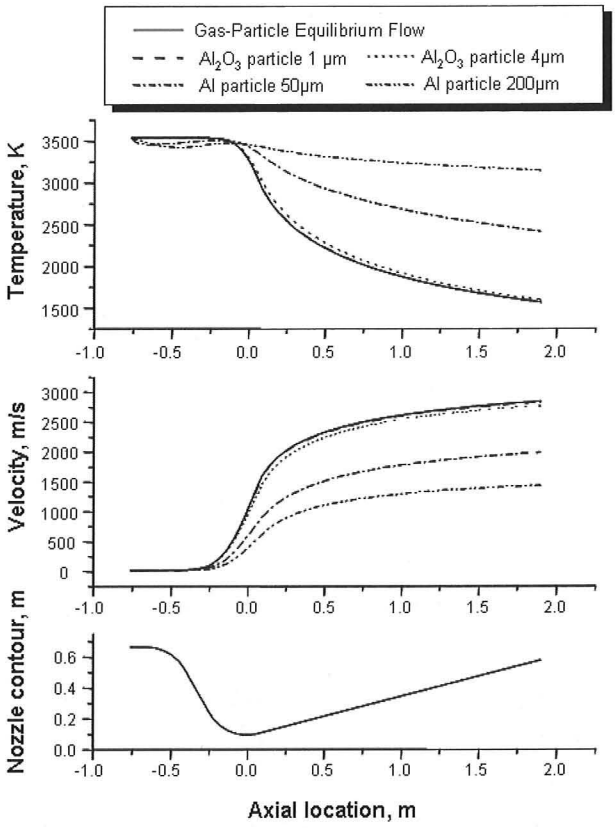

Fig. 3 Velocity and temperature distribution in a quasi-one dimensional phase equilibrium flow in SRM. Combustion pressure 5MPa, combustion temperature 3536K, the specific heat ratio 1.16, and average molecular weight 29.5.

The slip velocity is defined as the velocity difference of the two phases,

$$\vec{U}_s = \vec{U}_g - \vec{U}_p . \tag{3}$$

The slip temperature is defined as the temperature difference of the two phases,

$$T_s = T_g - T_p . \tag{4}$$

The particle Reynolds number is defined by

$$\mathrm{Re}_p = \left|\vec{U}_s\right| D_p \Big/ \nu_g . \tag{5}$$

The particle Mach number is defined by

$$M_p = \frac{\left|\vec{U}_s\right|}{a_g}, \tag{6}$$

where a_g is the speed of sound of the gas.

The residence time in a nozzle after the temperature of an Al_2O_3 particle decreases below the melting point (2303K) is denoted by t_{cr}.

The Weber number of a droplet *We* is defined by the ratio of the inertial force and the surface tension acting of the droplet,

$$We = \rho_g \left|\vec{U}_s\right|^2 D_p/\sigma_t \ . \tag{7}$$

The diffusion coefficient due to Brownian motion D_B is evaluated by the Einstein's formula

$$D_B = C_C k_B T/(3\pi\mu D_p) \tag{8}$$

in which a slip coefficient C_C of Cunningham is used.

Table 1 Characteristics of the multiphase flow in the model SRM

	Al_2O_3 1μm	Al_2O_3 4μm	Al 50μm	Al 200μm
δ (m)	$1\times10^{-5}\sim6\times10^{-5}$	$4\times10^{-5}\sim2\times10^{-4}$	$4\times10^{-4}\sim2\times10^{-3}$	$2\times10^{-3}\sim9\times10^{-3}$
α_p	$3\times10^{-6}\sim5\times10^{-4}$	$3\times10^{-6}\sim5\times10^{-4}$	$5\times10^{-6}\sim9\times10^{-4}$	$6\times10^{-6}\sim1\times10^{-3}$
St	$1\times10^{-4}\sim0.5$	$2\times10^{-3}\sim2$	$0.2\sim40$	$2\sim150$
$\left\|\vec{U}_s\right\|$ (m/s)	$0\sim20$	$0\sim140$	$0\sim850$	$0\sim1400$
T_s (K)	$-10\sim2$	$-80\sim7$	$-850\sim80$	$-1600\sim110$
Re_p	≤0.5	≤14	≤830	≤4900
M_p	≤0.024	≤0.14	≤1.2	≤2
t_{cr} (s)	5.7×10^{-4}	5.6×10^{-4}	NA	NA
We	≤0.001	≤0.2	≤45	≤360
D_B (m^2/s)	$5\times10^{-8}\sim5\times10^{-6}$	$1\times10^{-8}\sim1\times10^{-6}$	$5\times10^{-10}\sim7\times10^{-8}$	$1\times10^{-10}\sim1\times10^{-8}$

The result is summarized in Table 1. From this result, it is understood that the multiphase flow in SRM usually has the following features.

1) The volume of the particle can be ignored ($\alpha_p << 1$).
2) The gas-particle flow is dilute and disperse since $\delta >> D_p$ is realized. Particle motion, therefore, is controlled mainly by the surface force imposed from the gaseous phase and by the volume force like the gravity and rocket acceleration. Basically particle-particle collision can then be ignored or the binary collision is enough where it is necessary to consider it. Since the diameter of a particle is distributed, it is a poly-dispersed system.
3) It is a non-equilibrium flow in which the velocities and the temperatures, respectively, are different between the two phases and the interaction of the gaseous phase (continuous phase) and the particle phase (dispersed phase) is to be taken into account. Since the Stokes number is around the unity from the throat to the nozzle exit, one must usually consider non-equilibrium nature in SRM except for the case of a small particle in the combustion chamber ($St << 1$) and a large particle at the nozzle exit ($St >> 1$). In case of $St << 1$, the flow is called "equilibrium flow" and a particle follows the speed of the gaseous phase immediately. On the other hand, in case of $St >> 1$, the flow is called "frozen flow" and a particle and the gaseous phase behave independently.
4) Since the characteristic length of a flow is much greater than the average particle distance, a description of a continuum is possible for the particle phase. It is possible to define the amount of volume averages like dispersed density of the particle phase, and to express governing equations for the conservation of the mass, the momentum, and the energy of particle phase by the Eulerian description.
5) Diffusion of the particle by Brownian motion can be ignored.
6) The breakup of a droplet should be taken into account for a large particle. The surface tension of the droplet σ_t is

0.7 N/m and 0.84 N/m for aluminum and alumina, respectively. It is thought that if the Weber number exceeds a critical value We^*, the breakup of the droplet occurs. The critical Weber number changes with the kind of droplet, and the methods of acceleration, usually values of 15～30 are employed for alumina and aluminum.

7) Solidification of alumina can be disregarded. It is thought to take several seconds or several minutes for even a particle of 1 μm to solidify because it takes finite time before a solidification core is generated in a droplet and heat is released out of the surface. Since, on the other hand, t_{cr} is less than a millisecond, it is thought that a particle is in supercooled liquid phase within a nozzle.
8) A large aluminum droplet may not complete combustion within the residence time. The possibility of incompleteness becomes high as the size of SRM becomes smaller and the size of a droplet becomes larger.

In Chapter 2, mathematical models of multiphase flows in SRM and the sensitivity of various parameters on the phase interaction are described. The fluid dynamic force acting on a particle in a steady uniform free stream with the effects of compressibility and rarefied gas dynamics is discussed. Forces due to non uniform or unsteady free stream and their important role in the multiphase flow in SRM are discussed. The convective heat transfer and the radiative heat transfer between gas and a particle are also described.

In Chapter 3, as numerical simulation methods for the multiphase flow in SRM, the Eulerian-Eulerian method, the Eulerian-Lagrangian method, and the Eulerian-hybrid method are explained. Especially, about the Eulerian-Eulerian method, detailed description is given on the construction of a solution tool for axisymmetric multiphase flows. The effect of the particle diameter distribution is described in the Eulerian-Lagrangian method. The Eulerian-hybrid method is described towards the construction of a more realistic numerical simulation tool dealing with the effects of particle combustion and breakup.

In Chapter 4, numerical experiments are conducted using the technique stated in Chapter 3, and the feature of each technique is clarified. In Section 4.1, comparisons of the Eulerian-Eulerian method and the Eulerian-Lagrangian method are performed about two-dimensional, axisymmetric, and three-dimensional cases. In Section 4.2, several flows, from zero dimension to three dimensions, are computed using the Eulerian-hybrid method, and the effect of the combustion model of a particle and the effect of the particle-breakup model are verified.

2. Parameter sensitivity on forces and heat transfer of gas-particle Flow in SRM

2.1. Forces acting on a particle

Equation of motion

The equation of motion of the particle in fluid is expressed with Eq.(9).

$$m_p \frac{d\vec{U}_p}{dt} = \vec{F}_D + \vec{F}_G + \vec{F}_C \tag{9}$$

Here m_p is the particle mass ($=V_p \cdot \sigma_m$), σ_m the particle true density, V_p the particle volume, $\vec{U}_p$ the particle velocity vector, $\vec{F}_D$ the fluid dynamic force, $\vec{F}_G$ the gravity and the inertial force, and $\vec{F}_C$ the contact force between particles.

Fluid dynamic forces

When a particle has a spherical shape, the fluid dynamic force acting on the particle can be written in the following form[2].

$$\vec{F}_D = \frac{\pi}{8} C_D \rho_g D_p{}^2 \left|\vec{U} - \vec{U}_p\right| \left(\vec{U} - \vec{U}_p\right) \quad - V_p \nabla p \quad + V_p \nabla \cdot \vec{\tau} \quad + \frac{\rho_g}{2} V_p \left(\frac{D\vec{U}}{Dt} - \frac{d\vec{U}_p}{dt} \right)$$
$$+ \frac{3}{2} D_p{}^2 \sqrt{\pi \rho_g \mu} \left[\int_{t_0}^{t} \left(\frac{D\vec{U}/Dt - d\vec{U}_p/dt}{\sqrt{t - t'}} \right) dt' + \frac{\left(\vec{U} - \vec{U}_p\right)_{t_0}}{\sqrt{t}} \right] \tag{10}$$

Here D_p is the particle diameter, ρ_g the gas density, p the gas pressure, $\vec{U}$ the gas velocity vector, $\vec{\tau}$ the stress tensor, μ the gas viscosity coefficient, and C_D the drag coefficient.

In the right-hand side of Eq.(10), the first term is the fluid-dynamic drag in a steady and uniform flow, the second is the force due to the pressure gradient in the main stream, the third is the force due to the shear stress gradient, the fourth is the force required to accelerate additional mass (delay of the form drag change by acceleration) and sometimes called apparent mass force, and the fifth is the force by the temporal delay in boundary layer development due to the relative acceleration of unsteady motions of particle and fluid (Basset force).

In Eq.(10) D/Dt is the substantive derivative defined below.

$$\frac{D}{Dt} = \frac{\partial}{\partial t} + u\frac{\partial}{\partial x} + v\frac{\partial}{\partial y} + w\frac{\partial}{\partial z} \tag{11}$$

Fluid-dynamic drag in a steady and uniform flow

The fluid-dynamic force in Eq.(10) depends largely on the evaluation of C_D. There are several estimation formulae of a fluid-dynamic drag of a sphere.

① Stokes law

$$C_D = \frac{24}{\mathrm{Re}} \tag{12}$$

② Newton law

$$C_D = 0.45 \tag{13}$$

③ Schlichting[3]

$$C_D = \frac{24}{\mathrm{Re}} \left(1 + \frac{3\,\mathrm{Re}}{16} \right) \tag{14}$$

④ Schiller and Naumann[4]

$$C_D = \frac{24}{\mathrm{Re}} \left(1 + 0.15\,\mathrm{Re}^{0.687} \right) \qquad (\mathrm{Re} \le 800) \tag{15}$$

⑤ Wen and Yu[5]

$$C_D = \begin{cases} \dfrac{24}{\mathrm{Re}} \left(1 + 0.15\,\mathrm{Re}^{0.687} \right) & (\mathrm{Re} \le 1000) \\ 0.43 & (\mathrm{Re} > 1000) \end{cases} \tag{16}$$

⑥ Putnam[6]

$$C_D = \begin{cases} \dfrac{24}{\mathrm{Re}}\left(1+\dfrac{\mathrm{Re}^{2/3}}{6}\right) & (\mathrm{Re} < 1000) \\ 0.4392 & (1000 \le \mathrm{Re} < 300000) \end{cases} \tag{17}$$

⑦ Clift and Gauvin[7]

$$C_D = \frac{24}{\mathrm{Re}}\left(1+0.15\,\mathrm{Re}^{0.687}+\frac{0.0175\,\mathrm{Re}}{1+4.25\times10^4\,\mathrm{Re}^{-1.16}}\right) \tag{18}$$

⑧ Carlson and Hoglund[8]

$$C_D = C_{D0}\left(\frac{\left\{1+\exp\left[-\left(\dfrac{0.427}{M^{4.63}}\right)-\left(\dfrac{3.0}{\mathrm{Re}^{0.88}}\right)\right]\right\}}{1+\dfrac{M}{\mathrm{Re}}\left[3.82+1.28\exp\left(-\dfrac{1.25\,\mathrm{Re}}{M}\right)\right]}\right) \tag{19}$$

⑨ Henderson[9]

$$\text{if } M \ge 1.75, \quad C_D = \frac{0.9+\dfrac{0.34}{M^2}+1.86\left(\dfrac{M}{\mathrm{Re}}\right)^{1/2}\left[2+\dfrac{2}{M^2\gamma/2}+\dfrac{1.058}{M\sqrt{\gamma/2}}\right]\left(\dfrac{T_p}{T_g}\right)^{1/2}-\dfrac{1}{M^4\gamma^2/4}}{1+1.86\left(\dfrac{M}{\mathrm{Re}}\right)^{1/2}} \tag{20}$$

$$\text{if } M \le 1, \quad C_D = 24\left[\mathrm{Re}+M\sqrt{\gamma/2}\left\{4.33+\left(\frac{3.65-1.53\dfrac{T_p}{T_g}}{1+0.353\dfrac{T_p}{T_g}}\right)\exp\left(-0.247\frac{\mathrm{Re}}{M\sqrt{\gamma/2}}\right)\right\}\right]^{-1} + \exp\left(-\frac{0.5M}{\sqrt{\mathrm{Re}}}\right)\left[\frac{4.5+0.38(0.03\,\mathrm{Re}+0.48\sqrt{\mathrm{Re}})}{1+0.03\,\mathrm{Re}+0.48\sqrt{\mathrm{Re}}}+0.1M^2+0.2M^8\right] + 0.6M\sqrt{\gamma/2}\left[1-\exp\left(-\frac{M}{\mathrm{Re}}\right)\right] \tag{21}$$

$$\text{if } 1 < M < 1.75, \quad C_D(M,\mathrm{Re}) = C_D(1.0,\mathrm{Re}) + \frac{3}{4}(M-1.0)\left[C_D(1.75,\mathrm{Re})-C_D(1.0,\mathrm{Re})\right] \tag{22}$$

⑩ Crowe[10]

$$C_D = 2+(C_{D0}-2)\exp\left(-3.07\sqrt{\gamma}\,\frac{M}{\mathrm{Re}}g(\mathrm{Re})\right)+\frac{h(M)}{\sqrt{\gamma}M}\exp\left(-\frac{\mathrm{Re}}{2M}\right) \tag{23}$$

$$\log_{10}\left(g(\mathrm{Re})\right) = 1.25\left(1+\tanh(0.77\log_{10}\mathrm{Re}-1.92)\right)$$

$$h(M) = \left[2.3+1.7\sqrt{\frac{T_p}{T_g}}\right]-2.3\tanh\left(1.17\log_{10}M\right)$$

⑪ Hermsen[11]

$$C_D = 2 + (C_{D0} - 2)\exp\left(-3.07\sqrt{\gamma}\,\frac{M}{\mathrm{Re}}\,g(\mathrm{Re})\right) + \frac{h(M)}{\sqrt{\gamma}M}\exp\left(-\frac{\mathrm{Re}}{2M}\right) \tag{24}$$

$$g(\mathrm{Re}) = \frac{1 + \mathrm{Re}(12.278 + 0.548\,\mathrm{Re})}{1 + 11.278\,\mathrm{Re}}, \qquad h(M) = \frac{5.6}{1+M} + 1.7\sqrt{\frac{T_p}{T_g}}$$

The Reynolds number and the Mach number in the above formulae are defined based on a particle diameter and relative velocity.

$$\mathrm{Re} = \frac{\rho\left|\vec{U}_s\right|D_p}{\mu}, \qquad M = \frac{\left|\vec{U}_s\right|}{\sqrt{\gamma R T_g}} \tag{25}$$

Here, Re is the Reynolds number, M the Mach number, $\vec{U}_s$ is the slip velocity, γ the specific heat ratio, R the gas constant, T_g the gas temperature, and T_p the particle temperature.

The equations (12) to (18) are expressions of incompressible drag coefficients, whereas the compressibility and rarefied-gas dynamic effects are taken into account in Eqs. (19) to (24). The incompressible drag coefficient is denoted by C_{D0}. In the following analyses, C_{D0} is estimated by Eq.(16).

The comparison of drag coefficients (①~⑦) for the case of incompressible free-stream is shown in Fig. 4. The drag coefficient ① and ③ are the expressions that should be originally applied to a low Reynolds number of about Re <1, and behavior obviously different from another is shown on the high Reynolds number region. On the other hand, the drag coefficient ② is the one to be applied to the high Reynolds number side of about Re >1000, and is obviously different from other drag coefficients in the low Reynolds number region. It is understood that the empirical expressions, ④~⑦, which are proposed to be applicable within a comparatively wide range of the Reynolds number, almost estimate a similar value.

On the other hand, the expressions ⑧~⑪ are made to deal with the effect of compressibility and rarefaction, and they are compared in Fig. 5. When compressibility is weak (Mach 0.1), any formula gives the almost same result, but if compressibility becomes strong, the gap between methods is conspicuous. Since the Knudsen number Kn is of the order of M/Re, the degree of rarefaction becomes high as we go in Fig. 5 to the left, and the degree of rarefaction becomes low as we go to the right. Although any formula gives a result resembled in high-rarefaction and low-rarefaction regions, the variation among methods is large in the intermediate-rarefaction region.

Effect of a drag coefficient to the particle motion in SRM combustion gas

In order to see the effect of a drag coefficient to the particle motion in SRM combustion gas, traces of a particle injected with a constant initial velocity in a uniform stream shown in Fig. 6 are calculated for the conditions described in Table 2 and the difference in the particle locus is evaluated among drag coefficient expressions mentioned above. The temperature ratio appearing in ⑨, ⑩, and ⑪ is always set to unity.

In case that the initial velocity is so small that the compressibility is ineffective, a particle locus hardly depends on the calculation method of drag. If initial velocity is large and the influence of compressibility becomes large, a particle locus will vary with the drag calculation method. The particle loci computed for the case of the initial velocity of 500 m/s are shown in Fig. 7. It is seen in Fig. 8 that, in the larger Reynolds number region, the gap in the drag coefficients is large, whereas in the lower Reynolds number region, the same drag coefficient by any method is obtained. It is worth noticing that, in this problem, the particle locus by Stokes drag shows a completely different trend from others.

As mentioned above, in the portion where the Reynolds number is large and the compressibility is comparatively strong, it turns out that the formula considering of a compressibility effect (or a rarefaction effect) should be used. Moreover, although the Stokes drag coefficient is often used in a simple calculation, cautions are required so that it is used

in the very small range of the Reynolds number, unless a completely different solution may arise. The expressions taking account of compressibility and rarefaction give a little different results.

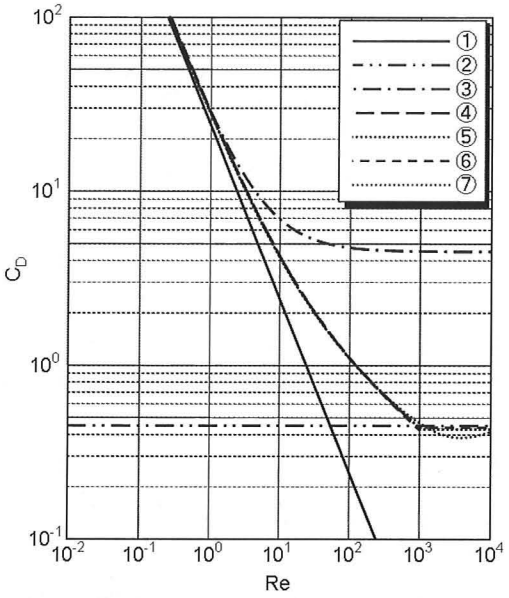

Fig. 4 Comparison of drag coefficients

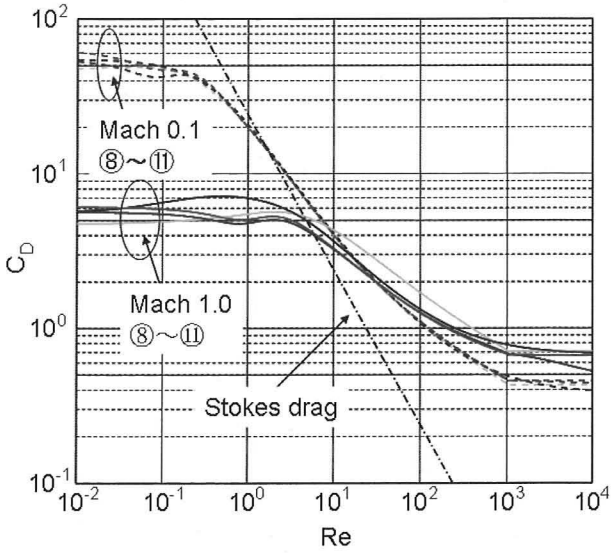

Fig. 5 Comparison of drag coefficient

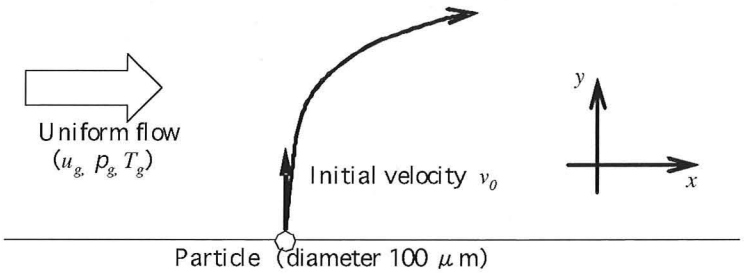

Fig. 6 Setup of numerical test of particle motion injected into a uniform stream

Table 2 Calculation conditions

Particle diameter	100 μm
Particle density	2500 kg/m^3
Free-stream pressure	10 MPa
Free-stream temperature	3000 K
Free-stream velocity	50 m/s
Specific heat ratio	1.2
Mean molecular weight	30 g/mol
Particle injection velocity	50 and 500 m/s

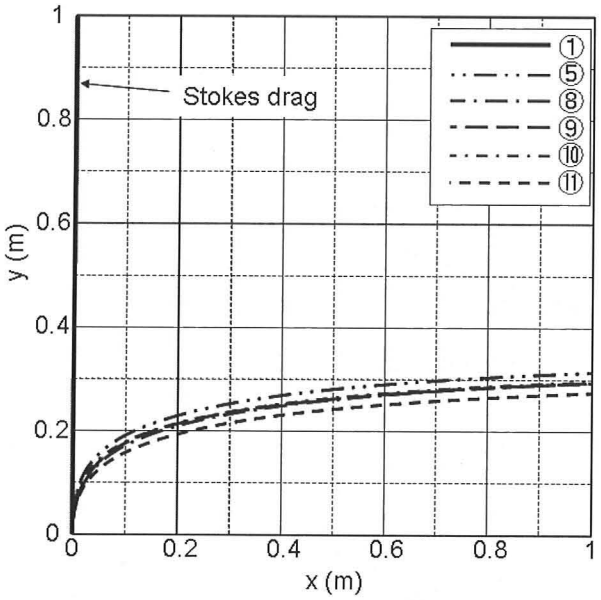

Fig. 7 Comparison of a particle locus (initial velocity 500 m/s)

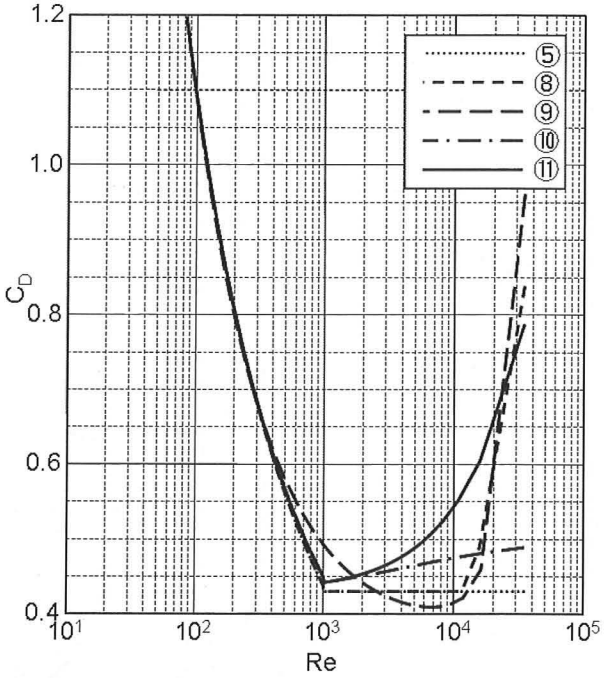

Fig. 8 Comparison of a drag coefficient along particle loci (initial velocity 500m/s)

Force due to a pressure gradient

A local pressure gradient exerts force on a particle. The force can be estimated by integrating the pressure over the particle surface.

$$\vec{F}_p = \int_{cs} -p\vec{n}dS = \int_{cv} -\nabla p dV \tag{26}$$

Here "cs" denotes the surface and "cv" denotes the volume of the sphere. The divergence theorem is used in the above equation.

When a sphere is small compared with the scale of change of the pressure gradient, the pressure gradient is considered to be constant all over the sphere. In this case Eq.(26) can be written as

$$\vec{F}_p = -\nabla p V_p . \tag{27}$$

Let us check the amount of this force for a solid rocket motor. The pressure and the pressure gradient in the nozzle shown in Fig. 9 are estimated by a quasi-one dimensional analysis. Here, the length and the pressure are non-dimensionalized by the throat diameter D_t and the chamber pressure. p_c, respectively.

From Fig. 9, it turns out that the absolute value of the pressure gradient becomes the maximum at the throat and its amount is about the ratio of the chamber pressure to the throat diameter. This approximation is generally valid for usual solid rocket motors.

$$\nabla p \approx \frac{p_c}{D_t} \tag{28}$$

Numerical experiment to evaluate the influence of a pressure gradient

Next, in order to investigate how much this pressure gradient contributes to the motion of a particle, numerical

analysis is performed for the case of putting a particle in the flow with the uniform velocity and pressure gradient as shown in Fig. 10. In the analysis, the initial particle speed is the same as the gas speed, and it accelerates by the pressure-gradient force to settle in a steady speed after a while. Beside the pressure-gradient force, only the fluid-dynamic drag in a steady uniform flow is taken into account in Eq. (10). Therefore, the result shows contribution of the pressure-gradient term over the steady fluid-dynamic drag. The formula of Henderson is used for a drag coefficient.

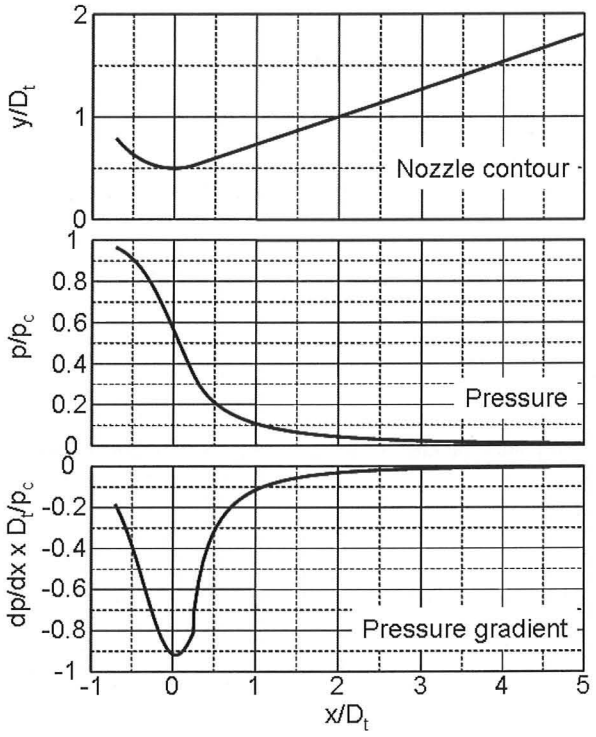

Fig. 9 Pressure and pressure gradient in SRM (quasi-one dimensional analysis)

A flow in a throat region (throat diameter of 100mm) with p_c=10MPa and T_c=3000K is assumed as the mainstream.

The uniform flow velocity is set as a parameter ranging within 100～1500m/s. The flow velocity distribution near the wall in the throat region obtained by a CFD analysis (M-25 motor axisymmetric analysis) is shown in Fig. 11. In this case, boundary layer thickness is of the order of millimeter and the flow velocity changes between 100 m/s and 1000 m/s roughly at the distance from the wall changing from the order of the particle diameter (micrometer) to the outer-edge of the boundary layer (the order of millimeter). Since the pressure gradient is imposed inside the boundary layer as well as the boundary layer exterior, the difference in the effect is checked by changing the flow velocity.

Here, since the particle is initially moving at the same speed as a uniform flow, it should flow at the same speed unless a pressure gradient exists. Here, the ratio of the speed of the particle to that of the gas is denoted by ϕ and is considered as the index of the pressure-gradient effect.

$$\phi = \frac{u_p}{u_g} \tag{29}$$

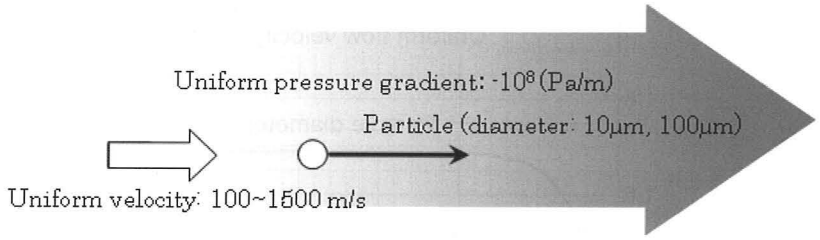

Fig. 10 Numerical experiment of the effect of pressure gradient on particle motion

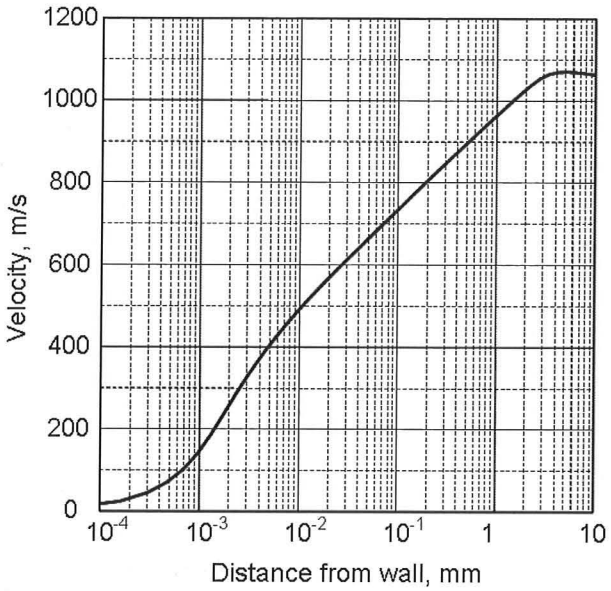

Fig. 11 Flow velocity distribution near the wall at a throat (a CFD result of M-25)

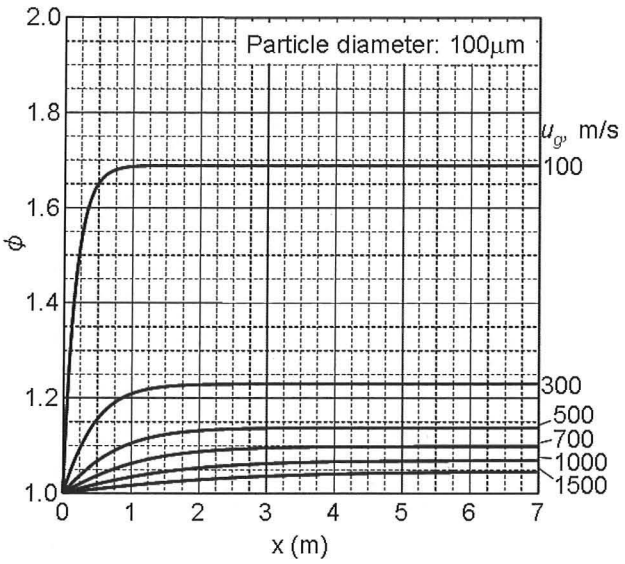

Fig. 12 Change of particle speed by pressure gradient for various uniform flow velocity levels

In the case of the particle diameter of 100 μm, if a pressure gradient is taken into account to the initial velocity of 100 m/s (uniform flow velocity), the terminal speed of the particle turns out to become about 1.7 times of the gas speed as shown in Fig. 12. The ratio of the terminal speed to the gas speed falls as the uniform flow velocity becomes large, and it is about 5% of increase in the case of the uniform flow velocity of 1500 m/s. It turns out that, for the particle diameter of 10 μm, the increase in speed becomes about 5% even when the uniform flow velocity is 100 m/s as shown in Fig. 13.

Therefore, when a particle diameter is large (order of 100 μm) and when a big pressure gradient is imposed to a region of slow gas speed like in the boundary layer, the influence of a pressure gradient becomes comparable as the fluid-dynamic drag and is not negligible.

Force due to a shear-stress gradient

A local shear-stress gradient exerts force on a particle. The force can be estimated by integrating the stress over the particle surface similarly to the pressure-gradient force.

$$\vec{F}_p = \int_{cs} \vec{\tau} \cdot \vec{n} dS = \int_{cv} \nabla \cdot \vec{\tau} dV \tag{30}$$

When a sphere is small compared with the scale of change of the shear-stress gradient, it can be considered that the shear-stress gradient is constant all over the sphere. In this case Eq.(30) can be written as

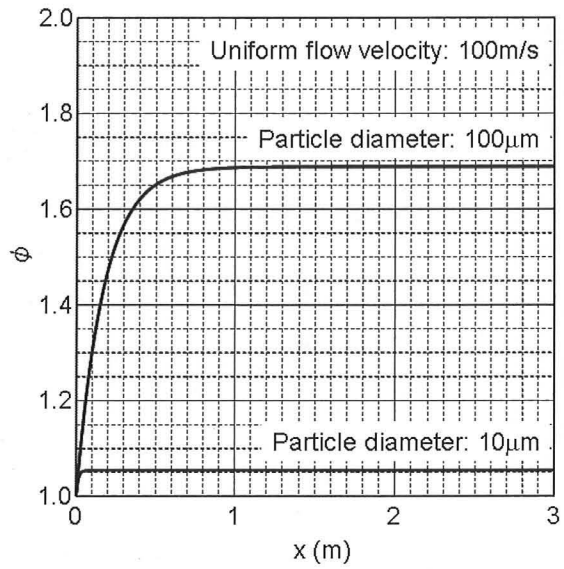

Fig. 13 Change of particle speed by pressure gradient for particle diameters of 10 and 100 μm

$$\vec{F}_p = \nabla \cdot \vec{\tau}\, V_p \tag{31}$$

Stress gradient within a boundary layer

The flow in a boundary layer can be thought as an example in which a stress gradient participates greatly. In order to investigate the influence of the force due to the stress gradient within a boundary layer, a model of a flow field shown in Fig. 14 is considered. Here, the distributions of the x-direction component of the flow velocity, u, are modeled by extracting, from the result of CFD analysis (M-25 axisymmetric heat flux analysis at the wall temperature of 2500K), the portion where the outer-edge speed is about 100 m/s and the other portion of flow near the throat. The components (v, w) in the y and z-directions, respectively, are always set to zero. Actually $v \neq 0$, but it is negligible because $v \ll u$. The distribution of the density and the viscous coefficient in the boundary layer are also set up based on the CFD analysis result.

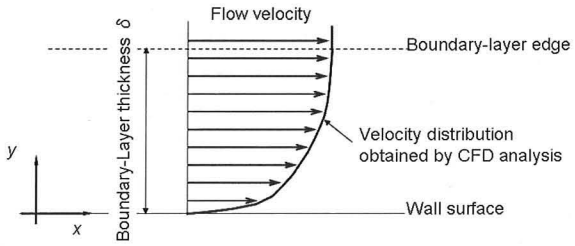

Fig. 14 Velocity distribution model in a boundary layer

In the model shown in Fig. 14, the dominant component in the stress tensor is

$$\tau_{12} = \mu \frac{du}{dy}. \tag{32}$$

The distributions of the flow velocity and the viscous coefficient (eddy viscosity is included) and the shearing force used for this model are shown in Fig. 15 and Fig. 16, respectively.

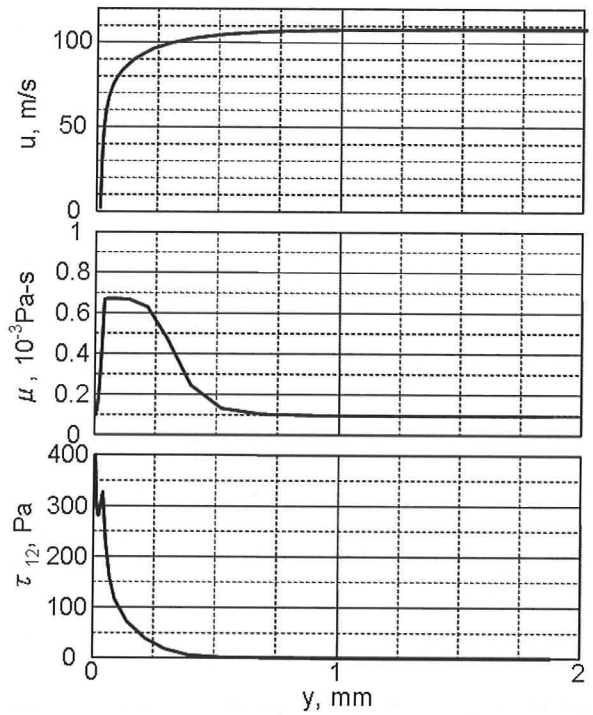

Fig. 15 Distributions of velocity, viscosity coefficient, and shear stress (where the speed at the boundary layer edge is about 100 m/s)

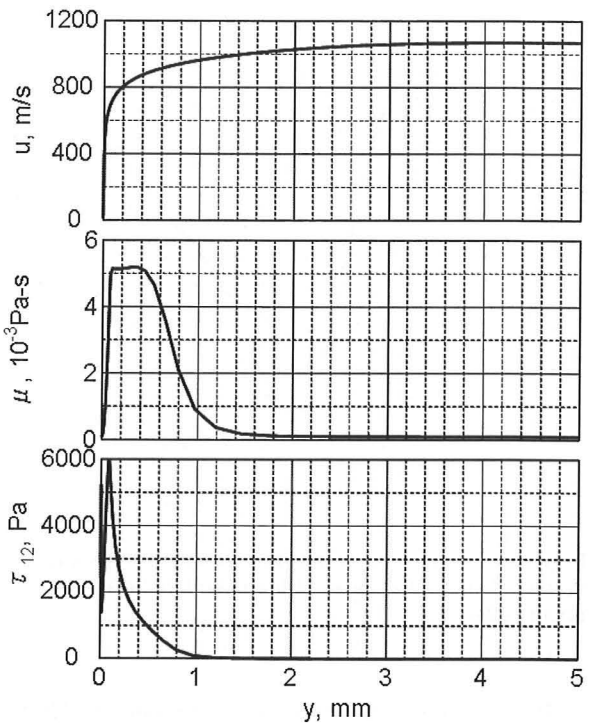

Fig. 16 Distributions of velocity, viscosity coefficient, and shear stress (near the throat)

Numerical experiment to evaluate the influence of a shear-stress gradient

It can be seen from these figures that the shear stress grows suddenly in the adjacent region within the distance of 0.5mm to about 1mm from the wall. Since the diameter of an agglomerate droplet is the order of 100 μm, this steep-gradient domain is as thick as the diameter of the large droplet.

In order to see the influence of a stress gradient, a particle is placed in a flow field and the deceleration process is investigated as shown in Fig. 17. As shown previously, since a stress gradient becomes large rapidly near the wall surface, a situation where a particle is nearly touching the wall surface is considered.

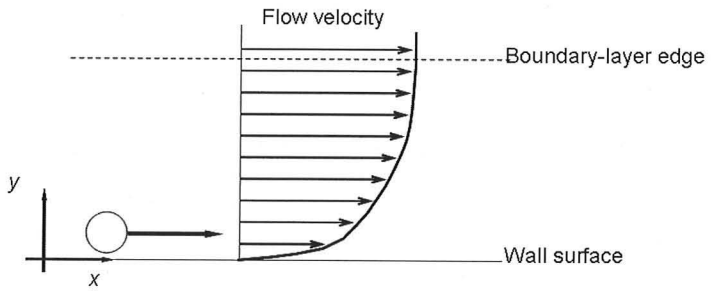

Fig. 17 Numerical experiment to see the influence by the stress gradient

The result of the analysis is shown in Fig. 18 and Fig. 19. The ratio ϕ of the flow velocity in the steady state to that at the center of the particle is plotted in these figures.

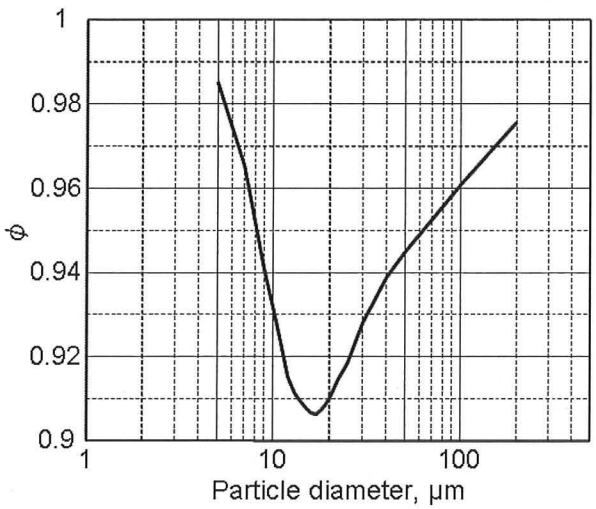

Fig. 18 Change of the particle speed by the stress gradient (where the speed at the boundary layer edge is about 100 m/s)

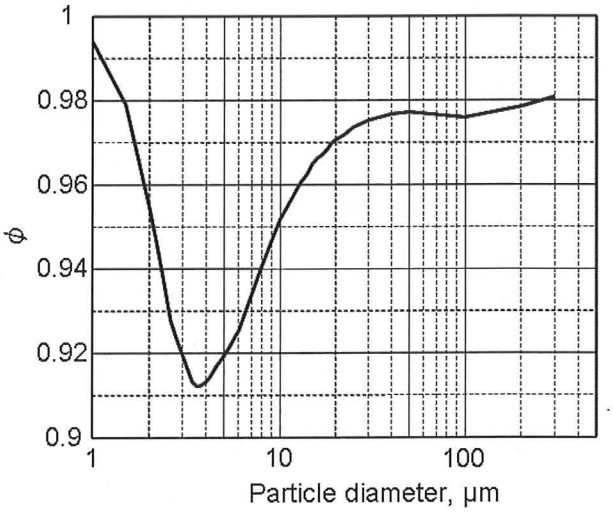

Fig. 19 Change of the particle speed by the stress gradient (near the throat)

It is shown in Fig. 18 that, when the boundary-layer-edge speed is about 100 m/s, the influence of a stress gradient becomes most strong for particle diameter of near 20 μm and the influence appears as about 10% of a speed decrease. Within the boundary layer, as the particle diameter becomes smaller, the particle will be located closer to the wall surface and be imposed by a stronger stress gradient, whereas the volume of the particle becomes smaller. For this reason, the amount of the right-hand side of Eq. (31) is determined by the balance of those two effects, and the influence is coming out most greatly for particle diameter about 20 μm in the present model. The particle diameter in which the influence of a stress gradient appears most greatly varies with amounts of quantities of a boundary layer (thickness, outer-edge speed). In case of the throat region, the particle diameter is about 3 to 4 μm as shown in Fig. 19.

As mentioned above, it turns out that it is required to take the effect of a stress gradient into account, since the influence becomes large depending on particle diameter in a boundary layer near the wall surface.

Force due to the additional mass

When a particle accelerates in fluid, the inertia increases because the surrounding fluid is dragged with the particle motion. The increased inertia is called the additional mass. This term appears in connection with the unsteadiness of the slip velocity.

In order to understand the effect of the additional mass term, only the steady fluid-dynamic drag term and the additional mass term are taken out from Eq. (10) and substituted into the equation of motion as follows.

$$V_p \sigma_m \frac{d\vec{U}_p}{dt} = \frac{\pi}{8} C_D \rho_g D_p{}^2 \left|\vec{U} - \vec{U}_p\right| \left(\vec{U} - \vec{U}_p\right) + \frac{\rho_g}{2} V_p \left(\frac{D\vec{U}}{Dt} - \frac{d\vec{U}_p}{dt} \right) \tag{33}$$

Let us transform Eq. (33) into a non-dimensioned form with the length normalized by the particle diameter, D_p, the time by the relaxation time, τ_V, and the velocity by the free-stream speed, U_∞. The relaxation time can be written as

$$\tau_v = \frac{\sigma_m D_p^{\ 2}}{18\mu}. \tag{34}$$

The non-dimensioned equation can be written as

$$\frac{d\vec{\bar{U}}_p}{d\bar{t}} = \frac{\mathrm{Re}}{24} C_D \left|\vec{\bar{U}} - \vec{\bar{U}}_p\right| \left(\vec{\bar{U}} - \vec{\bar{U}}_p\right) + \frac{\chi}{2}\left(\frac{D\vec{\bar{U}}}{D\bar{t}} - \frac{d\vec{\bar{U}}_p}{d\bar{t}}\right) \tag{35}$$

where ($\bar{}$) designates a dimensionless quantity. Dimensionless parameters Re and χ are defined by the following equations.

$$\mathrm{Re} = \frac{\rho_g U_\infty D_p}{\mu}, \qquad \chi = \frac{\rho_g}{\sigma_m} \tag{36}$$

Equation (35) shows that the additional mass term is proportional to the density ratio χ and a difference of the acceleration between the gas and the particle. On the other hand, the density ratio is not contained in the steady fluid-dynamic drag term. In the SRM internal flow, since the density ratio is a very small value of about 1/1000, it is usually the case that the additional mass term can be ignored compared with the steady fluid-dynamic drag. However, when the difference of the acceleration between the phases is very large, even if the density ratio is small, the additional mass term can become significant.

Numerical experiment to evaluate the influence of an additional mass

As a situation in which the influence of an additional mass term appears greatly, the motion of the particle placed in the vortex is considered as shown in Fig. 20.

Here, the flow shall be in steady state and have a constant velocity component u in the x-direction, and shall carry out

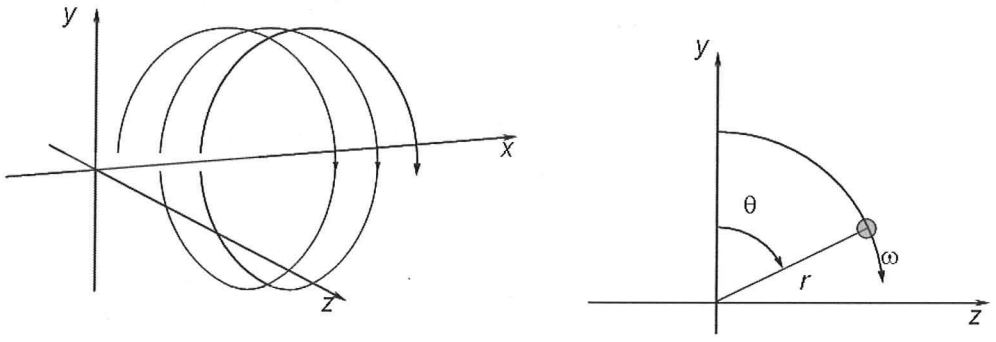

Fig. 20 Numerical experiment for the effect of an additional mass on particle motion

rigid-body rotation with an angular velocity ω in the y-z plane.

$$\vec{U} = (u, -r\omega\sin\theta, r\omega\cos\theta) \tag{37}$$

The substantive derivative of $\vec{U}$ is calculated as

$$\frac{D\vec{U}}{Dt} = \left(\vec{U}\cdot div\right)\vec{U} = (0, -r\omega^2\cos\theta, -r\omega^2\sin\theta) \tag{38}$$

Suppose that a particle flows in from the upstream near the center of this vortex. Since the very center becomes a singular point, an initial position of $r = R \neq 0$, $\theta = 0$ is assumed.

The loci of the particle for cases with and without an additional mass taken into account are compared and shown in Fig. 21 ~ Fig. 26. The flow is assumed to have u =1m/s and the vortex of 50Hz of number of rotations. The initial locations of a particle shall be =0.1, 10, and 1000 μm and the particle diameters 100 and 500 μm.

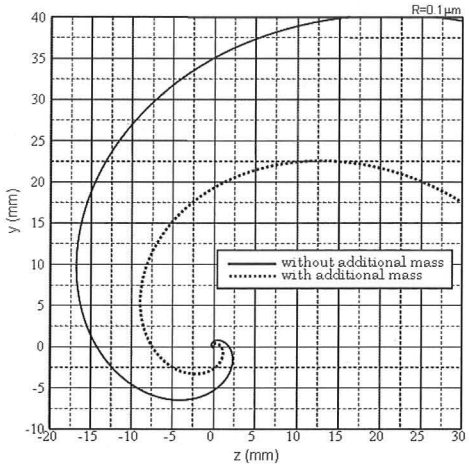

Fig. 21 Effect of additional mass: Comparison of particle locus (R = 0.1 μm, D_p = 100 μm)

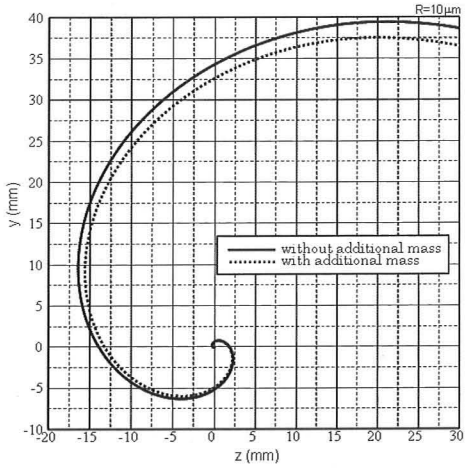

Fig. 22 Effect of additional mass: Comparison of particle locus (R = 10 μm, D_p = 100 μm)

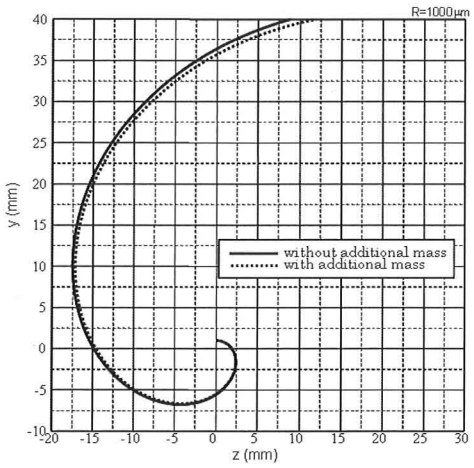

Fig. 23 Effect of additional mass: Comparison of particle locus (R = 1000 μm, D_p = 10 μm)

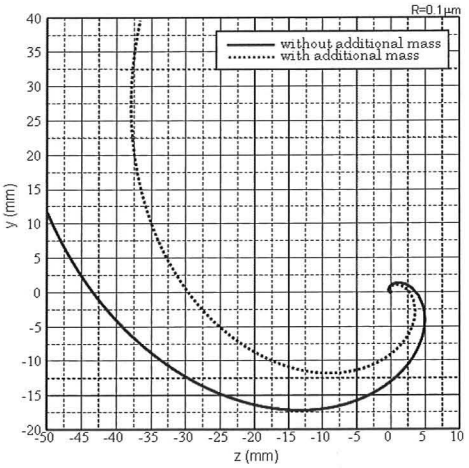

Fig. 24 Effect of additional mass: Comparison of particle locus (R = 0.1 μm, D_p = 500 μm)

The effect of additional mass shows up greatly as the particle diameter becomes large and the initial position becomes close to the vortex center as well. This is due to the fact that the acceleration term becomes large in comparison to the steady fluid-dynamic drag near the vortex center. It turns out that, when a particle is placed near the center, the difference in a position arises to a 10mm order by the inclusion of an additional mass while moving in 50mm×50mm region in the y-z plane. In the case of 500 μm of particle diameter, even when the gap from the vortex center of the initial position is as large as about 2 times of particle diameter, particle loci differ considerably depending on whether or not the additional mass is taken into account.

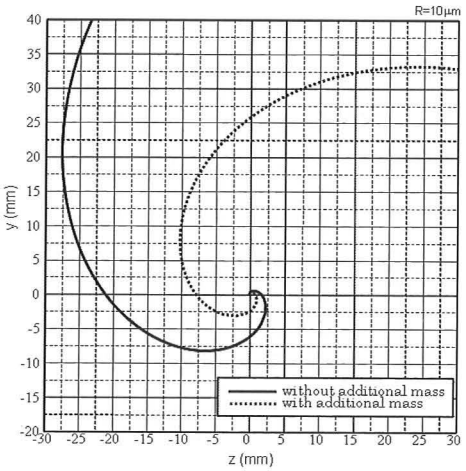

Fig. 25 Effect of additional mass: Comparison of particle locus (R = 10 μm, D_p = 500 μm)

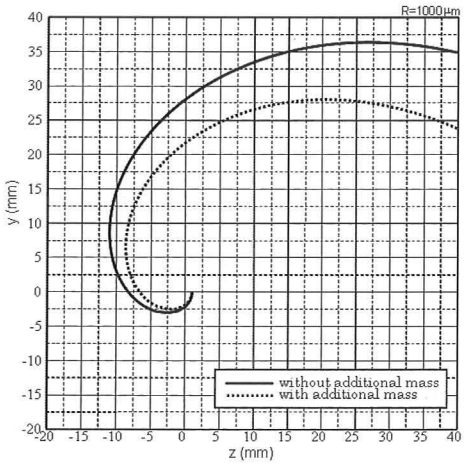

Fig. 26 Effect of additional mass: Comparison of particle locus (R = 1000 μm, D_p = 500 μm)

Therefore, when acceleration is large, e.g., in case that a particle flows into the center of a vortex with big angular velocity, the additional mass term cannot be neglected.

The nozzle liner, in SRM, placed downstream of the throat insert may sometimes form concave surface by the ablation phenomena. In such a situation, Görtler-type vortices as shown in Fig. 27 may occur from the hydrodynamic instability due to centrifugal force. When a particle is involved in such vortices, situation mentioned above may grow up.

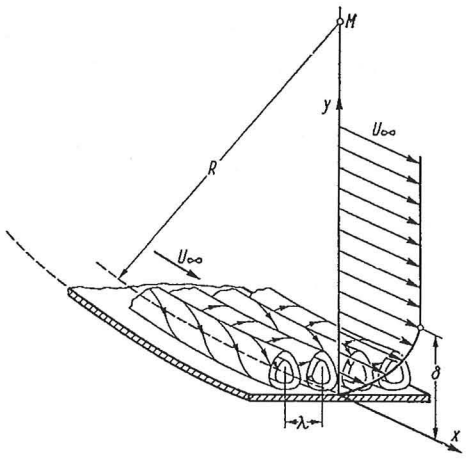

Fig. 27 Görtler vortex (Ref.3)

2.2. Heat exchange between a particle and the gaseous phase

Energy equation

Equation which describes the temporal change of the internal energy of a particle can be written as

$$m_p \frac{d\left(C_{P_p} T_p\right)}{dt} = Q_R + Q_C , \tag{39}$$

where m_p denotes particle mass, C_{P_p} specific heat of particle, T_p particle temperature, Q_R radiative heating, and Q_C convective heating. It is assumed that the temperature inside a particle is uniform here.

Convective heating

The convection heating term can be written as

$$Q_c = \pi D_p{}^2 \, h\left(T_g - T_p\right) + \frac{\pi D_p{}^3 \lambda}{12} \nabla^2 T_g + \pi D_p{}^2 \lambda \int_0^t \frac{\left(\frac{DT_g}{Dt} - \frac{dT_p}{dt}\right)}{\sqrt{\pi \alpha_g (t-\tau)}} d\tau \,, \tag{40}$$

where h denotes heat transfer coefficient, T_g surrounding gas temperature, λ thermal conductivity of gas, α_g thermal diffusivity, and D_p particle diameter.

The first term in Eq. (40) represents the steady-state term, the second does the non-uniformity term, and the third does the unsteadiness term. Here the effect due to particle combustion is not taken into account.

Steady-state term

Convective heating to the surface of a sphere from a steady uniform flow is expressed as

$$Q_c = \pi D_p{}^2 \, h\left(T_g - T_p\right). \tag{41}$$

Since the heat transfer coefficient can be written with the Nusselt number by definition as

$$h = \frac{Nu\lambda}{D_p}, \tag{42}$$

Eq. (41) can be rewritten as

$$Q_c = Nu\lambda\pi D_p \left(T_g - T_p\right). \tag{43}$$

The thermal conductivity of gas λ is estimated by the film temperature T_f in consideration of physical-properties change within the thermal boundary layer on the surface of a particle. The definition of T_f is

$$T_f = 0.5\left(T_g + T_p\right). \tag{44}$$

Various formulae are proposed for the Nusselt number. Some of them are summarized below.

①[12]

$$Nu = 2.5\,\mathrm{Re}^{0.15} + 0.04\,\mathrm{Re} \tag{45}$$

②[12]

$$Nu = 2 + 0.370\,\mathrm{Re}^{0.6}\,\mathrm{Pr}^{1/3} \tag{46}$$

③[12]

$$Nu = 2 + 0.459\,\mathrm{Re}^{0.55}\,\mathrm{Pr}^{1/3} \tag{47}$$

④Ranz-Marshall[13]

$$Nu = 2 + 0.6\,\mathrm{Re}^{0.5}\,\mathrm{Pr}^{1/3} \tag{48}$$

⑤Kavanau-Drake[14]

$$Nu = \frac{2 + 0.459\,\mathrm{Re}^{0.55}\,\mathrm{Pr}^{0.33}}{1 + 3.42\left(\dfrac{M}{\mathrm{Re}\,\mathrm{Pr}}\right)\left(2 + 0.459\,\mathrm{Re}^{0.55}\,\mathrm{Pr}^{0.33}\right)} \tag{49}$$

⑥[12]

$$Nu = \left[\left(2 + 0.654\,\mathrm{Re}^{1/2}\,\mathrm{Pr}^{1/3}\right)^{-1} + 3.42\frac{M}{\mathrm{Re}\,\mathrm{Pr}}\right]^{-1} \tag{50}$$

In the above equations the Prandtl number is denoted by Pr.

The Eqs.(45)～(48) (①～④) are the formulae for an incompressible flow and Eqs.(49) and (50) (⑤～⑥) are those in which the compressibility and rarefaction effects are taken into account.

In Fig. 28 comparison of the Nusselt number for the incompressible flow and in Fig. 29 for the compressible flow is shown. The Prandtl number is set to 0.42 for a combustion gas.

In Fig. 28, the values of the Nusselt number are in general alike, except for that of ①. They produce some difference in the Re～10 neighborhood and in the high Reynolds number side of $Re>10^3$. The formula ② and ④ make a difference of about 1.5 times at $Re=10^4$. On the other hand, when compressibility is taken into account, the differences between methods are small. It turns out that the influence of compressibility is remarkable as shown in Fig. 29.

Next, the configuration of a motor of Fig. 30 is considered, and temperature change of the particle is analyzed for a quasi-one dimensional flow under conditions summarized in Table 3. Results are compared among the Nusselt number formulae shown previously. The formula of Crowe (Eq. (23)) is used for a drag coefficient.

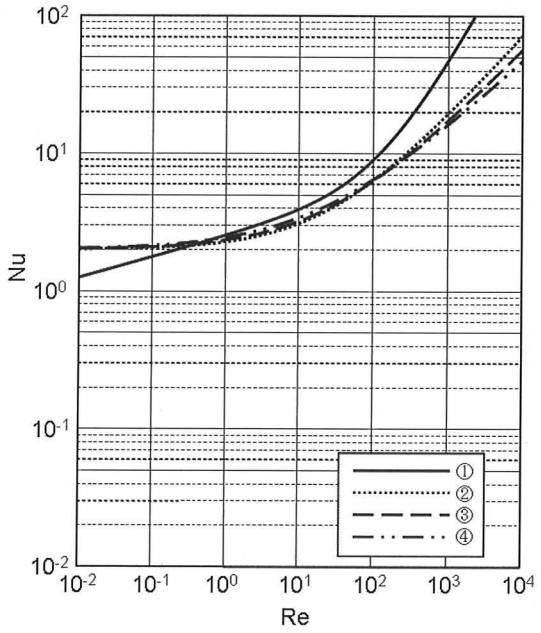

Fig. 28 Comparison of expressions for the Nusselt number

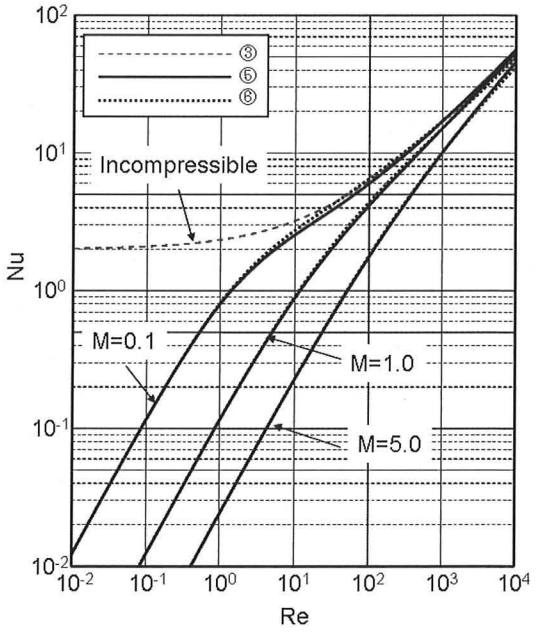

Fig. 29 Comparison of expressions for the Nusselt number

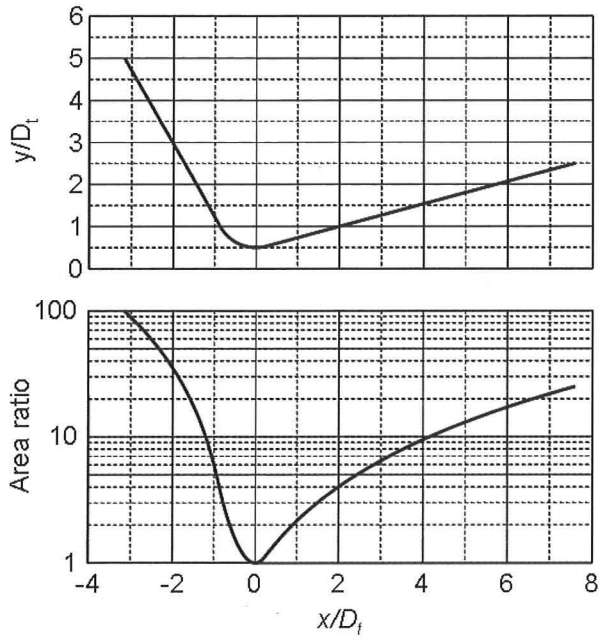

Fig. 30 Nozzle geometry used in quasi-one dimensional analysis

Table 3 Calculation conditions

Particle diameter	1, 10, 100μm
Particle density	2500 kg/m^3
Particle specific heat	1400 J/kg/K
Chamber pressure	10 MPa
Chamber temperature	3000 K
Specific heat ratio	1.2
Mean molecular weight	30 g/mol

The changes of particle temperature along the loci for the cases of particle diameter of 1, 10, and 100 micros are shown in Fig. 31, Fig. 32, and Fig. 33, respectively. Also the changes in the Nusselt number along the loci for the three cases are shown in Fig. 34, Fig. 35, and Fig. 36, respectively.

When the particle diameter is as small as 1 μm, there is little deference between the phases and also there is little variation in the Nusselt number evaluations. When the particle diameter is 10 μm, the results are divided into two groups whether the compressibility is considered or not. When the particle diameter becomes further large, the variation within the incompressible group becomes large. The level of variation is about 100～200K at the exit.

When the particle diameter is small, the inertia of the particle is small, and then a Nusselt number corresponding to a small Reynolds number is used because of a small slip velocity. The compressibility effect appears large because of this reason and, as shown in Fig. 34, the trend of change of the Nusselt number is roughly divided into two groups whether the compressibility is considered or not. However, as shown in Fig. 31, the difference between methods is not significant in the resulting particle temperature. As the particle diameter becomes large, a Nusselt number corresponding to a large Reynolds number is used, and then the compressibility effect becomes small. On the other hand, the variation in the incompressible Nusselt number among the evaluation methods becomes large, and so does that in the resulting particle temperature.

Non-uniformity term

When the mainstream is not uniform for a Stokes flow, Faxen force is added because of the non-uniformity. Similarly, in case of energy exchange, because of non-uniformity of the gaseous phase temperature in space, non-uniformity term of the following form is added.

$$Q_{c,nu} = \frac{\pi D_p{}^3 \lambda}{12} \nabla^2 T_g \tag{51}$$

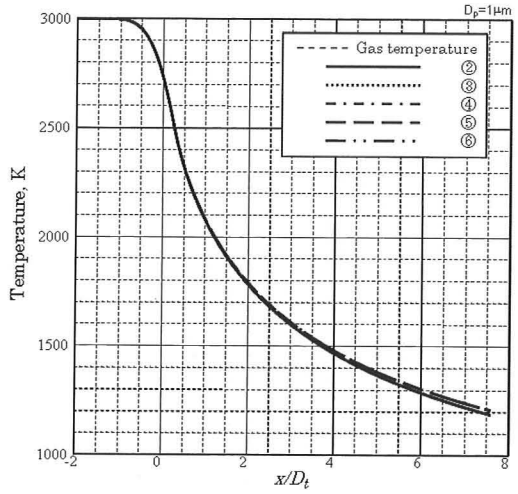

Fig. 31 Particle temperature (D_p = 1 μm)

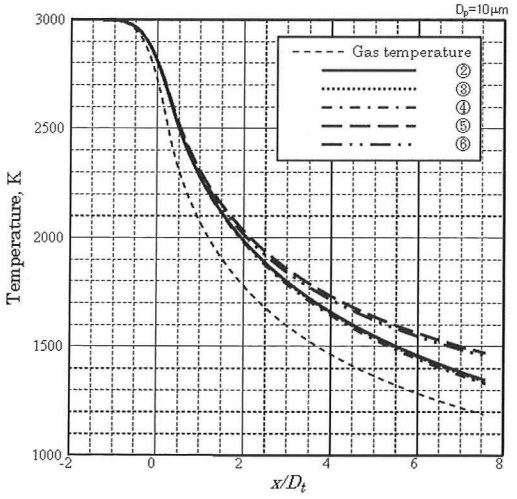

Fig. 32 Particle temperature (D_p = 10 μm)

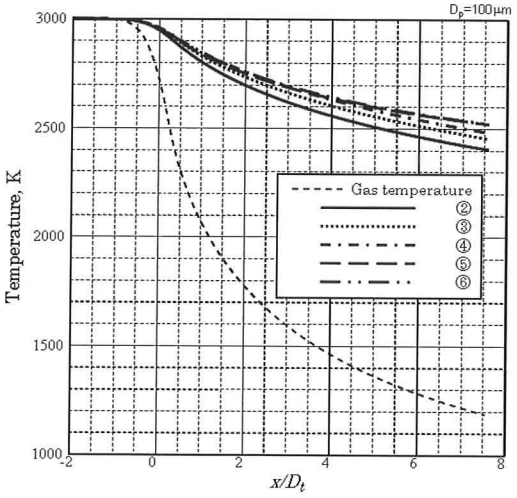

Fig. 33 Particle temperature (D_p = 100 μm)

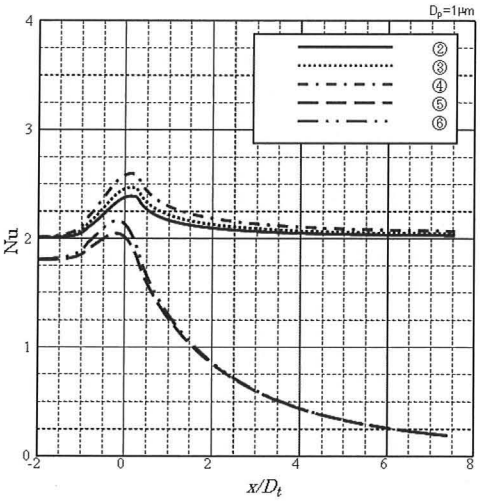

Fig. 34 Nusselt number (D_p = 1 μm)

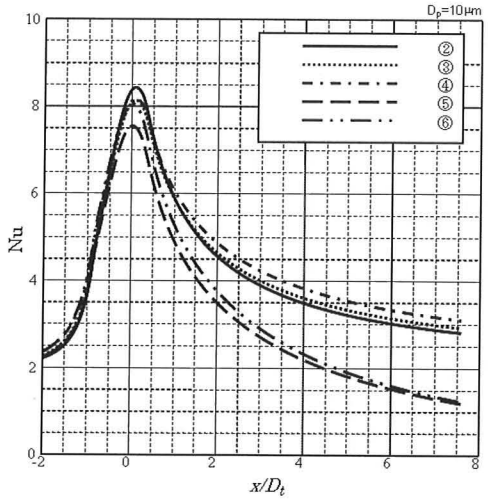

Fig. 35 Nusselt number (D_p = 10 μm)

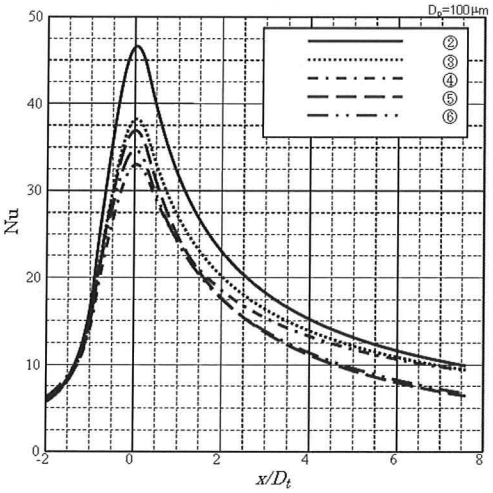

Fig. 36 Nusselt number (D_p = 100 μm)

Boundary-layer flow can be recognized as the case in which non-uniformity involves greatly. In order to investigate the influence of the non-uniformity of gaseous phase temperature to the particle temperature within a boundary layer, a flow-field model as shown in Fig. 14 is considered. The distribution of the transportation coefficient in the boundary layer is also set up based on the CFD analysis result.

The distributions of the temperature, the thermal conductivity (including turbulent effect), and $\lambda\nabla^2 T$ used for this model are shown in Fig. 37 and Fig. 38.

In order to see the influence of the non-uniformity term, a particle is placed in a flow field and the deceleration process is investigated as shown in Fig. 17. As shown in Fig. 37 and Fig. 38, $\lambda\nabla^2 T$ becomes large rapidly near the surface of a wall, and since it is possible to influence strongly in this portion, the situation where a particle is nearly touching the wall surface is considered. The particle temperature is calculated by numerically solving the energy equation, Eq.(39), with the particle motion obtained by solving the equation of motion with the formula of Crowe used for a drag coefficient and the force due to shear-stress gradient in a boundary layer considered. The results of the numerical experiment are

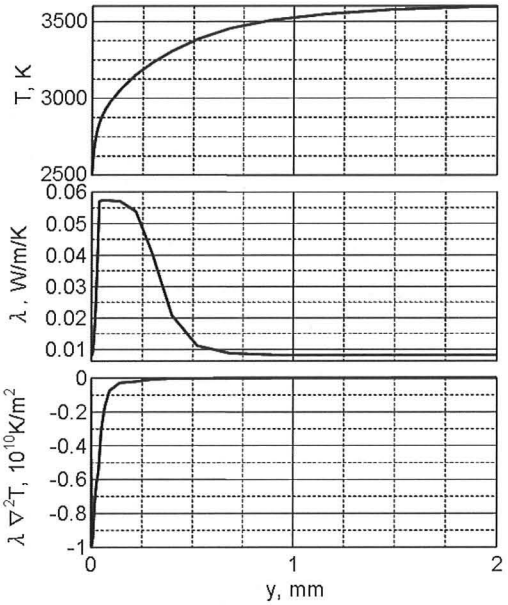

Fig. 37 Temperature, thermal conductivity, and $\lambda\nabla^2 T$ (boundary-layer-edge speed is about 100 m/s)

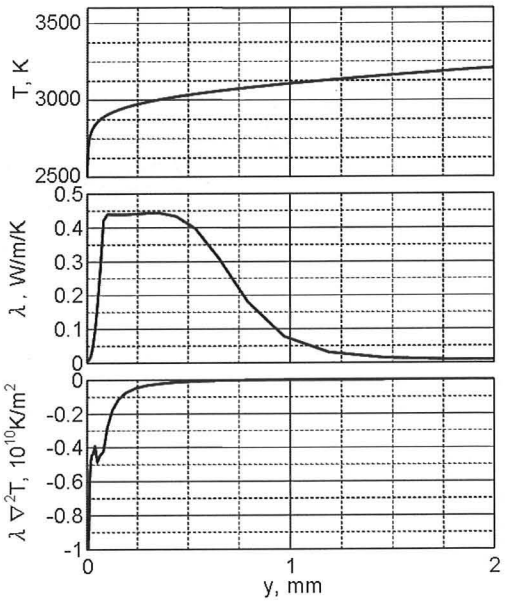

Fig. 38 Temperature, thermal conductivity, and $\lambda\nabla^2 T$ (near the throat)

shown in Fig. 39 and Fig. 40. The ratio of the particle temperature of the steady state evaluated with the non-uniformity effect taken into account to the gaseous phase temperature at the particle center is denoted by Ψ and is plotted against the particle diameter. From Fig. 39 and Fig. 40, it turns out that, when the speed at the outer-edge of the boundary layer is about 100 m/s, the degree of temperature decrease is about 0.5%, even with the most effective particle diameter, about 60 μm, to the non-uniformity of the temperature field. Moreover, for the case of the velocity profile near the throat, the decrease of the temperature of the particle is at most 0.3% in which the influence of non-uniformity appears most greatly with a particle diameter of about 10 μm or less. Within a boundary layer, since a small particle is located near the surface of a wall, it is put to a strong non-uniformity. On the other hand, since at the same time the volume of the particle becomes small, the steady-state term becomes dominant. It is considered that, with the particle diameter determined by the balance of the two effects, the influence of non-uniformity becomes the maximum. It is thought that the effect of non-uniformity is small enough compared with a steady-state term, and it is not necessary to take this effect into consideration in the SRM internal flow.

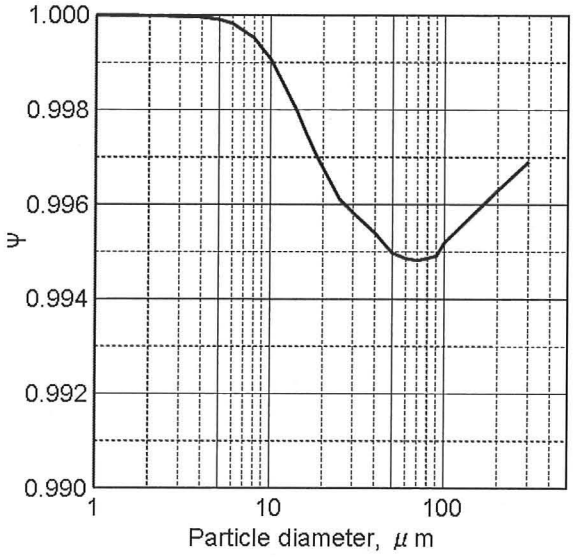

Fig. 39 Ratio of particle temperature to gas temperature due to non-uniformity term (boundary-layer-edge speed is about 100 m/s)

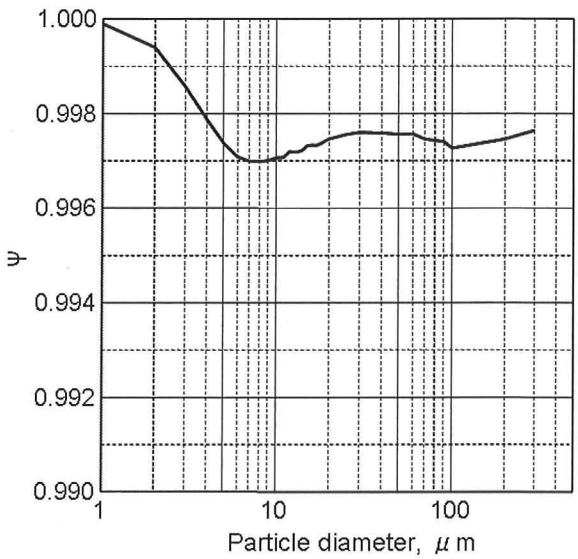

Fig. 40 Ratio of particle temperature to gas temperature due to non-uniformity term (near the throat)

Radiative heating

The energy exchange due to radiative heating is evaluated when a particle is surrounded by a gaseous body as[15]

$$Q_R = \varepsilon_p \sigma \pi D_p^{\,2} \left(T_g^{\,4} - T_p^{\,4} \right), \tag{52}$$

where ε_p denotes the emissivity of the particle and σ the Stefan-Boltzmann constant (5.670×10^{-8} (W/m^2/K^4)).

Similarly to the steady-state term in the convective heating, the particle temperature is analyzed about the SRM configuration of under the conditions of Table 3 for a quasi-one dimensional flow with or without the radiative heating. The Nusselt number is evaluated with the compressibility effect considered by the formula of Kavanau-Drake (Eq.(49)). The drag coefficient is evaluated by the formula of Crowe. The emissivity of a particle is set to 1 in order to see the maximum radiative heating effect.

The particle temperature evolution along particle loci is plotted in Fig. 41 ~ Fig. 43. The convective and radiative heating along the loci are also plotted in Fig. 44 ~ Fig. 46.

When particle diameter is small, since there is almost no slip temperature, no significant effect of radiation heating is seen. If particle diameter becomes as large as about 100 μm, the effect of radiation heating shows up since the slip temperature will become large. In the case of 100 μm of particle diameter, the effects by radiation are about 20K in this case at the nozzle exit. It is thought that the rate of convection heating is larger than that of radiation heating.

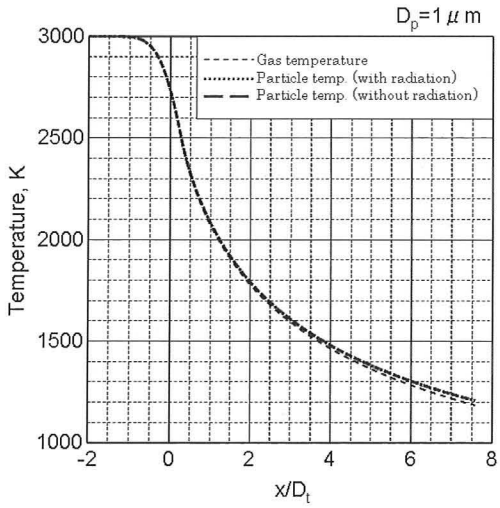

Fig. 41 Particle temperature (D_p = 1 μm)

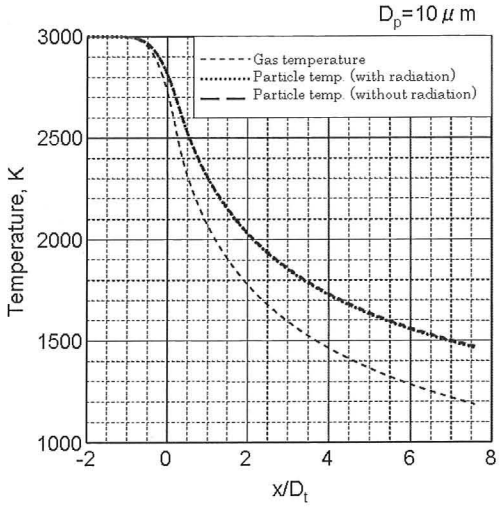

Fig. 42 Particle temperature (D_p = 10 μm)

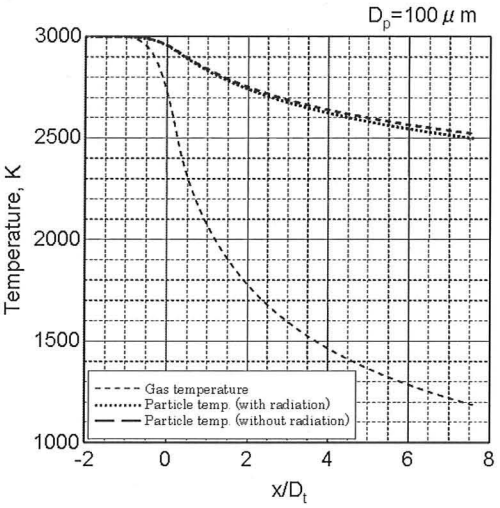

Fig. 43 Particle temperature (D_p = 100 μm)

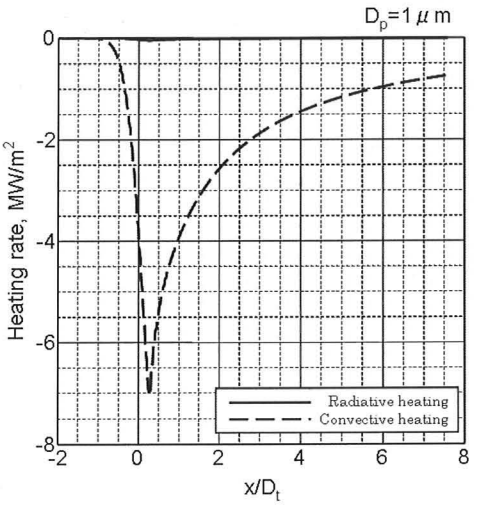

Fig. 44 Heating rate to particle (D_p = 1 μm)

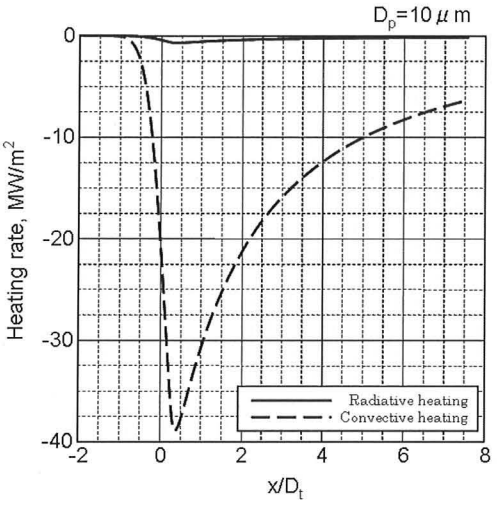

Fig. 45 Heating rate to particle (D_p = 10 μm)

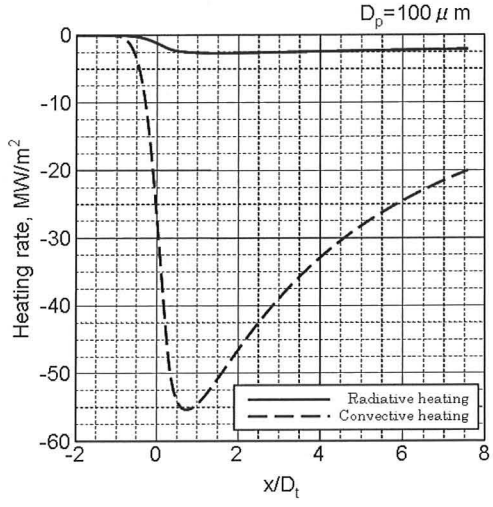

Fig. 46 Heating rate to particle (D_p = 100 μm)

3. Computational Method of multiphase Flow in SRM

About multiphase flows in SRM, a great number of researches have been carried out over the half-century including a lot of numerical analyses[16],[17],[18],[19],[20],[21],[22],[23],[24],[25],[26],[27].

In the computational analysis of a multiphase flow in SRM, governing equations for the conservation of the mass, momentum, and energy are solved for the gaseous phase and the dispersed-particle phase including their mutual, two-way coupling, interactions. Moreover, the following assumptions are made in the present numerical analysis of the multiphase flow in a solid rocket motor.

1) A particle does not undergo phase change.
2) Gas phase follows the ideal-gas equation of state.
3) Particle volume is negligible.
4) Particle random motion is negligible. (No effective pressure and stress in the particle phase.)
5) Particle coalescence effect is negligible.
6) Physical properties of particles are constant and not dependent of the temperature.
7) Particle is spherical.
8) Temperature is uniform in a particle.
9) Acceleration and gravity force are not taken into account.

As for the gaseous phase, it is common to be based on the Eulerian description in which the time and space are the independent variables, and the state variables such as density, pressure, and fluid velocity are the dependent variables. A phase-interaction term is added as a source term to the system of basic equations, i.e., the Navier-Stokes or Euler equation and the energy equation. No source term is added to the continuity equation.

On the other hand, in the description of particle phase, there are two kinds of methods, i.e., the Eulerian and the Lagrangian. The outline of both methods is shown in Fig. 47 and Fig. 48. In the Eulerian description, the particle phase is considered as a continuum, and the system of governing equations for the particle-phase conservations of mass, momentum, and energy with the gas-particle interaction source terms is simultaneously solved. On the other hand, in the Lagrangian approach, simulation particles are generated from the burning surface and the location and the temperature of each particle is updated by integrating in time the equation of motion with the energy equation. The influence on the gaseous phase is calculated by sampling particle information in each cell.

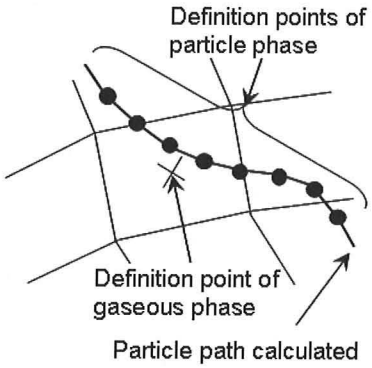

Fig. 47 Lagrangian method

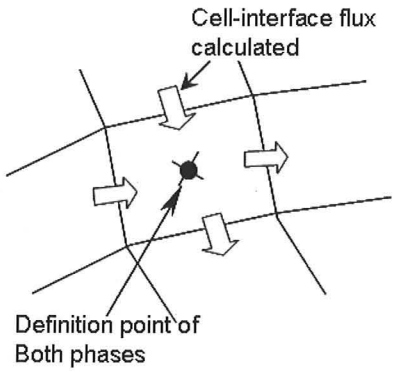

Fig. 48 Eulerian method

The Eulerian-Eulerian method, in which the particle-phase is treated by the Eulerian approach, is called two-fluid model. The Eulerian-Lagrangian method, in which the particle phase is treated by the Lagrangian approach, is called particle tracing method.

Furthermore, a hybrid technique which combines the two above-mentioned methods can be considered. Small particles like alumina smoke are treated in gaseous phase (Eulerian description), and comparatively large particles are treated by the Lagrangian method in a hybrid technique.

3.1. Eulerian-Eulerian method

3.1.1. Governing equations

The system of governing equations for the gas-particle flow containing N_p sorts of particle groups of different diameter is described below.

Governing equations for gaseous phase

$$\frac{\partial \mathbf{Q}_g}{\partial t}+\frac{\partial \mathbf{E}_g}{\partial x}+\frac{\partial \mathbf{F}_g}{\partial y}+\frac{\partial \mathbf{G}_g}{\partial z}=\mathbf{S}_g \tag{53}$$

$$\mathbf{Q}_g=\begin{pmatrix}\rho_g\\ \rho_g u_g\\ \rho_g v_g\\ \rho_g w_g\\ e_g\end{pmatrix}\quad \mathbf{E}_g=\begin{pmatrix}\rho_g u_g\\ \rho_g u_g^2+p\\ \rho_g u_g v_g\\ \rho_g u_g w_g\\ (e_g+p)u_g\end{pmatrix}\quad \mathbf{F}_g=\begin{pmatrix}\rho_g v_g\\ \rho_g u_g v_g\\ \rho_g v_g^2+p\\ \rho_g v_g w_g\\ (e_g+p)v_g\end{pmatrix}\quad \mathbf{G}_g=\begin{pmatrix}\rho_g w_g\\ \rho_g u_g w_g\\ \rho_g v_g w_g\\ \rho_g w_g^2+p\\ (e_g+p)w_g\end{pmatrix} \tag{54}$$

$$\mathbf{S}_g=\begin{pmatrix}0\\ -\sum_{k=1}^{N_p}A^{(k)}(u_g-u_p^{(k)})\\ -\sum_{k=1}^{N_p}A^{(k)}(v_g-v_p^{(k)})\\ -\sum_{k=1}^{N_p}A^{(k)}(w_g-w_p^{(k)})\\ -\sum_{k=1}^{N_p}\left[A^{(k)}\left\{u_p^{(k)}(u_g-u_p^{(k)})+v_p^{(k)}(v_g-v_p^{(k)})+w_p^{(k)}(w_g-w_p^{(k)})\right\}+B^{(k)}(T_g-T_p^{(k)})\right]\end{pmatrix} \tag{55}$$

Here, ρ denotes the density, (u, v, w) the components of velocity in x, y, and z directions, respectively, p the pressure, T the temperature, and e the total energy per unit volume. The subscripts, g and p designate the gaseous phase and the particle phase, respectively. The superscript (k) denotes the k-th particle group. Coefficients A and B in the phase-interaction term are defined in Eqs.(65) and (70).

The pressure and the temperature are determined from the equation of state.

$$p=(\gamma-1)\left(e_g-\tfrac{1}{2}\rho_g(u_g^2+v_g^2+w_g^2)\right),\qquad T_g=p/\rho_g R \tag{56}$$

Governing equations for the k-th particle phase ($k=1,\ldots,N_p$)

$$\frac{\partial \mathbf{Q}_p^{(k)}}{\partial t}+\frac{\partial \mathbf{E}_p^{(k)}}{\partial x}+\frac{\partial \mathbf{F}_p^{(k)}}{\partial y}+\frac{\partial \mathbf{G}_p^{(k)}}{\partial z}=\mathbf{S}_p^{(k)} \tag{57}$$

$$\mathbf{Q}_p^{(k)} = \begin{pmatrix} \rho_p^{(k)} \\ \rho_p^{(k)} u_p^{(k)} \\ \rho_p^{(k)} v_p^{(k)} \\ \rho_p^{(k)} w_p^{(k)} \\ e_p^{(k)} \end{pmatrix} \quad \mathbf{E}_p^{(k)} = \begin{pmatrix} \rho_p^{(k)} u_p^{(k)} \\ \rho_p^{(k)} u_p^{(k)} u_p^{(k)} \\ \rho_p^{(k)} u_p^{(k)} v_p^{(k)} \\ \rho_p^{(k)} u_p^{(k)} w_p^{(k)} \\ e_p^{(k)} u_p^{(k)} \end{pmatrix} \quad \mathbf{F}_p^{(k)} = \begin{pmatrix} \rho_p^{(k)} v_p^{(k)} \\ \rho_p^{(k)} u_p^{(k)} v_p^{(k)} \\ \rho_p^{(k)} v_p^{(k)} v_p^{(k)} \\ \rho_p^{(k)} v_p^{(k)} w_p^{(k)} \\ e_p^{(k)} v_p^{(k)} \end{pmatrix} \quad \mathbf{G}_p^{(k)} = \begin{pmatrix} \rho_p^{(k)} w_p^{(k)} \\ \rho_p^{(k)} u_p^{(k)} w_p^{(k)} \\ \rho_p^{(k)} v_p^{(k)} w_p^{(k)} \\ \rho_p^{(k)} w_p^{(k)} w_p^{(k)} \\ e_p^{(k)} w_p^{(k)} \end{pmatrix} \tag{58}$$

$$\mathbf{S}_p^{(k)} = \begin{pmatrix} 0 \\ A^{(k)}(u_g - u_p^{(k)}) \\ A^{(k)}(v_g - v_p^{(k)}) \\ A^{(k)}(w_g - w_p^{(k)}) \\ A^{(k)}\left(u_p^{(k)}(u_g - u_p^{(k)}) + v_p^{(k)}(v_g - v_p^{(k)}) + w_p^{(k)}(w_g - w_p^{(k)})\right) + B^{(k)}(T_g - T_p^{(k)}) \end{pmatrix} \tag{59}$$

Here ρ_p is the particle bulk density. The total energy per unit volume of the particle phase is described as

$$e_p = \rho_p C_{Pp} T_p + \tfrac{1}{2}\rho_p (u_p^2 + v_p^2 + w_p^2), \tag{60}$$

where C_{Pp} is the specific heat of the particle.

Phase-interaction term

It is necessary to evaluate the phase-interaction term in the simultaneous solution process of Eqs. (53) and (57). For the simplicity, N_p is set to unity later on.

The force acting on a single particle is evaluated as

$$\vec{f} = \frac{1}{2}\rho_g \left|\vec{U}_s\right| S_{ref} C_D \left(\vec{U}_g - \vec{U}_p\right), \tag{61}$$

$$\left|\vec{U}_s\right| = \sqrt{(u_g - u_p)^2 + (v_g - v_p)^2 + (w_g - w_p)^2}, \tag{62}$$

where C_D is a drag coefficient per a single particle.

Since the number density is determined as the ratio of the particle bulk density to the mass per a particle, the force acting on the particles per unit volume can be calculated as

$$\vec{F} = \vec{f}\,\frac{\rho_p}{\sigma_m V_p} = \tfrac{1}{2}\rho_g \left|\vec{U}_s\right| S_{ref}\; C_D\; (\vec{U}_g - \vec{U}_p)\,\frac{\rho_p}{\sigma_m V_p}, \tag{63}$$

where σ_m is the density of particle material and V_p the volume of a particle.

Assuming a spherical particle, the above equation can be rewritten with replacing S_{ref} by the projected area of a sphere πr_p^2 as

$$\vec{F} = A\,(\vec{U}_g - \vec{U}_p) \tag{64}$$

$$A = \frac{3}{8}\frac{\rho_p \rho_g}{\sigma_m}\left|\vec{U}_s\right| C_D \frac{1}{r_p}, \tag{65}$$

where r_p is the radius of the particle.

The energy exchange between the phases can be described as follows. First, the convective heat transfer to the surface of a particle is considered. The heat transfer coefficient is written with the Nusselt number, Nu as

$$h = \frac{Nu\,\lambda}{L} = \frac{Nu\,c_p\,\mu}{L\,\mathrm{Pr}}, \tag{66}$$

where h denotes the heat transfer coefficient, λ the thermal conductivity of gas, c_p the specific heat of gas at constant pressure, L a reference length, and Pr the Prandtl number.

Designating the surface area of a particle by S_{sur}, the energy amount q received by a single particle from the gaseous phase can be calculated as

$$q = h S_{sur}(T_g - T_p) = \frac{Nu\,c_p\,\mu}{L\,\mathrm{Pr}} S_{sur}(T_g - T_p). \tag{67}$$

Similarly to the force, the energy amount Q received by the particle-phase per unit volume from the gaseous phase is

$$Q = q\frac{\rho_p}{\rho_m V_p} = \frac{Nu\,c_p\,\mu}{L\,\mathrm{Pr}} S_{sur}(T_g - T_p)\frac{\rho_p}{\rho_m V_p}. \tag{68}$$

Replacing L by the particle diameter, the above equation can be written as

$$Q = B(T_g - T_p), \tag{69}$$

$$B = \frac{3}{2}\frac{\rho_p}{\sigma_m r_p^2}\frac{Nu\,c_p\,\mu}{\mathrm{Pr}}. \tag{70}$$

3.1.2. Phase-equilibrium flow

Let us consider a case in which the diameter of a particle is so small that speed and temperature of the particle phase follow immediately with those of the gaseous phase. Such a flow is called the phase-equilibrium flow. The Stokes number is usually very small in such a case.

Let us consider the governing equations for the two-phase flow, Eqs. (53) and (57) with $N_p = 1$. In a phase-equilibrium flow, the velocity and the temperature are common in both phases, i.e.,

$$(u_p \quad v_p \quad w_p) = (u_g \quad v_g \quad w_g) = (u \quad v \quad w) \tag{71}$$

$$T_p = T_g = T \tag{72}$$

By summing up Eqs. (53) and (57) and inserting Eqs. (71) and (72), a system of equations for a phase-equilibrium flow is obtained as

$$\frac{\partial \mathbf{Q}}{\partial t} + \frac{\partial \mathbf{E}}{\partial x} + \frac{\partial \mathbf{F}}{\partial y} + \frac{\partial \mathbf{G}}{\partial z} = 0, \tag{73}$$

$$\mathbf{Q} = \begin{pmatrix} \rho \\ \rho u \\ \rho v \\ \rho w \\ e \end{pmatrix} \quad \mathbf{E} = \begin{pmatrix} \rho u \\ \rho u^2 + p \\ \rho uv \\ \rho uw \\ (e+p)u \end{pmatrix} \quad \mathbf{F} = \begin{pmatrix} \rho v \\ \rho uv \\ \rho v^2 + p \\ \rho vw \\ (e+p)v \end{pmatrix} \quad \mathbf{G} = \begin{pmatrix} \rho w \\ \rho uw \\ \rho vw \\ \rho w^2 + p \\ (e+p)w \end{pmatrix}. \tag{74}$$

It should be noticed that the source terms are cancelled out. The density and total energy of the phase-equilibrium flow are defined as follows.

$$\rho = \rho_g + \rho_p \tag{75}$$

$$e = e_g + e_p \tag{76}$$

Let us define the loading ratio of the particle as the ratio of the particle bulk density to the gaseous-phase density and designate it by ψ.

$$\psi = \frac{\rho_p}{\rho_g} \tag{77}$$

The particle bulk density can be written as

$$\rho_p = \psi\rho_g = \frac{\psi}{1+\psi}\rho\,. \tag{78}$$

Since Eqs. (73) and (74) are formally the same as the equations of compressive fluid, a phase-equilibrium flow can be treated as a single-species gas flow.

The total energy of a phase-equilibrium flow is obtained by summing up the total energy of the two phases.

$$\begin{aligned} e &= e_p + e_g \\ &= \rho_p C_{Pp} T + \frac{p}{\gamma - 1} + \frac{\rho}{2}\left(u^2 + v^2 + w^2\right) \\ &= \psi\rho_g C_{Pp} T + \frac{p}{\gamma - 1} + \frac{\rho}{2}\left(u^2 + v^2 + w^2\right) \\ &= \left(\frac{\psi C_{Pp}}{R} + \frac{1}{\gamma - 1}\right)p + \frac{\rho}{2}\left(u^2 + v^2 + w^2\right) \end{aligned} \tag{79}$$

Moreover, the equation of state can be described as

$$p = \rho_g RT = \frac{1}{1+\psi}\rho RT\,. \tag{80}$$

Introducing the effective specific heat ratio $\bar{\gamma}$ and gas constant $\bar{R}$ for a phase-equilibrium flow, it is possible to treat the flow by a usual single-phase, ideal-gas compressible fluid.

$$e = \frac{1}{\bar{\gamma} - 1}p + \frac{\rho}{2}\left(u^2 + v^2 + w^2\right) \tag{81}$$

$$p = \rho\bar{R}T \tag{82}$$

Comparing Eqs.(79)～(82), the effective properties can be defined as

$$\frac{1}{\bar{\gamma} - 1} = \frac{1}{\gamma - 1} + \frac{\psi C_{Pp}}{R}, \tag{83}$$

$$\bar{R} = \frac{1}{1+\psi}R\,. \tag{84}$$

Phase-equilibrium flow analyses are utilized to investigate the multiphase flow behavior containing very fine particles like an alumina smoke or to supply the initial flow field of non-equilibrium multiphase flow calculation.

3.1.3. Outline of numerical simulation method

A computer program is developed along with the Eulerian-Eulerian method to calculate multiphase flow in SRM. The program is named SPEC-1 (Solid Propulsion Enhanced Code, No.1).

In the Eulerian method, the governing partial differential equations (53) and (57) are discretized by a finite volume method to deduce a system of ordinary differential equations, which is then integrated in time by an implicit scheme to give a system of algebraic equations.

The computational domain is divided into finite-volume cells, as shown in Fig. 49, and volume-averaged quantities of $\mathbf{Q}_g$, $\mathbf{Q}_p$ are defined per each cell. The instantaneous fluxes of conservation variables at the interface of each cell are calculated to give the time derivative of each variable. The amount of change is calculated by numerically integrating the derivative by an appropriate time interval. By successively performing the above procedure, Eqs. (53) and (57) are solved in a time-evolutional manner. A steady-state solution, when it is concerned, is obtained as the time-asymptotic solution reached after sufficient number of iterations.

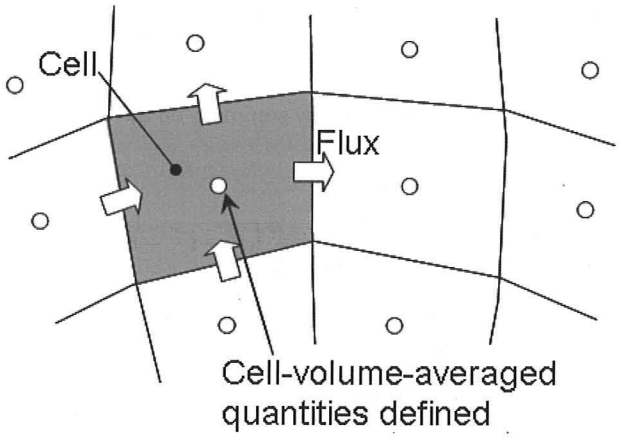

Fig. 49 Computation scheme of Eulerian method

Calculation of the numerical flux

As for gaseous phase, several methods are proposed for the numerical flux of the convection term of compressive fluid. In SPECS (Solid Propulsion Enhanced Code Series), the AUSM-DV-EF method[28],[29], with MUSCL approach and second- or third-order reconstruction, is commonly used as the convective numerical flux scheme. In the MUSCL approach, a limiter, e.g., minmod function, is used for extrapolating the primitive variables. Details of the method are available in Ref. 28 and Ref. 29.

Numerical flux of the particle advection term in Eq. (57) will be described below. It is calculated by solving a Riemann problem at each cell interface.

Let us consider one-dimensional governing equations. The conservation variable vector and the advection flux vector for the particle phase can be written as

$$\mathbf{q}_p = \begin{bmatrix} \rho_p \\ \rho_p u_p \\ \rho_p \varepsilon_p \end{bmatrix} \quad \text{and} \quad \mathbf{F}_p = \begin{bmatrix} \rho_p u_p \\ \rho_p u_p^2 \\ \rho_p \varepsilon_p u_p \end{bmatrix} = u_p \mathbf{q}_p \,. \tag{85}$$

The Jacobian matrix of the advection flux vector with respect to the conservation variable vector is calculated as

$$\mathbf{A}_p \equiv \frac{\partial \mathbf{F}_p}{\partial \mathbf{q}_p} = \begin{bmatrix} 0 & 1 & 0 \\ -u_p^2 & 2u_p & 0 \\ -\varepsilon_p u_p & \varepsilon_p & u_p \end{bmatrix}. \tag{86}$$

The eigenvalues of $\mathbf{A}_p$ are u_p, u_p, and u_p. The speed of information of particle phase is, therefore, only the particle velocity. This system of partial differential equations is hyperbolic and degenerative. Because of this degenerative nature, the particle-free zone appears in the solution and also the density is piled up where the particle is colliding to the wall or each other.

In the Riemann problem, the left-side and the right-side particle velocity at a cell interface are denoted by u_{pL} and u_{pR}, respectively.

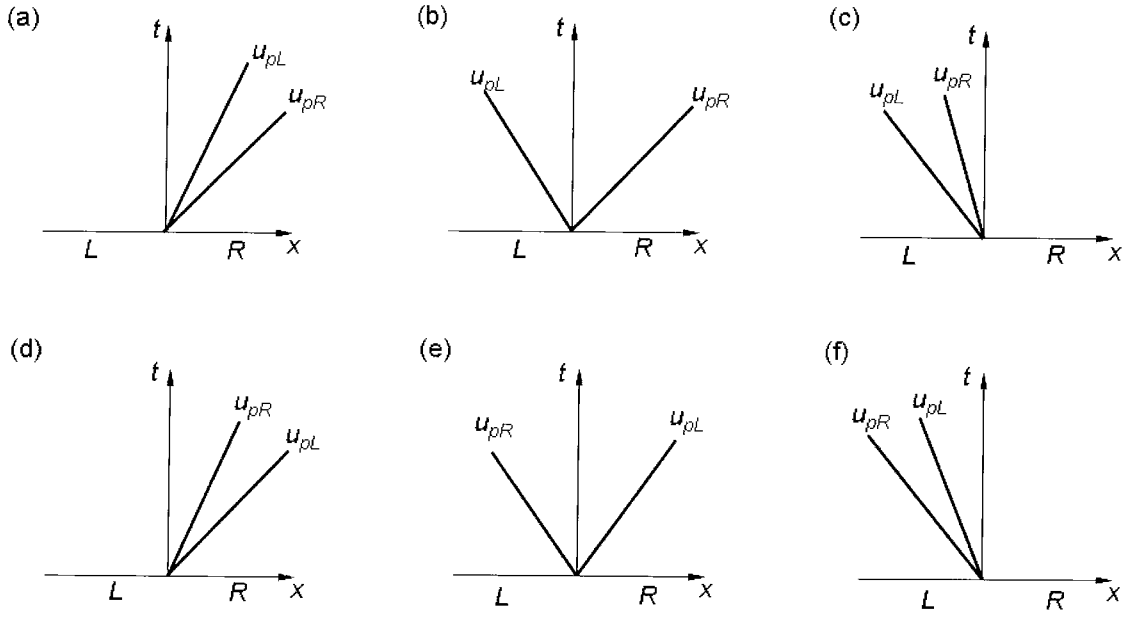

Fig. 50 Six states in the Riemann problem of particle phase

The Riemann problem at a cell interface can be categorized into six kinds of the left-side and right-side states as shown in Fig. 50. In the states of (a), (b), and (c), the left particle and the right particle are separating, so they are "expansion" cases. On the other hand, the states of (d), (e), and (f) are "compression" cases.

The particle bulk density ρ^* and the velocity u^* at a cell interface are determined based on the solutions of the Riemann problem.

(a) $u_{pL} > 0$, $u_{pR} > 0$, $u_{pL} < u_{pR}$: $\rho^* = \rho_{pL}$, $u^* = u_{pL}$ (87)

(b) $u_{pL} < 0$, $u_{pR} > 0$: $\rho^* = 0$ (88)

(c) $u_{pL} < 0$, $u_{pR} < 0$, $u_{pL} < u_{pR}$: $\rho^* = \rho_{pR}$, $u^* = u_{pR}$ (89)

(d) $u_{pL} > 0$, $u_{pR} > 0$, $u_{pL} > u_{pR}$: $\rho^* = \rho_{pL}$, $u^* = u_{pL}$ (90)

(e) $u_{pL} > 0$, $u_{pR} < 0$: $\rho^* = \rho_{pL} + \rho_{pR}$, $u^* = \left(\rho_{pL} u_{pL} + \rho_{pR} u_{pR}\right) / \left(\rho_{pL} + \rho_{pR}\right)$ (91)

(f) $u_{pL} < 0$, $u_{pR} < 0$, $u_{pL} > u_{pR}$: $\rho^* = \rho_{pR}$, $u^* = u_{pR}$ (92)

The numerical flux for the particle phase becomes

$$\mathbf{F}_p{}^* = \begin{bmatrix} \rho^* u^* \\ \rho^* u^* u^* \\ \rho^* \varepsilon^* u^* \end{bmatrix}. \tag{93}$$

The total energy ε^* can be evaluated in the same manner as ρ^*.

The numerical flux can be expressed in a different form, which is more convenient in practice.

$$\mathbf{F}_p{}^* = \mathbf{F}_{pL} + \mathbf{F}_{pR} = u_p^+ \mathbf{q}_{pL} + u_p^- \mathbf{q}_{pR} \tag{94}$$

$$u_p^+ = \frac{1}{2}\left(u_{pL} + |u_{pL}|\right) \tag{95}$$

$$u_p^- = \frac{1}{2}\left(u_{pR} - |u_{pR}|\right) \tag{96}$$

In order to attain higher order accuracy in space, the variation of the physical quantities within a cell is considered, and the values of the right and the left sides of an interface are reconstructed from discrete cell-averaged quantities of neighboring cells. The reconstruction is done assuming a linear or parabolic distribution of physical quantities within a cell with a slope limiter in order to meet the monotonicity constraint among the left, intermediate, and right values at each cell interface.

Calculation of the phase-interaction term

The phase-interaction term does not include the derivatives of properties, and can be calculated in a straightforward manner as a source term.

Method of time-wise integration

An implicit method is used for time integral calculus mainly for the purpose of obtaining a steady-state solution efficiently. The LU-SGS method[30] which is efficient in this operation is used here. In the LU-SGS method, the implicit operator, a block tri-diagonal matrix, is decomposed into a product of upper- and lower- triangular matrices based on an idea of upwind differencing. Furthermore, in the process of LU-decomposition, by taking the spectral radius as a common speed of information about all characteristic waves, number of operations is remarkably reduced.

Boundary conditions

Solid wall: For both the gaseous phase and the particle phase, mirror-image values are set in a virtual cell with a velocity-slip condition. In this case, the particle which has reached the surface of a wall loses the speed of the wall-normal direction, and flows tangentially to the wall. In addition, boundary conditions under which a wall adsorbs the particle reaching the wall can also be given. In the Eulerian method, it is inherently difficult to set up a boundary condition under which a particle carries out specular reflection with a wall.

Axis of center: As for the axis of revolution in an axisymmetric calculation, since the boundary surface area vanishes there, all the fluxes are set to zero.

Nozzle exit: Usually, at a nozzle exit, since combustion gas is discharged at supersonic speed, all quantities of both the gaseous phase and the particle phase are extrapolated from the inside of the computational domain (supersonic outflow condition).

Burning surface: The density, velocity, pressure, and temperature are determined as follows.

$$\rho_{gb} = \frac{p_c}{T_c R} \tag{97}$$

$$u_{gb} = \frac{\dot{m}}{\rho_{gb}(1+\psi)} \tag{98}$$

$$p_{gb} = p_c \tag{99}$$

$$\rho_{pb} = \psi \rho_{gb} \tag{100}$$

$$u_{pb} = u_{gb} \tag{101}$$

$$T_{pb} = T_c \tag{102}$$

Here the subscript b denotes the value applied to a virtual cell as boundary conditions and the subscript c does the combustion chamber quantities given as inputs from the outside. The total mass flux of the gaseous and the particle phases at the burning surface is denoted by $\dot{m}$. The loading ratio ψ is defined in Eq. (77). The total mass flux is determined either from the relationship

$$\dot{m} = \dot{r}_b \sigma_p , \tag{103}$$

or from

$$\dot{m} = \frac{p_c}{c^*} \frac{A_t}{A_b}, \tag{104}$$

where $\dot{r}_b$ is linear burning rate, σ_p the propellant density, c^* the characteristic discharge velocity, A_t the throat area, and A_b the burning surface area. The direction of the velocity at the burning surface is set normal to the surface.

3.1.4. Details of numerical simulation of a two-dimensional axisymmetric gas-particle flow

The solution method and demonstration of SPEC-1 (Solid Propulsion Enhanced Code No.1) computer code will be described. The SPEC-1 is an Eulerian-Eulerian axisymmetric two-phase flow program.

Governing equations

The governing equations for the axisymmetric two-phase flow can be written in a semi-conservation form as follows. It should be noticed that the radial coordinate r is included in conservation variables, fluxes, and source terms.

$$\frac{\partial \mathbf{q}}{\partial t} + \frac{\partial \mathbf{E}}{\partial x} + \frac{\partial \mathbf{F}}{\partial r} = \mathbf{S}$$

$$\mathbf{q} = \begin{bmatrix} r\rho_g \\ r\rho_g u_g \\ r\rho_g v_g \\ r\rho_g \varepsilon_g \\ r\rho_p \\ r\rho_p u_p \\ r\rho_p v_p \\ r\rho_p \varepsilon_p \end{bmatrix}, \quad \mathbf{E} = \begin{bmatrix} r\rho_g u_g \\ r(\rho_g u_g^2 + p) \\ r\rho_g v_g u_g \\ r\rho_g u_g H \\ r\rho_p u_p \\ r\rho_p u_p^2 \\ r\rho_p v_p u_p \\ r\rho_p \varepsilon_p u_p \end{bmatrix}, \quad \mathbf{F} = \begin{bmatrix} r\rho_g v_g \\ r\rho_g u_g v_g \\ r(\rho_g v_g^2 + p) \\ r\rho_g v_g H \\ r\rho_p v_p \\ r\rho_p u_p v_p \\ r\rho_p v_p^2 \\ r\rho_p \varepsilon_p v_p \end{bmatrix} \tag{105}$$

$$\mathbf{S}=\begin{bmatrix} 0 \\ -r\dfrac{\rho_p}{\tau_v}(u_g-u_p) \\ p-r\dfrac{\rho_p}{\tau_v}(v_g-v_p) \\ -r\left\{\dfrac{\rho_p C_{Pp}}{\tau_T}(T_g-T_p)+\dfrac{\rho_p}{\tau_v}\left[(u_g-u_p)u_p+(v_g-v_p)v_p\right]\right\} \\ 0 \\ r\dfrac{\rho_p}{\tau_v}(u_g-u_p) \\ r\dfrac{\rho_p}{\tau_v}(v_g-v_p) \\ r\left\{\dfrac{\rho_p C_{Pp}}{\tau_T}(T_g-T_p)+\dfrac{\rho_p}{\tau_v}\left[(u_g-u_p)u_p+(v_g-v_p)v_p\right]\right\} \end{bmatrix} \tag{106}$$

Here, (u_g, v_g) are the gaseous-phase velocity components in (x, r) directions. Again, N_p is assumed to be 1. The total energy per unit mass of the gaseous phase ε_g and the total enthalpy H are

$$\begin{aligned} \varepsilon_g &= \frac{1}{\gamma-1}\frac{p}{\rho_g}+\frac{1}{2}(u_g^2+v_g^2), \\ H &= \varepsilon_g+\frac{p}{\rho_g}. \end{aligned} \tag{107}$$

The total energy per unit mass of the particle phase ε_p is

$$\varepsilon_p = C_{Pp}T_p+\frac{1}{2}\left(u_p^2+v_p^2\right). \tag{108}$$

The velocity and the temperature relaxation times are determined as follows.

$$\tau_V = \frac{4}{3}\frac{\sigma_m D_p^2}{\mathrm{Re}_r\,\mu C_D} \tag{109}$$

$$\tau_T = \frac{c\sigma_m D_p^2}{6\mathrm{Nu}\lambda_g} \tag{110}$$

Discretization by a finite volume method

Let us consider a quadrangle cell in the computational domain as shown in Fig. 51. It is numbered by (i, j). The governing equation Eq. (105) is integrated over the cell-projected area $A_{i,j}$ as

$$\iint_{A_{i,j}}\left(\frac{\partial \mathbf{q}}{\partial t}+\frac{\partial \mathbf{E}}{\partial x}+\frac{\partial \mathbf{F}}{\partial r}\right)dx\,dr = \iint_{A_{i,j}}\mathbf{S}\,dx\,dr \tag{111}$$

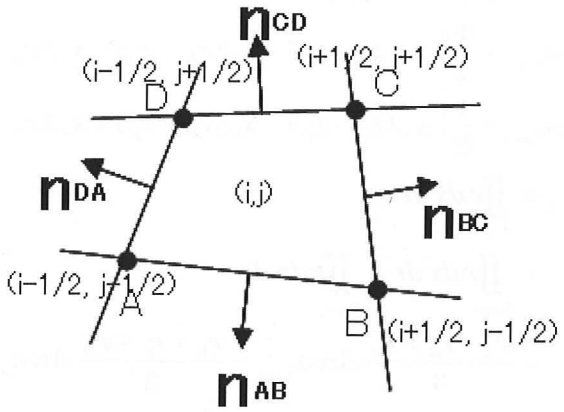

Fig. 51 Cell, cell interface, and surface normal vector, projected on $x-r$ plane

The convection term in the left-hand side of Eq.(111) is transformed by the Gauss' divergence theorem to an integral over the circumference $\partial A_{i,j}$ of the projected area $A_{i,j}$.

$$\iint_{A_{i,j}} \frac{\partial \mathbf{q}}{\partial t} dx\, dr + \oint_{\partial A_{i,j}} (n_x \mathbf{E} + n_r \mathbf{F}) ds = \iint_{A_{i,j}} \mathbf{S}\, dx\, dr \tag{112}$$

where, the element ds is along the interface $\partial A_{i,j}$ and its positive direction is determined so that the internal domain is looked on the left from an observer facing the positive direction. Outbound unit normal vector of the interface is denoted by $\mathbf{n} \equiv (n_x, n_r)$. As shown in Fig. 51, the interface $\partial A_{i,j}$ consists of four line segments, AB, BC, CD, and DA. Given the coordinates of the four vertexes, four unit normal vectors $\mathbf{n}_{AB}$, $\mathbf{n}_{BC}$, $\mathbf{n}_{CD}$, and $\mathbf{n}_{DA}$ are determined.

For example, defining

$$\begin{aligned} \Delta x_{AB} &\equiv x_B - x_A \\ \Delta r_{AB} &\equiv r_B - r_A \end{aligned}, \tag{113}$$

and denoting the length of AB by $|AB|$, one can calculate $\mathbf{n}_{AB}$ by the following vector product

$$\mathbf{n}_{AB} = \left(\frac{\Delta x_{AB}}{|AB|}, \frac{\Delta r_{AB}}{|AB|}, 0\right) \times (0,0,1) = \left(\frac{\Delta r_{AB}}{|AB|}, -\frac{\Delta x_{AB}}{|AB|}, 0\right). \tag{114}$$

Now, in order to discretize the time-derivative term and the source term, cell-volume averaged quantities are defined as

$$\overline{\mathbf{q}}_{i,j} \equiv \frac{\iint_{A_{i,j}} \mathbf{q}\, dx\, dr}{\iint_{A_{i,j}} r\, dx\, dr} = \frac{\iint_{A_{i,j}} \mathbf{q}\, dx\, dr}{Vol_{i,j}}. \tag{115}$$

$$\overline{\mathbf{S}}_{i,j} \equiv \frac{\iint_{A_{i,j}} \mathbf{S}\, dx\, dr}{\iint_{A_{i,j}} r dx\, dr} = \frac{\iint_{A_{i,j}} \mathbf{S}\, dx\, dr}{Vol_{i,j}} \tag{116}$$

It is noted that the radius r is not included in $\overline{\mathbf{q}}_{i,j}$ and $\overline{\mathbf{S}}_{i,j}$.

The projected area $A_{i,j}$ and the volume of a cell $Vol_{i,j}$ are calculated as

$$
\begin{aligned}
A_{i,j} &= Area_{\Delta_{ABD}} + Area_{\Delta_{BCD}} \\
Area_{\Delta_{ABD}} &= \frac{1}{2}\left\{ x_A(r_B - r_D) + x_B(r_D - r_A) + x_D(r_A - r_B)\right\}, \\
Area_{\Delta_{BCD}} &= \frac{1}{2}\left\{ x_B(r_C - r_D) + x_C(r_D - r_B) + x_D(r_B - r_C)\right\}
\end{aligned} \tag{117}
$$

$$
\begin{aligned}
Vol_{i,j} &\equiv \iint_{A_{i,j}} r\,dx\,dr \\
&= \iint_{\Delta_{ABD}} r\,dx\,dr + \iint_{\Delta_{BCD}} r\,dx\,dr \\
&= \frac{r_A + r_B + r_D}{3} Area_{\Delta_{ABD}} + \frac{r_B + r_C + r_D}{3} Area_{\Delta_{BCD}}
\end{aligned} \tag{118}
$$

Inserting Eqs. (115) and (116) into Eq. (111), the following is obtained.

$$
Vol_{i,j}\frac{d\overline{\mathbf{q}}_{i,j}}{dt} + \oint_{\partial A_{i,j}} (n_x \mathbf{E} + n_r \mathbf{F}) ds = Vol_{i,j}\overline{\mathbf{S}}_{i,j} \tag{119}
$$

Next, the convection term is written as

$$
\widetilde{\mathbf{E}} \equiv n_x \mathbf{E} + n_r \mathbf{F} = r \begin{bmatrix}
\rho_g (n_x u_g + n_r v_g) \\
\rho_g u_g (n_x u_g + n_r v_g) + n_x p \\
\rho_g v_g (n_x u_g + n_r v_g) + n_r p \\
\rho_g H (n_x u_g + n_r v_g) \\
\rho_p (n_x u_p + n_r v_p) \\
\rho_p u_p (n_x u_p + n_r v_p) \\
\rho_p v_p (n_x u_p + n_r v_p) \\
\rho_p \varepsilon_p (n_x u_p + n_r v_p)
\end{bmatrix}. \tag{120}
$$

The normal and tangential components of the velocity is expressed by

$$
\begin{bmatrix} u_n \\ u_t \end{bmatrix} = \begin{bmatrix} n_x & n_r \\ -n_r & n_x \end{bmatrix} \begin{bmatrix} u \\ v \end{bmatrix}, \tag{121}
$$

or reversing it as

$$
\begin{bmatrix} u \\ v \end{bmatrix} = \begin{bmatrix} n_x & -n_r \\ n_r & n_x \end{bmatrix} \begin{bmatrix} u_n \\ u_t \end{bmatrix}. \tag{122}
$$

The convection term can then be written using (u_n, u_t) as,

$$
\widetilde{\mathbf{E}} = n_x \mathbf{E} + n_r \mathbf{F} = r\mathbf{T}\mathbf{G}, \tag{123}
$$

where

$$\mathbf{T} \equiv \begin{bmatrix} 1 & 0 & 0 & 0 & 0 & 0 & 0 & 0 \\ 0 & n_x & -n_r & 0 & 0 & 0 & 0 & 0 \\ 0 & n_r & n_x & 0 & 0 & 0 & 0 & 0 \\ 0 & 0 & 0 & 1 & 0 & 0 & 0 & 0 \\ 0 & 0 & 0 & 0 & 1 & 0 & 0 & 0 \\ 0 & 0 & 0 & 0 & 0 & n_x & -n_r & 0 \\ 0 & 0 & 0 & 0 & 0 & n_r & n_x & 0 \\ 0 & 0 & 0 & 0 & 0 & 0 & 0 & 1 \end{bmatrix}, \text{ and } \mathbf{G} \equiv \begin{bmatrix} \rho_g u_{g_n} \\ \rho_g u_{g_n}^2 + p \\ \rho_g u_{g_t} u_{g_n} \\ \rho_g H u_{g_n} \\ \rho_p u_{p_n} \\ \rho_p u_{p_n}^2 \\ \rho_p u_{p_t} u_{p_n} \\ \rho_p \varepsilon_p u_{p_n} \end{bmatrix}. \tag{124}$$

The equation (119) can be rewritten by using Eq.(123) as,

$$Vol_{i,j} \frac{d\overline{\mathbf{q}}_{i,j}}{dt} + \oint_{\partial A_{ij}} r\mathbf{T}\mathbf{G}\, ds = Vol_{i,j}\, \overline{\mathbf{S}}_{i,j}\ . \tag{125}$$

The integral of the convection term is written for the present cell as

$$\begin{aligned} \oint_{\partial A_{ij}} r\mathbf{T}\mathbf{G}\, ds &= \int_A^B r\mathbf{T}\mathbf{G}\, ds + \int_B^C r\mathbf{T}\mathbf{G}\, ds + \int_C^D r\mathbf{T}\mathbf{G}\, ds + \int_D^A r\mathbf{T}\mathbf{G}\, ds \\ &= T_{AB} \int_A^B r\mathbf{G}\, ds + T_{BC} \int_B^C r\mathbf{G}\, ds + T_{CD} \int_C^D r\mathbf{G}\, ds + T_{DA} \int_D^A r\mathbf{G}\, ds \end{aligned} \tag{126}$$

Furthermore, introducing the following averaged quantities,

$$\overline{\mathbf{G}} \equiv \frac{\int r\mathbf{G}\, ds}{\int r\, ds} \quad \text{and} \quad \bar{r} \equiv \frac{\int r\, ds}{\int ds} = \frac{\int r\, ds}{\Delta s}, \tag{127}$$

Eq. (126) is rewritten as,

$$\begin{aligned} \oint_{\partial A_{ij}} r\mathbf{T}\mathbf{G}\, ds = {} & \Delta s_{AB}\, \bar{r}_{AB}\, \mathbf{T}_{AB}\, \overline{\mathbf{G}}_{AB} + \Delta s_{BC}\, \bar{r}_{BC}\, \mathbf{T}_{BC}\, \overline{\mathbf{G}}_{BC} \\ & + \Delta s_{CD}\, \bar{r}_{CD}\, \mathbf{T}_{CD}\, \overline{\mathbf{G}}_{CD} + \Delta s_{DA}\, \bar{r}_{DA}\, \mathbf{T}_{DA}\, \overline{\mathbf{G}}_{DA} \end{aligned}\ . \tag{128}$$

The system of governing equations (125) can be written using Eq. (128) as,

$$Vol_{i,j} \frac{d\overline{\mathbf{q}}_{i,j}}{dt} + \sum_{k=1}^{4} \Delta s_k\, \bar{r}_k\, \mathbf{T}_k\, \overline{\mathbf{G}}_k = Vol_{i,j}\, \overline{\mathbf{S}}_{i,j}\,, \tag{129}$$

where k = 1,2,3,4 represent line segments AB, BC, CD, and DE, respectively.

It is also convenient, in case of a structured grid, to use the unit normal vectors of the i-direction and the j-direction instead of using the outward unit normal vectors. In this case, Eq. (129) is rewritten as

$$\begin{aligned} Vol_{i,j} \frac{d\overline{\mathbf{q}}_{i,j}}{dt} & + \left(\Delta s\, \bar{r}\, \mathbf{T}\, \overline{\mathbf{G}}\right)_{i+1/2,j} - \left(\Delta s\, \bar{r}\, \mathbf{T}\, \overline{\mathbf{G}}\right)_{i-1/2,j} \\ & + \left(\Delta s\, \bar{r}\, \mathbf{T}\, \overline{\mathbf{G}}\right)_{i,j+1/2} - \left(\Delta s\, \bar{r}\, \mathbf{T}\, \overline{\mathbf{G}}\right)_{i,j-1/2} = Vol_{i,j}\, \overline{\mathbf{S}}_{i,j} \end{aligned}\ , \tag{130}$$

where $\mathbf{T}$, $\overline{\mathbf{G}}$ are with the unit normal vectors of the i- and j- directions of each cell boundary.

After the numerical flux $\overline{\mathbf{G}}$ is determined, the flux vector is retransformed by the matrix $\mathbf{T}$ to give the momentum components in (x, r) directions.

Time-wise numerical integration

An LU-SGS method is used for the time-wise integration. Let us integrate Eq. (129) by time from t^n to t^{n+1}.

$$Vol_{i,j}\int_{t^n}^{t^{n+1}}\frac{d\overline{\mathbf{q}}_{i,j}}{dt}dt+\sum_k \Delta s_k \bar{r}_k \mathbf{T}_k \int_{t^n}^{t^{n+1}}\overline{\mathbf{G}}_k dt = Vol_{i,j}\int_{t^n}^{t^{n+1}}\overline{\mathbf{S}}_{i,j}dt \tag{131}$$

Performing the integration with $\overline{\mathbf{G}}$ and $\overline{\mathbf{S}}$ evaluated at t^{n+1}, one can get

$$\begin{aligned} Vol_{i,j}\left(\overline{\mathbf{q}}_{i,j}^{n+1}-\overline{\mathbf{q}}_{i,j}^{n}\right)+\Delta t\left[\left(\Delta s\bar{r}\mathbf{T}\overline{\mathbf{G}}^{n+1}\right)_{i+1/2,j}-\left(\Delta s\bar{r}\mathbf{T}\overline{\mathbf{G}}^{n+1}\right)_{i-1/2,j}\right] \\ +\Delta t\left[\left(\Delta s\bar{r}\mathbf{T}\overline{\mathbf{G}}^{n+1}\right)_{i,j+1/2}-\left(\Delta s\bar{r}\mathbf{T}\overline{\mathbf{G}}^{n+1}\right)_{i,j-1/2}\right]=\Delta t Vol_{i,j}\,\overline{\mathbf{S}}_{i,j}^{n+1}. \end{aligned} \tag{132}$$

Denoting the difference $\bar{q}^{n+1}-\bar{q}^{n}$ by $\Delta\bar{q}$ and expanding $\overline{\mathbf{G}}$ and $\overline{\mathbf{S}}$ by $\Delta\bar{q}$ around those of $t=t^n$ to the first order, one can get

$$\begin{aligned} \Delta\overline{\mathbf{q}}_{i,j}+\frac{\Delta t}{Vol_{i,j}}\Bigg[&\left\{\Delta s\bar{r}\mathbf{T}\left(\overline{\mathbf{G}}^{n}+\frac{\partial\overline{\mathbf{G}}}{\partial\overline{\mathbf{q}}}^{n}\Delta\overline{\mathbf{q}}\right)\right\}_{i+1/2,j}-\left\{\Delta s\bar{r}\mathbf{T}\left(\overline{\mathbf{G}}^{n}+\frac{\partial\overline{\mathbf{G}}}{\partial\overline{\mathbf{q}}}^{n}\Delta\overline{\mathbf{q}}\right)\right\}_{i-1/2,j} \\ &+\left\{\Delta s\bar{r}\mathbf{T}\left(\overline{\mathbf{G}}^{n}+\frac{\partial\overline{\mathbf{G}}}{\partial\overline{\mathbf{q}}}^{n}\Delta\overline{\mathbf{q}}\right)\right\}_{i,j+1/2}-\left\{\Delta s\bar{r}\mathbf{T}\left(\overline{\mathbf{G}}^{n}+\frac{\partial\overline{\mathbf{G}}}{\partial\overline{\mathbf{q}}}^{n}\Delta\overline{\mathbf{q}}\right)\right\}_{i,j-1/2}\Bigg] \\ &=\Delta t\left(\overline{\mathbf{S}}^{n}+\frac{\partial\overline{\mathbf{S}}}{\partial\overline{\mathbf{q}}}^{n}\Delta\overline{\mathbf{q}}\right)_{i,j} \end{aligned} \tag{133}$$

Denoting the difference $()_{i+1/2,j}-()_{i-1/2,j}$ by $\delta_I()$ and $()_{i,j+1/2}-()_{i,j-1/2}$ by $\delta_J()$, and omitting the superscript n, Eq. (133) can be written with some modification in the left-hand side as

$$\begin{aligned} \left[\mathbf{I}-\Delta t\frac{\partial\overline{\mathbf{S}}}{\partial\overline{\mathbf{q}}}_{i,j}+\frac{\Delta t}{Vol_{i,j}}\left\{\delta_I\left(\Delta s\bar{r}\mathbf{T}\frac{\partial\overline{\mathbf{G}}}{\partial\overline{\mathbf{q}}}\right)+\delta_J\left(\Delta s\bar{r}\mathbf{T}\frac{\partial\overline{\mathbf{G}}}{\partial\overline{\mathbf{q}}}\right)\right\}\right]\Delta\overline{\mathbf{q}}_{i,j} \\ =-\frac{\Delta t}{Vol_{i,j}}\left\{\delta_I\left(\Delta s\bar{r}\mathbf{T}\overline{\mathbf{G}}\right)+\delta_J\left(\Delta s\bar{r}\mathbf{T}\overline{\mathbf{G}}\right)-Vol_{i,j}\overline{\mathbf{S}}_{i,j}\right\} \end{aligned} \tag{134}$$

Furthermore, splitting the source term operator in the left-hand side, we get

$$\left(\mathbf{I}-\Delta t\frac{\partial\overline{\mathbf{S}}}{\partial\overline{\mathbf{q}}}_{i,j}\right)\left[\mathbf{I}+\frac{\Delta t}{Vol_{i,j}}\left\{\delta_I\left(\Delta s\bar{r}\mathbf{T}\frac{\partial\overline{\mathbf{G}}}{\partial\overline{\mathbf{q}}}\right)+\delta_J\left(\Delta s\bar{r}\mathbf{T}\frac{\partial\overline{\mathbf{G}}}{\partial\overline{\mathbf{q}}}\right)\right\}\right]\Delta\overline{\mathbf{q}}_{i,j}=\mathbf{RHS}_{i,j}, \tag{135}$$

where

$$\mathbf{RHS}_{i,j}\equiv-\frac{\Delta t}{Vol_{i,j}}\left\{\delta_I\left(\Delta s\bar{r}\mathbf{T}\overline{\mathbf{G}}\right)^n+\delta_J\left(\Delta s\bar{r}\mathbf{T}\overline{\mathbf{G}}\right)^n-Vol_{i,j}\overline{\mathbf{S}}_{i,j}^{n}\right\}. \tag{136}$$

In LU-SGS method, the convective term implicit operator is split as follows.

$$\left(\mathbf{I}-\Delta t\frac{\partial\overline{\mathbf{S}}}{\partial\overline{\mathbf{q}}}_{i,j}\right)\left[\mathbf{I}+\frac{\Delta t}{Vol_{i,j}}\left\{\nabla_I\left(\Delta s\bar{r}\mathbf{T}\frac{\partial\overline{\mathbf{G}}^{+}}{\partial\overline{\mathbf{q}}}\right)+\Delta_I\left(\Delta s\bar{r}\mathbf{T}\frac{\partial\overline{\mathbf{G}}^{-}}{\partial\overline{\mathbf{q}}}\right)\right.\right.$$
$$\left.\left.+\nabla_J\left(\Delta s\bar{r}\mathbf{T}\frac{\partial\overline{\mathbf{G}}^{+}}{\partial\overline{\mathbf{q}}}\right)+\Delta_J\left(\Delta s\bar{r}\mathbf{T}\frac{\partial\overline{\mathbf{G}}^{-}}{\partial\overline{\mathbf{q}}}\right)\right\}\right]\Delta\overline{\mathbf{q}}_{i,j}=\mathbf{RHS}_{i,j} \tag{137}$$

Here, Δ_I, Δ_J are the forward difference and ∇_I, ∇_J the backward difference of the i- and j-directions, respectively.

Next, let us determine the Jacobian Matrices in Eq. (137). Consider the conservation variable vectors

$$\mathbf{q}^*=\left(\rho_g \quad \rho_g u_g \quad \rho_g v_g \quad \rho_g \varepsilon_g \quad \rho_p \quad \rho_p u_p \quad \rho_p v_p \quad \rho_p \varepsilon_p\right)^T \tag{138}$$

$$\tilde{\mathbf{q}}^*=\left(\rho_g \quad \rho_g u_{g_n} \quad \rho_g u_{g_t} \quad \rho_g \varepsilon_g \quad \rho_p \quad \rho_p u_{p_n} \quad \rho_p u_{p_t} \quad \rho_p \varepsilon_p\right)^T \tag{139}$$

Note that $d\mathbf{q}^*=\mathbf{T}d\tilde{\mathbf{q}}^*$.

The Jacobian matrix is written as

$$\frac{\partial\overline{\mathbf{G}}}{\partial\overline{\mathbf{q}}}=\frac{\partial\mathbf{G}}{\partial\mathbf{q}^*}=\frac{\partial\mathbf{G}}{\partial\tilde{\mathbf{q}}^*}\frac{\partial\tilde{\mathbf{q}}^*}{\partial\mathbf{q}^*}=\hat{\mathbf{A}}\frac{\partial\tilde{\mathbf{q}}^*}{\partial\mathbf{q}^*}=\hat{\mathbf{A}}\mathbf{T}^{-1}. \tag{140}$$

The Jacobian matrix $\hat{\mathbf{A}}\equiv\partial\mathbf{G}/\partial\tilde{\mathbf{q}}^*$ can be obtained as

$$\hat{\mathbf{A}}=\begin{pmatrix}
0 & 1 & 0 & 0 & 0 & 0 & 0 & 0\\
\frac{\Gamma}{2}(u_{g_n}^2+u_{g_t}^2)-u_{g_n}^2 & (3-\gamma)u_{g_n} & -\Gamma u_{g_t} & \Gamma & 0 & 0 & 0 & 0\\
-u_{g_n}u_{g_t} & u_{g_t} & u_{g_n} & 0 & 0 & 0 & 0 & 0\\
\frac{1}{2}u_{g_n}\left\{-2H+\Gamma(u_{g_n}^2+u_{g_t}^2)\right\} & H-\Gamma u_{g_n}^2 & -\Gamma u_{g_n}u_{g_t} & \gamma u_{g_n} & 0 & 0 & 0 & 0\\
0 & 0 & 0 & 0 & 0 & 1 & 0 & 0\\
0 & 0 & 0 & 0 & -u_{p_n}^2 & 2u_{p_n} & 0 & 0\\
0 & 0 & 0 & 0 & -u_{p_n}u_{p_t} & u_{p_t} & u_{p_n} & 0\\
0 & 0 & 0 & 0 & -u_{p_n}e_p & e_p & 0 & u_{p_n}
\end{pmatrix}, \tag{141}$$

where $\Gamma\equiv\gamma-1$.

From Eqs. (123) and (140), the Jacobian matrix $\tilde{\mathbf{A}}$ is defined as

$$\tilde{\mathbf{A}}\equiv\frac{\partial\tilde{\mathbf{E}}}{\partial\mathbf{q}^*}\equiv\frac{\partial\left(n_x\mathbf{E}+n_r\mathbf{F}\right)}{\partial\mathbf{q}^*}=r\,\mathbf{T}\frac{\partial\mathbf{G}}{\partial\mathbf{q}^*}=r\,\mathbf{T}\hat{\mathbf{A}}\mathbf{T}^{-1}. \tag{142}$$

The equation (137) can then be written as

$$\left(\mathbf{I}-\Delta t\frac{\partial\overline{\mathbf{S}}}{\partial\overline{\mathbf{q}}}_{i,j}\right)\left[\mathbf{I}+\frac{\Delta t}{Vol_{i,j}}\left\{\nabla_I\left(\Delta s\mathbf{A}^{+}\right)+\Delta_I\left(\Delta s\mathbf{A}^{-}\right)+\nabla_J\left(\Delta s\mathbf{B}^{+}\right)+\Delta_J\left(\Delta s\mathbf{B}^{-}\right)\right\}\right]\Delta\overline{\mathbf{q}}_{i,j}=\mathbf{RHS}_{i,j}, \tag{143}$$

where $\tilde{\mathbf{A}}$ in the i-direction is replaced by $\mathbf{A}$ and in the j-direction by $\mathbf{B}$.

In the LU-SGS method, the diagonal dominant, split matrices according to the information propagating directions are defined as

$$\mathbf{A}^{\pm} \equiv \frac{1}{2}(\mathbf{A} \pm \nu_A \mathbf{I}), \tag{144}$$

$$\mathbf{B}^{\pm} \equiv \frac{1}{2}(\mathbf{B} \pm \nu_B \mathbf{I}), \tag{145}$$

where ν_A and ν_B are the spectral radii of **A** and **B**, respectively, and calculated by

$$\nu \equiv r \times \max\left[\left|u_{g_n}\right| + a, \left|u_{p_n}\right|\right]. \tag{146}$$

The equation (143) is rewritten with Eqs.(144) and (145) as

$$\left(\mathbf{I} - \Delta t \frac{\partial \overline{\mathbf{S}}}{\partial \overline{\mathbf{q}}}_{i,j}\right) \times \left[\left(1 + \frac{\Delta t}{Vol_{i,j}}\left\{(\Delta s_I \nu_A)_{i,j} + (\Delta s_J \nu_B)_{i,j}\right\}\right)\mathbf{I} + \right.$$
$$\left. + \frac{\Delta t}{Vol_{i,j}}\left\{-(\Delta s_I \mathbf{A}^+)_{i-1,j} - (\Delta s_J \mathbf{B}^+)_{i,j-1}\right\} + \frac{\Delta t}{Vol_{i,j}}\left\{+(\Delta s_I \mathbf{A}^-)_{i+1,j} + (\Delta s_J \mathbf{B}^-)_{i,j+1}\right\}\right] \Delta \overline{\mathbf{q}}_{i,j} = \mathbf{RHS}_{i,j} \tag{147}$$

At last the LU-SGS scheme is obtained as

$$\left(\mathbf{I} - \Delta t \frac{\partial \overline{\mathbf{S}}}{\partial \overline{\mathbf{q}}}_{i,j}\right)\left[\mathbf{I} + \frac{\Delta t}{Vol_{i,j}\alpha_{i,j}}\left\{-(\Delta s_I \mathbf{A}^+)_{i-1,j} - (\Delta s_J \mathbf{B}^+)_{i,j-1}\right\}\right]$$
$$\times \left[\mathbf{I} + \frac{\Delta t}{Vol_{i,j}\alpha_{i,j}}\left\{+(\Delta s_I \mathbf{A}^-)_{i+1,j} + (\Delta s_J \mathbf{B}^-)_{i,j+1}\right\}\right] \Delta \overline{\mathbf{q}}_{i,j} = \frac{1}{\alpha_{i,j}} \mathbf{RHS}_{i,j}, \tag{148}$$

where

$$\alpha_{i,j} \equiv 1 + \frac{\Delta t}{Vol_{i,j}}\left\{(\Delta s_I \nu_A)_{i,j} + (\Delta s_J \nu_B)_{i,j}\right\}. \tag{149}$$

Integration of the above draws the following three steps as an LU-SGS method.

First Step: Point implicit scheme

$$\left(\mathbf{I} - \Delta t \frac{\partial \overline{\mathbf{S}}}{\partial \overline{\mathbf{q}}}_{i,j}\right) \Delta \mathbf{q}^{**}_{i,j} = \frac{1}{\alpha_{i,j}} \mathbf{RHS}_{i,j}, \tag{150}$$

where

$$\frac{\partial \mathbf{S}}{\partial \mathbf{q}} = \frac{\partial \mathbf{S}}{\partial \mathbf{q}}^{(AXISYM)} + \frac{\partial \mathbf{S}}{\partial \mathbf{q}}^{(2PHASE)} \tag{151}$$

$$\frac{\partial \mathbf{S}}{\partial \mathbf{q}}^{(AXISYM)} = \begin{pmatrix} 0 & 0 & 0 & 0 & 0 & 0 & 0 & 0 \\ 0 & 0 & 0 & 0 & 0 & 0 & 0 & 0 \\ \dfrac{(\gamma-1)(u_g^2+v_g^2)}{2r} & \dfrac{(1-\gamma)u_g}{r} & \dfrac{(1-\gamma)v_g}{r} & \dfrac{\gamma-1}{r} & 0 & 0 & 0 & 0 \\ 0 & 0 & 0 & 0 & 0 & 0 & 0 & 0 \\ 0 & 0 & 0 & 0 & 0 & 0 & 0 & 0 \\ 0 & 0 & 0 & 0 & 0 & 0 & 0 & 0 \\ 0 & 0 & 0 & 0 & 0 & 0 & 0 & 0 \\ 0 & 0 & 0 & 0 & 0 & 0 & 0 & 0 \end{pmatrix} \tag{152}$$

$$
\frac{\partial \mathbf{S}^{(2PHASE)}}{\partial \mathbf{q}} =
\begin{pmatrix}
0 & 0 & 0 & 0 & 0 & 0 & 0 & 0 \\
0 & 0 & 0 & 0 & 0 & 0 & 0 & 0 \\
0 & 0 & 0 & 0 & 0 & \frac{1}{\tau_v} & 0 & 0 \\
0 & 0 & 0 & 0 & 0 & 0 & \frac{1}{\tau_v} & 0 \\
0 & 0 & 0 & 0 & 0 & -\frac{u_p - u_g}{\tau_v} & -\frac{v_p - v_g}{\tau_v} - 2\nu_p & \frac{1}{\tau_T} \\
0 & 0 & 0 & 0 & 0 & 0 & 0 & 0 \\
0 & 0 & 0 & 0 & 0 & 0 & 0 & 0 \\
0 & 0 & 0 & 0 & 0 & \frac{u_p - u_g}{\tau_v} & \frac{v_p - v_g}{\tau_v} + 2\nu_p & -\frac{1}{\tau_T}
\end{pmatrix}
$$

$$
=
\begin{pmatrix}
0 & 0 & 0 & 0 & 0 & 0 & 0 & 0 \\
0 & 0 & 0 & 0 & 0 & 0 & 0 & 0 \\
0 & 0 & 0 & 0 & 0 & \frac{1}{\tau_v} & 0 & 0 \\
0 & 0 & 0 & 0 & 0 & 0 & \frac{1}{\tau_v} & 0 \\
0 & 0 & 0 & 0 & -\frac{\kappa}{\tau_T} & -\frac{u_p - u_g}{\tau_v} & -\frac{v_p - v_g}{\tau_v} - 2\nu_p & \frac{1}{\tau_T} \\
0 & 0 & 0 & 0 & 0 & 0 & 0 & 0 \\
0 & 0 & 0 & 0 & 0 & 0 & 0 & 0 \\
0 & 0 & 0 & 0 & \frac{\kappa}{\tau_T} & \frac{u_p - u_g}{\tau_v} & \frac{v_p - v_g}{\tau_v} + 2\nu_p & -\frac{1}{\tau_T}
\end{pmatrix}
$$

$$
+
\begin{pmatrix}
0 & 0 & 0 & 0 & 0 & 0 & 0 & 0 \\
0 & 0 & 0 & 0 & 0 & 0 & 0 & 0 \\
0 & 0 & 0 & -\frac{\psi}{\tau_v} & 0 & 0 & 0 & 0 \\
0 & 0 & -\frac{\psi}{\tau_v} & 0 & 0 & 0 & 0 & 0 \\
0 & 0 & 0 & 0 & -\psi\left(\frac{1}{\tau_v} - \frac{\nu_p}{\tau_T}\right) & -\psi\frac{u_p}{\tau_T} & -\psi\left(\frac{\nu_p}{\tau_v} + \frac{\kappa_g \nu_g}{\tau_T}\right) & \psi\frac{1}{\tau_T} \\
0 & 0 & 0 & 0 & 0 & 0 & 0 & 0 \\
0 & 0 & 0 & 0 & 0 & 0 & 0 & 0 \\
0 & 0 & -\frac{\psi}{\tau_v} & 0 & \psi\left(\frac{\nu_p}{\tau_v} + \frac{\kappa_g \nu_g}{\tau_T}\right) & \psi\left(\frac{u_p}{\tau_T} + \frac{\kappa_g u_g}{\tau_T}\right) & \psi\left(\frac{1}{\tau_v} + \frac{\kappa_g \nu_g}{\tau_T}\right) & -\psi\frac{1}{\tau_T}
\end{pmatrix}
$$

$$
-\psi
\begin{pmatrix}
0 & 0 & 0 & 0 & 0 & 0 & 0 & 0 \\
0 & 0 & 0 & 0 & 0 & 0 & 0 & 0 \\
0 & 0 & \frac{u_g}{\tau_v} & -\frac{\nu_g}{\tau_v} & 0 & 0 & 0 & 0 \\
0 & 0 & -\frac{\nu_g}{\tau_v} & -\frac{u_g}{\tau_v} & 0 & 0 & 0 & 0 \\
0 & 0 & 0 & 0 & \frac{\kappa_g}{2\tau_T}\left\{\frac{u_g^2 + \nu_g^2}{\tau_v} + \frac{2c_v T_g}{\tau_T} - u_g^2 - \nu_g^2\right\} & \frac{\kappa_g u_g}{\tau_T} & \frac{\kappa_g \nu_g}{\tau_T} & -\frac{\kappa_g}{\tau_T} \\
0 & 0 & 0 & 0 & 0 & 0 & 0 & 0 \\
0 & 0 & 0 & 0 & 0 & 0 & 0 & 0 \\
0 & 0 & \frac{u_g}{\tau_v} & \frac{\nu_g}{\tau_v} & \frac{\kappa_g}{2\tau_T}\left\{\frac{u_g^2 + \nu_g^2}{\tau_v} + \frac{2c_v T_g}{\tau_T} - u_g^2 - \nu_g^2\right\} & \frac{\kappa_g u_g}{\tau_T} & \frac{\kappa_g \nu_g}{\tau_T} & -\frac{\kappa_g}{\tau_T}
\end{pmatrix}
\tag{153}
$$

Here the loading ratio is defined by

$$\psi \equiv \frac{\rho_p}{\rho_g}, \tag{154}$$

and the ratio of specific heats is

$$\kappa \equiv \frac{C_{Pp}}{c_v}. \tag{155}$$

The non-zero eigenvalues of the Jacobian matrix of the two-phase source term are

$$-\frac{1+\psi}{\tau_V} \quad \text{and} \quad -\frac{1+\kappa\psi}{\tau_T}. \tag{156}$$

Then the spectral radius is determined by

$$\nu_S = \max\left[\frac{1+\psi}{\tau_V}, \quad \frac{1+\kappa\psi}{\tau_T}\right]. \tag{157}$$

When an explicit scheme is employed the time step must be smaller than $1/\nu_S$. It turns out that τ_V and τ_T are functions of the square of the particle diameter as shown in Eqs. (109) and (110). The restriction to the time step, therefore, becomes very severe as a particle becomes small. Since it may become restrictive comparably to or more than the convection term, it is required to use an implicit solution about the source term.

The first step is further decomposed into two operators as follows.

$$\left(\mathbf{I}-\Delta t\frac{\partial\overline{\mathbf{S}}}{\partial\overline{\mathbf{q}}}\right)\Delta\mathbf{q}^{**}_{i,j} = \left(\mathbf{I}-\Delta t\frac{\partial\overline{\mathbf{S}}}{\partial\overline{\mathbf{q}}}^{AXISYM}\right)\times\left(\mathbf{I}-\Delta t\frac{\partial\overline{\mathbf{S}}}{\partial\overline{\mathbf{q}}}^{2PHASE}\right)\Delta\mathbf{q}^{**}_{i,j} = \frac{1}{\alpha_{i,j}}\mathbf{RHS}_{i,j} \tag{158}$$

Then, in STEP (1-1), we first solve axisymmetric-source-term implicit part,

$$\left(\mathbf{I}-\Delta t\frac{\partial\overline{\mathbf{S}}}{\partial\overline{\mathbf{q}}}^{AXISYM}\right)\Delta\mathbf{q}^{***}_{i,j} = \frac{1}{\alpha_{i,j}}\mathbf{RHS}_{i,j}. \tag{159}$$

This solution can be explicitly shown as

$$\Delta\mathbf{q}^{***}_{i,j} = \frac{1}{\alpha_{i,j}}\begin{bmatrix} RHS^{(1)} \\ RHS^{(2)} \\ \beta\left\{\frac{\Gamma}{2}\left(u_g^2+v_g^2\right)RHS^{(1)} + \Gamma u_g RHS^{(2)} + \frac{r}{\Delta t}RHS^{(3)} + \Gamma RHS^{(4)}\right\} \\ RHS^{(4)} \\ RHS^{(5)} \\ RHS^{(6)} \\ RHS^{(7)} \\ RHS^{(8)} \end{bmatrix}_{i,j}, \tag{160}$$

where

$$\beta \equiv \frac{1}{\frac{r}{\Delta t}+\Gamma v_g}, \quad \text{and} \quad \Gamma \equiv \gamma - 1. \tag{161}$$

Next, in STEP (1-2), we solve the two-phase source-term implicit part,

$$\left(\mathbf{I}-\Delta t\frac{\partial\overline{\mathbf{S}}}{\partial\overline{\mathbf{q}}}^{2PHASE}\right)\Delta\mathbf{q}_{i,j}^{**}=\Delta\mathbf{q}_{i,j}^{***}. \tag{162}$$

All but the two, $\Delta\boldsymbol{q}_{i,j}^{**(4)}$ and $\Delta\boldsymbol{q}_{i,j}^{**(8)}$, are determined as the followings.

$$\Delta q_{i,j}^{**(1)}=\Delta q_{i,j}^{***(1)} \tag{163}$$

$$\Delta q_{i,j}^{**(2)}=\frac{1}{1+\psi+\dfrac{\tau_V}{\Delta t}}\left\{\psi u_g\Delta q_{i,j}^{***(1)}+\left(1+\frac{\tau_V}{\Delta t}\right)\Delta q_{i,j}^{***(2)}-u_g\Delta q_{i,j}^{***(5)}+\Delta q_{i,j}^{***(6)}\right\} \tag{164}$$

$$\Delta q_{i,j}^{**(3)}=\frac{1}{1+\psi+\dfrac{\tau_V}{\Delta t}}\left\{\psi v_g\Delta q_{i,j}^{***(1)}+\left(1+\frac{\tau_V}{\Delta t}\right)\Delta q_{i,j}^{***(3)}-v_g\Delta q_{i,j}^{***(5)}+\Delta q_{i,j}^{***(7)}\right\} \tag{165}$$

$$\Delta q_{i,j}^{**(5)}=\Delta q_{i,j}^{***(5)} \tag{166}$$

$$\Delta q_{i,j}^{**(6)}=\frac{1}{1+\psi+\dfrac{\tau_V}{\Delta t}}\left\{-\psi u_g\Delta q_{i,j}^{***(1)}+\psi\Delta q_{i,j}^{***(2)}+u_g\Delta q_{i,j}^{***(5)}+\left(\psi+\frac{\tau_V}{\Delta t}\right)\Delta q_{i,j}^{***(6)}\right\} \tag{167}$$

$$\Delta q_{i,j}^{**(7)}=\frac{1}{1+\psi+\dfrac{\tau_V}{\Delta t}}\left\{-\psi v_g\Delta q_{i,j}^{***(1)}+\psi\Delta q_{i,j}^{***(3)}+v_g\Delta q_{i,j}^{***(5)}+\left(\psi+\frac{\tau_V}{\Delta t}\right)\Delta q_{i,j}^{***(7)}\right\} \tag{168}$$

Then, $\Delta\boldsymbol{q}_{i,j}^{**(4)}$ and $\Delta\boldsymbol{q}_{i,j}^{**(8)}$ are determined as

$$\Delta q_{i,j}^{**(4)}=\frac{1}{1+\kappa\psi+\dfrac{\tau_T}{\Delta t}}\left\{\left(1+\frac{\tau_T}{\Delta t}\right)a_4+a_8\right\}, \tag{169}$$

$$\Delta q_{i,j}^{**(8)}=\frac{1}{1+\kappa\psi+\dfrac{\tau_T}{\Delta t}}\left\{\kappa\psi a_4+\left(\kappa\psi+\frac{\tau_T}{\Delta t}\right)a_8\right\}, \tag{170}$$

where

$$a_4=\Delta q_{i,j}^{***(4)}+a_4^*, \tag{171}$$

$$a_8=\Delta q_{i,j}^{***(8)}+a_8^*, \tag{172}$$

$$\begin{aligned}a_4^*=&\psi\left[\frac{\left\{c_vT_g-\frac{1}{2}\left(u_g{}^2+v_g{}^2\right)\right\}\kappa}{\tau_T/\Delta t}+\frac{u_gu_p+v_gv_p}{\tau_V/\Delta t}\right]\Delta q_{i,j}^{**(1)}\\&+\psi\left(\frac{u_g\kappa}{\tau_T/\Delta t}-\frac{u_p}{\tau_V/\Delta t}\right)\Delta q_{i,j}^{**(2)}+\psi\left(\frac{v_g\kappa}{\tau_T/\Delta t}-\frac{v_p}{\tau_V/\Delta t}\right)\Delta q_{i,j}^{**(3)}\\&-\left[\frac{\kappa c_vT_g-\frac{1}{2}\left(u_p^2+v_p^2\right)}{\tau_T/\Delta t}+\frac{u_p^2+v_p^2}{\tau_V/\Delta t}\right]\Delta q_{i,j}^{**(5)}\\&-\left(\frac{u_p}{\tau_T/\Delta t}+\frac{u_g-2u_p}{\tau_V/\Delta t}\right)\Delta q_{i,j}^{**(6)}-\left(\frac{v_p}{\tau_T/\Delta t}+\frac{v_g-2v_p}{\tau_V/\Delta t}\right)\Delta q_{i,j}^{**(7)}\end{aligned}, \tag{173}$$

$$a_8^*=-a_4^*. \tag{174}$$

Second Step: Forward Sweep

$$\Delta\mathbf{q}^{*}_{i,j} = \Delta\mathbf{q}^{**}_{i,j} + \frac{\Delta t}{Vol_{i,j}\alpha_{i,j}}\left\{\left(\Delta s_I \mathbf{A}^{+}\right)_{i-1,j}\Delta\mathbf{q}^{*}_{i-1,j} + \left(\Delta s_J \mathbf{B}^{+}\right)_{i,j-1}\Delta\mathbf{q}^{*}_{i,j-1}\right\} \tag{175}$$

Third Step: Backward Sweep

$$\Delta\overline{\mathbf{q}}_{i,j} = \Delta\mathbf{q}^{*}_{i,j} - \frac{\Delta t}{Vol_{i,j}\alpha_{i,j}}\left\{\left(\Delta s_I \mathbf{A}^{-}\right)_{i+1,j}\Delta\overline{\mathbf{q}}_{i+1,j} + \left(\Delta s_J \mathbf{B}^{-}\right)_{i,j+1}\Delta\overline{\mathbf{q}}_{i,j+1}\right\} \tag{176}$$

Examples of simulation: Here, examples of numerical analyses, carried out by the above-mentioned method, are described concerning some axisymmetric two-phase flows inside a solid rocket motor with simple chamber-nozzle geometry shown in Fig. 52. As shown in the figure, AB is the line of center, BC the outflow boundary, CD the nozzle internal surface, and DA the burning propellant surface.

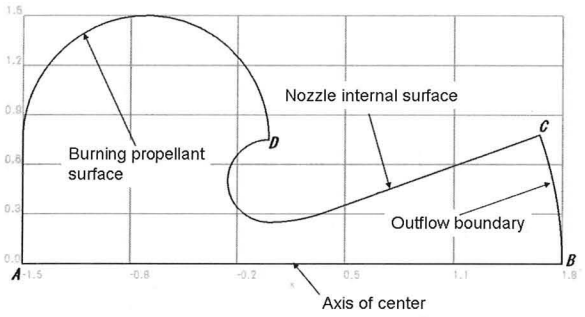

Fig. 52 Geometry of SRM

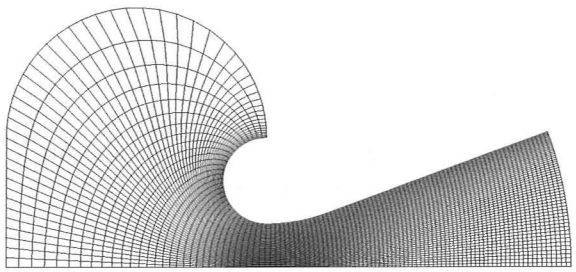

Fig. 53 Grid system

Four cases of different particle diameters, 0.5, 5, 50, and 500 μm, are computed for the combustion temperature T_c of 3500K, combustion pressure p_c of 5MPa, specific heat ratio of gas γ of 1.211, mean molecular weight $\tilde{M}$ of 20.33 g/mol, and the loading ratio ψ of 0.4.

In order to accelerate the convergence, a local time-step method is employed. The grid system employed is shown in Fig. 53 and consists of 101×54 points in *i* and *j* directions.

In Fig. 54～Fig. 61, density distributions of the gaseous phase and the particle phase are plotted. From these results, it is seen that a particle-free zone grows as the diameter of a particle becomes large and the density of gaseous phase is affected by it.

In Fig. 62～Fig. 69, temperature distribution of the both phases are shown. For small particle case, almost phase-equilibrium flow is established. The non-equilibrium nature grows as the particle become large. The temperature of the particle-phase in the particle-free zone is not physical solution, but it is numerically generated virtual solution for a very small amount of numerical particle bulk density values in the particle-free zone obtained by this Eulerian-Eulerian simulation. These are the results of a numerical treatment to cope with the degenerative system of the particle phase equations.

In Fig. 70～Fig. 73, convergence history of each simulation is shown. It is apparent that the steady-state solution is effectively reached in all particle-diameter cases. In case of the largest particle size, 500 μm, numerical stability is less than the other cases and this is thought due to the large particle-free zone appearing in the nozzle.

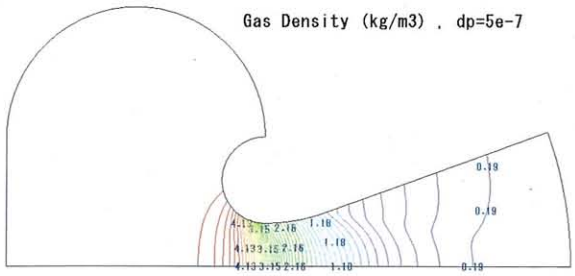

Fig. 54 Gas density, D_p = 0.5 μm

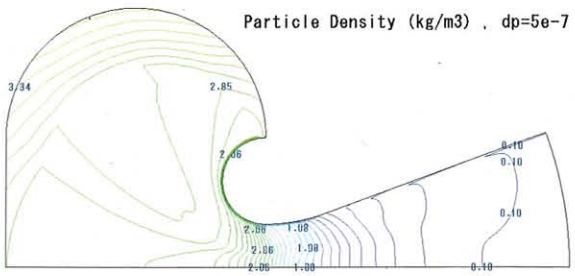

Fig. 55 Particle density, D_p = 0.5 μm

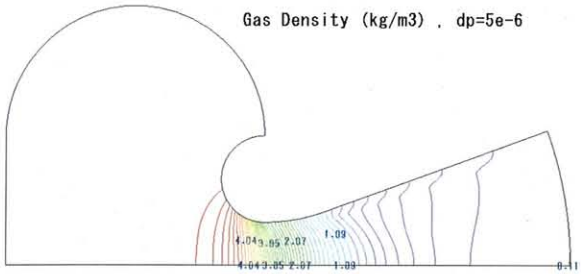

Fig. 56 Gas density, D_p = 5 μm

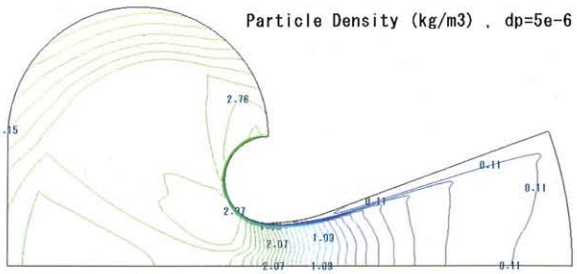

Fig. 57 Particle density, D_p = 5 μm

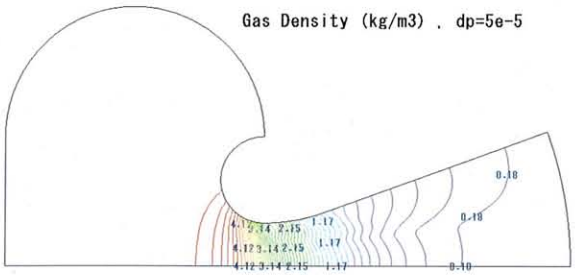

Fig. 58 Gas density, D_p = 50 μm

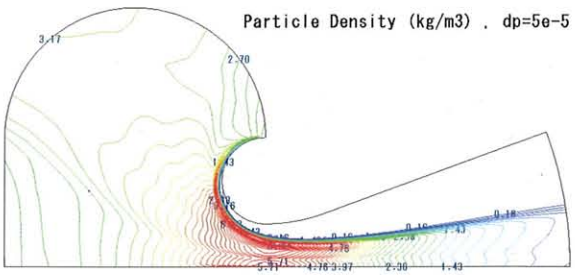

Fig. 59 Particle density, D_p = 50 μm

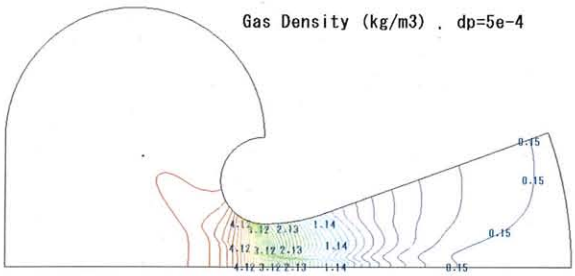

Fig. 60 Gas density, D_p = 500 μm

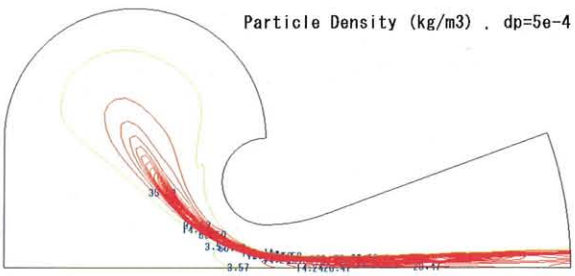

Fig. 61 Particle density, D_p = 500 μm

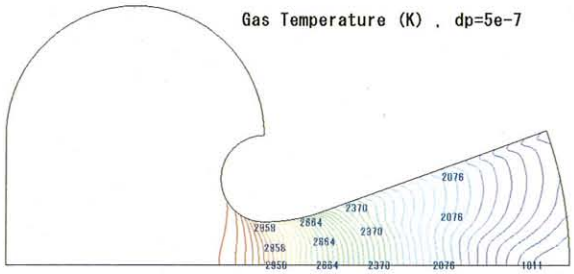

Fig. 62 Gas temperature, D_p = 0.5 μm

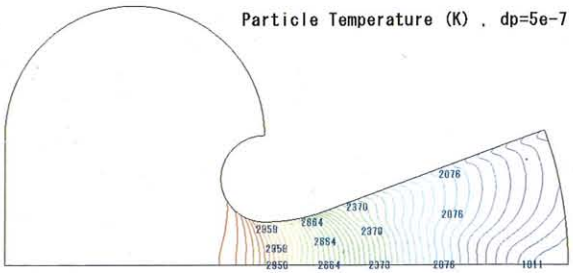

Fig. 63 Particle temperature, D_p = 0.5 μm

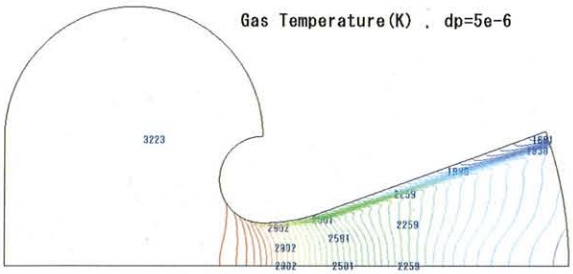

Fig. 64 Gas temperature, D_p = 5 μm

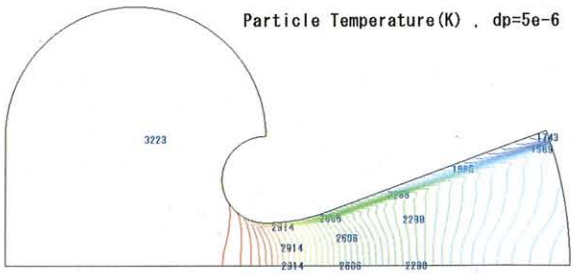

Fig. 65 Particle temperature, D_p = 5 μm

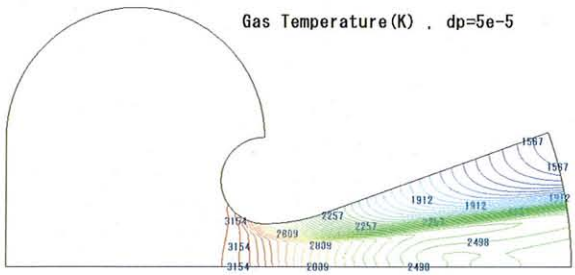

Fig. 66 Gas temperature, D_p = 50 μm

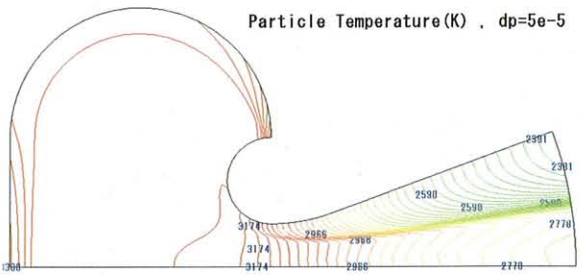

Fig. 67 Particle temperature, D_p = 50 μm

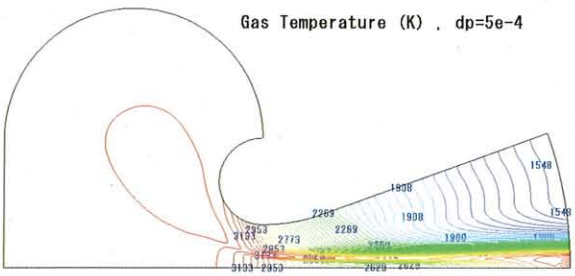

Fig. 68 Gas temperature, D_p = 500 μm

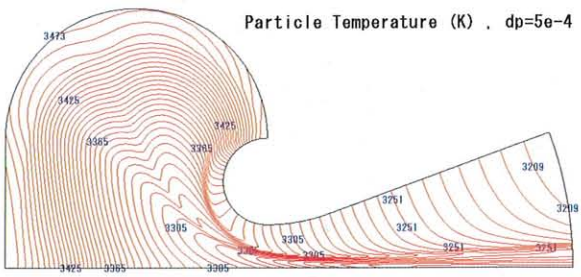

Fig. 69 Particle temperature, D_p = 500 μm

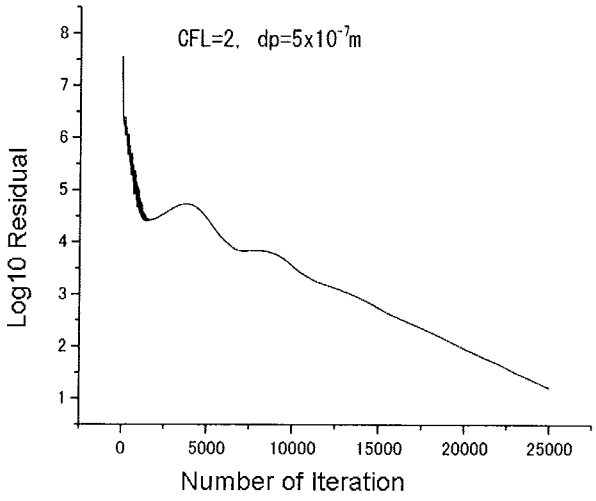

Fig. 70 Convergence history, D_p= 0.5 μm

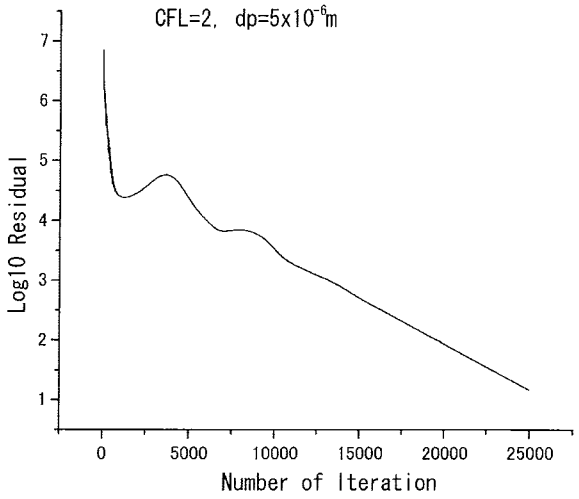

Fig. 71 Convergence history, D_p= 5 μm

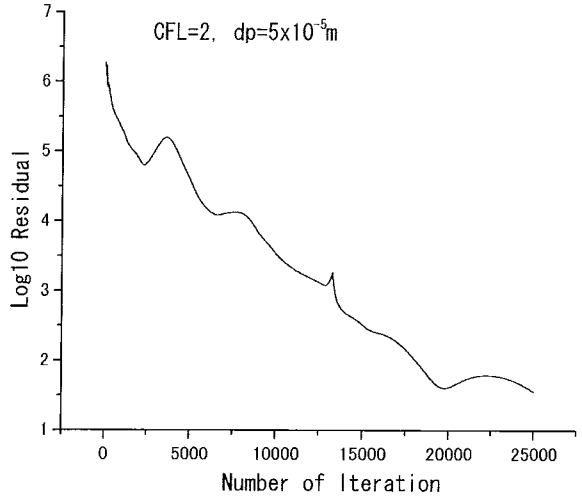

Fig. 72 Convergence history, D_p= 50 μm

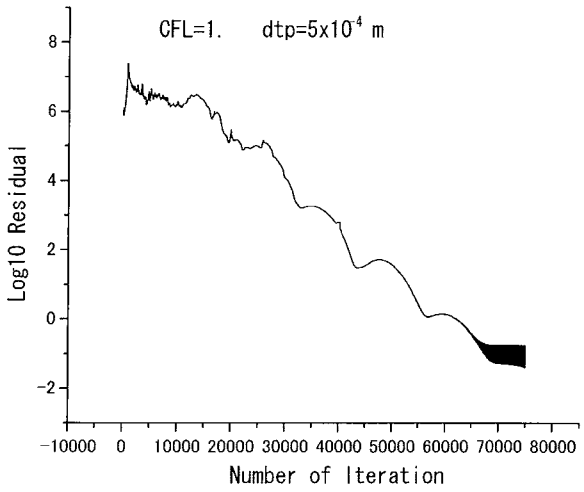

Fig. 73 Convergence history, D_p= 500 μm

3.2. Eulerian-Lagrangian method

A computer program is developed for the Eulerian-Lagrangian method to calculate multiphase flow in SRM. The program is named SPEC-2 (Solid Propulsion Enhanced Code, No.2).

In an Eulerian-Lagrangian method, the gaseous phase is treated as a continuum and described in the Eulerian framework, whereas the particle phase is treated as a group of particles whose motions are described by a dynamics law, i.e., the Lagrangian approach. Since movement of a particle is pursued, it is also called the trajectory method.

In the Lagrangian method, the particle phase is divided into many small particle groups, and behavior of each particle group is investigated. First, let us assume the followings.

1) The domain ΔS which a particle group occupies is small enough that the behavior of the group is represented by a representative particle which exists at the center. That is, the speed and the temperature of all the particles belonging to a particle group are equal to those of the representative particle.
2) The exchanged momentum and energy between the gaseous phase and the particle phase are equal to the product

of the number of the particles contained in a particle group and the amounts of these quantities per a representative particle.

On the other hand, it is required to contain sufficient numbers of particle groups in a cell in order for the averages of physical properties in a cell are to be defined. When the size of the cell in a calculation domain is S_{cell}, including the above-mentioned assumptions, this condition can be written as

$$\ell^3 << \Delta S << S_{cell} << L^3, \tag{177}$$

where ℓ is the mean particle distance and L is a characteristic length of flow.

3.2.1. Governing equations

Particle-phase equations

$$\frac{d\mathbf{W}}{dt} = \mathbf{S} \tag{178}$$

$$\mathbf{W} = \begin{pmatrix} x_p \\ y_p \\ z_p \\ u_p \\ v_p \\ w_p \\ C_{Pp}T_p \end{pmatrix} \qquad \mathbf{S} = \begin{pmatrix} u_p \\ v_p \\ w_p \\ A'(u_g - u_p) \\ A'(v_g - v_p) \\ A'(w_g - w_p) \\ B'(T_g - T_p) \end{pmatrix}, \tag{179}$$

where

$$A' = \frac{3}{8}\frac{\rho_g}{\sigma_m}\left|\vec{U}_s\right| C_D \frac{1}{r_p}, \text{ and } \quad B' = \frac{3}{2\sigma_m r_p^2}\frac{Nu\, c_p\, \mu}{\mathrm{Pr}}. \tag{180}$$

Gaseous-phase equations

Equations for the gaseous phase are basically the same as those in the Eulerian-Eulerian method.

$$\frac{\partial \mathbf{Q}_g}{\partial t} + \frac{\partial \mathbf{E}_g}{\partial x} + \frac{\partial \mathbf{F}_g}{\partial y} + \frac{\partial \mathbf{G}_g}{\partial z} = \mathbf{S}_g \tag{181}$$

$$\mathbf{Q}_g = \begin{pmatrix} \rho_g \\ \rho_g u_g \\ \rho_g v_g \\ \rho_g w_g \\ e_g \end{pmatrix} \quad \mathbf{E}_g = \begin{pmatrix} \rho_g u_g \\ \rho_g u_g^2 + p \\ \rho_g u_g v_g \\ \rho_g u_g w_g \\ (e_g + p)u_g \end{pmatrix} \quad \mathbf{F}_g = \begin{pmatrix} \rho_g v_g \\ \rho_g u_g v_g \\ \rho_g v_g^2 + p \\ \rho_g v_g w_g \\ (e_g + p)v_g \end{pmatrix} \quad \mathbf{G}_g = \begin{pmatrix} \rho_g w_g \\ \rho_g u_g w_g \\ \rho_g v_g w_g \\ \rho_g w_g^2 + p \\ (e_g + p)w_g \end{pmatrix} \tag{182}$$

The treatment of the source term for the gas-particle interactions is described below. In a Lagrangian method representative particles exist in space discretely. An inspection volume Ω of the volume V is considered, and the total number of representative particles in this volume is denoted by N_p. The repulsive force which the gaseous phase in the volume receives from a particle can be written as

$$\vec{F} = -\sum_{k=1}^{N_p} \vec{f}_k N_{Tk} \ . \tag{183}$$

Here N_{Tk} is the number of particles included in the k-th particle group and can be written as

$$N_{Tk} = \frac{M_k}{m_p} . \tag{184}$$

The total mass of the particles in the k-th particle group is denoted by M_k and this value is set initially at a starting point of the trajectory on a burning surface according to the mass generation due to combustion. Finally, the source terms are added to the equation of motion as

$$\begin{aligned}
&\frac{\partial \rho_g u_g}{\partial t} + \frac{\partial(\rho_g u_g^2 + p)}{\partial x} + \frac{\partial(\rho_g u_g v_g)}{\partial y} + \frac{\partial(\rho_g u_g w_g)}{\partial z} = -\sum_{k=1}^{N_p} \frac{M_k}{m_p} \frac{f_x^k}{V} \\
&\frac{\partial \rho_g v_g}{\partial t} + \frac{\partial(\rho_g u_g v_g)}{\partial x} + \frac{\partial(\rho_g v_g^2 + p)}{\partial y} + \frac{\partial(\rho_g v_g w_g)}{\partial z} = -\sum_{k=1}^{N_p} \frac{M_k}{m_p} \frac{f_y^k}{V} \\
&\frac{\partial \rho_g w_g}{\partial t} + \frac{\partial(\rho_g u_g w_g)}{\partial x} + \frac{\partial(\rho_g v_g w_g)}{\partial y} + \frac{\partial(\rho_g w_g^2 + p)}{\partial z} = -\sum_{k=1}^{N_p} \frac{M_k}{m_p} \frac{f_z^k}{V}
\end{aligned} , \tag{185}$$

where $\vec{f}_k = (f_x^k, f_y^k, f_z^k)$. The reason why the right-hand side is divided by the volume V is to obtain space-averaged quantities (per unit volume). In the numerical simulation, the volume of a cell is used for V.

The energy equation is treated similarly. Since the energy which a single particle exchanges with the gaseous phase is the sum of the heat transfer between the phases and the work done by the particle motion, the energy equation can be written as

$$\frac{\partial e_g}{\partial t} + \frac{\partial(e_g + p)u_g}{\partial x} + \frac{\partial(e_g + p)v_g}{\partial y} + \frac{\partial(e_g + p)w_g}{\partial z} = -\sum_{k=1}^{N_p} \frac{M_k}{m_p V} \left(q + f_x^k u_p^k + f_y^k v_p^k + f_z^k w_p^k \right). \tag{186}$$

Finally the phase-interaction source term can be written as

$$S_g = \begin{pmatrix} 0 \\ -\sum_{k=1}^{N_p} \frac{M_k}{V} A'(u_g - u_p^k) \\ -\sum_{k=1}^{N_p} \frac{M_k}{V} A'(v_g - v_p^k) \\ -\sum_{k=1}^{N_p} \frac{M_k}{V} A'(w_g - w_p^k) \\ -\sum_{k=1}^{N_p} \frac{M_k}{V} \left[A' \left(u_p^k (u_g - u_p^k) + v_p^k (v_g - v_p^k) + w_p^k (w_g - w_p^k) \right) + B'(T_g - T_p^k) \right] \end{pmatrix}, \tag{187}$$

where superscript k denotes the velocity or the temperature of the k-th particle group. When the diameter of every particle group differs one another, so do the values of A' and B'.

Particle bulk density

Particle bulk density can be obtained by counting the total mass of particle groups contained in the inspection volume Ω and dividing it by the volume of Ω as

$$\rho_p = \sum_{k=1}^{N_p} \frac{M_k}{V} \tag{188}$$

In a simulation, a finite-volume cell is used for the inspection volume. The particle bulk density for every cell is obtained by dividing the total mass by the volume of the cell.

3.2.2. Outline of numerical simulation method

In the Lagrangian method, the basic equation for the particle-phase shown in Eq. (178) is solved numerically to obtain the temporally changing location and the temperature of a representative particle which has departed from a burning surface. Phase-interaction terms are calculated based on the instantaneous state variables of the gaseous phase in a certain particle position.

As shown in Fig. 74, since the data point of the gaseous phase differs from the data point of the particle phase, interpolation of data is needed for the calculation of an interaction term.

As for the gaseous phase, Eq. (181) is solved by an Eulerian method time-dependently with the phase-interaction terms evaluated from Eq. (187).

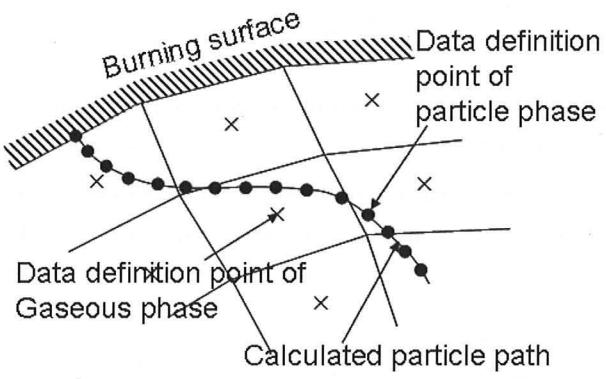

Fig. 74 Eulerian-Lagrangian method

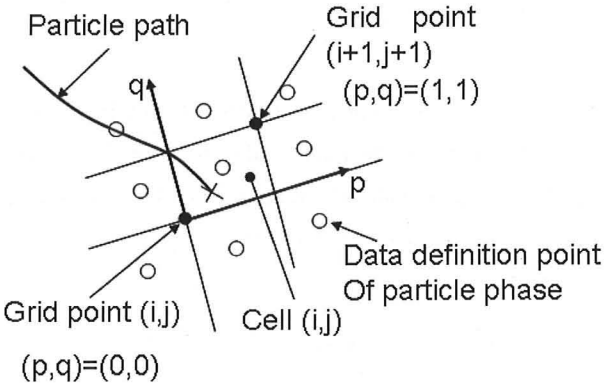

Fig. 75 Local coordinate system (p,q)

Interpolation of gaseous-phase data at a particle location

In order to evaluate Eq. (178), it is necessary to know the properties of gaseous phase at the particle location (x_p, y_p, z_p) at the time t. As described previously, since the data definition points of the particle phase differ from those of the gaseous phase, the properties are evaluated by an interpolation.

Here, for the sake of simplicity, let us consider a two-dimensional situation shown in Fig. 75. An extension to a three-dimensional problem is straightforward. Now, let us consider a particle in the cell (i, j) and introduce a local coordinate system (p, q) which has the origin at the grid point (i, j) and at the same time (p, q)=(1, 1) at the grid point (i+1, j+1).

The above-mentioned space is re-divided into the four domains ①, ②, ③, and ④ shown in Fig. 76 and the cells used for interpolation is selected according to the domain the particle belongs to. Here, suppose that the particle belongs to the domain ① as an example. The procedure is the same for the other domains.

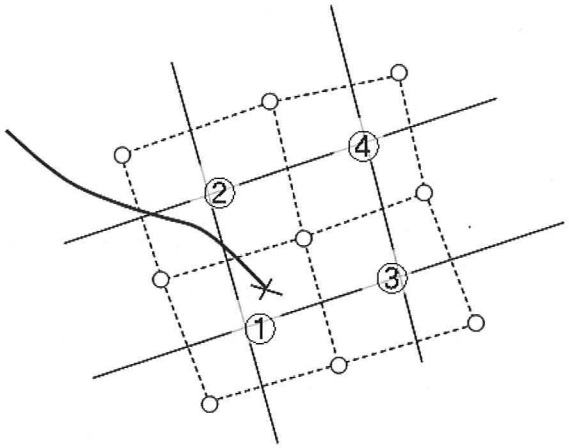

Fig. 76 Interpolation at the particle position

In this example, the particle position is surrounded by the four points

$$\begin{aligned}(p,q) &= (-0.5,-0.5)\\ &= (-0.5,0.5)\\ &= (0.5,-0.5)\\ &= (0.5,0.5)\end{aligned} \tag{189}$$

Denoting $p1 = -0.5$, $p2 = 0.5$, $q1 = -0.5$, $q2 = 0.5$, a quantity Q_g at the particle position (p^*, q^*) can be interpolated as

$$\begin{aligned}Q_g(p^*,q^*) = {} & (p_2-p^*)(q_2-q^*)\,Q_g(p_1,q_1)+(p_2-p^*)(q^*-q_1)\,Q_g(p_1,q_2)\\ & +(p^*-p_1)(q_2-q^*)\,Q_g(p_2,q_1)+(p^*-p_1)(q^*-q_1)\,Q_g(p_2,q_2)\end{aligned} \tag{190}$$

Whereas the physical space coordinates of the virtual cell in the outside of a boundary are not required in this method, the physical properties in a virtual cell are required in the interpolation including around the corner such as $(i, j)=(0, 0)$.

Calculation of a particle path

The position of a particle is traced not with the values of (x, y) but by the combination of values of (i, j) and (p, q).

First of all, the relationship between (x, y) and (p^*, q^*) are obtained by interpolation inside a cell. Since a coordinate point is defined on each grid point, inserting $p1 = 0.0$, $p2 = 1.0$, $q1 = 0.0$, $q2 = 1.0$ in Eq.(190), the interpolated particle location, which is in a cell (i, j) can be expressed as follows.

$$\begin{aligned}x(p^*,q^*) = {} & (1-p^*)(1-q^*)\,x_{i,j}+p^*(1-q^*)\,x_{i+1,j}\\ & +(1-p^*)q^*\,x_{i,j+1}+p^*q^*\,x_{i+1,j+1}\end{aligned} \tag{191}$$

$$\begin{aligned}y(p^*,q^*) = {} & (1-p^*)(1-q^*)\,y_{i,j}+p^*(1-q^*)\,y_{i+1,j}\\ & +(1-p^*)q^*\,y_{i,j+1}+p^*q^*\,y_{i+1,j+1}\end{aligned} \tag{192}$$

The equation of motion of a particle in Eq. (178) can be rewritten as

$$\begin{pmatrix} \frac{\partial x}{\partial p} & \frac{\partial x}{\partial q} \\ \frac{\partial y}{\partial p} & \frac{\partial y}{\partial q} \end{pmatrix} \begin{pmatrix} \frac{dp}{dt} \\ \frac{dq}{dt} \end{pmatrix} = \begin{pmatrix} u_p \\ v_p \end{pmatrix}. \tag{193}$$

With $\frac{\partial x}{\partial p}$, $\frac{\partial x}{\partial q}$, $\frac{\partial y}{\partial p}$, $\frac{\partial y}{\partial q}$ determined by differentiating Eqs. (191) and (192), the values of $\frac{dp}{dt}$ and $\frac{dq}{dt}$ can be obtained by solving Eq.(193). The equation (178) is numerically integrated over an appropriate time step Δt to determine the position and the velocity of a particle after the time interval Δt. What is always necessary about particle path calculation is to trace the set of values of (p, q) and (i, j), by increasing i (or j) by one when p (or q) exceeds one, and by reducing i (or j) by one when p (or q) becomes smaller than zero.

Time-wise integration

A second-order Runge-Kutta method is utilized to integrate Eq. (178). Time-step size Δt is set to about 1/100 of the amount of time in which it takes for the particle to cross the cell. Computational time will be saved if Δt is enlarged or a simpler integration method is used, but, since the integration error will be piled up to make final paths differ from the correct one, it is desirable to choose an appropriate method in which the error is restrained as small as possible.

Boundary conditions

As for the gaseous phase, the same boundary conditions as the Eulerian method are applied. For the particle phase, the following boundary conditions are imposed.

Solid wall: It is easier by the Lagrangian method to set up a boundary condition under which a particle reflects on the wall surface.

- Slip wall: The wall-normal component of the velocity vanishes and the tangential component is reserved. The particle path calculation is continued after the impingement.
- Non-slip wall: Calculation of a particle path is stopped at the particle impingement to a wall.
- Reflecting wall: The mirror-reflection velocity is given at the particle impingement to the wall and the particle path calculation is continued.

Burning surface: The initial values of particle properties are given at a burning surface. A burning surface is divided suitably to determine the initial position of particle-path calculation. The initial speed of a particle is set equal to the gas-phase injection speed (no velocity-lag condition) in the normal direction of the burning surface. The total mass flux is determined by the same method described in the Eulerian-Eulerian method. For the sake of the calculation of the phase-interaction term, the amount of the mass which a simulation particle represents is stored in memory for every particle path. It is necessary to make the product, "the total number of particle" × "the mass represented by a simulation particle" × "injection speed", be in agreement with the total amount of the particle-phase mass flow from the burning surface. The initial temperature is set equal to the combustion temperature (no temperature lag condition).

Axis of center: A particle is considered to cross the axis. Especially, in an axisymmetric flow, a particle path is calculated as it reflects with the axis of center. Thereby, it is realized that particle groups can pass crossing each other.

Nozzle exit: A particle-path calculation is terminated at the nozzle exit.

Steady-state calculation

In a steady-state calculation, once a particle path is calculated, the amount of phase-interaction term can be calculated by dividing the path into particle groups taking advantage of the steady-state solution. Denoting the particle mass flow rate

at the starting point by $\dot{m}$, the mass of particles included in the particle group defined on the particle path is given by $\dot{m}\Delta t$. Here, Δt is the time-step size used in the particle path calculation. This is explained schematically in Fig. 77. Since it is not necessary to store the discrete points on the particle path one by one, large saving of computational resources can be attained in this case.

Furthermore, in steady-state solution process, it is not necessary to calculate the phase-interaction term at each time step. Since a particle-path calculation is the most time consuming process, it is better off reducing the frequency of calculation of the interaction term, for example, every 20 gaseous-phase iterations, in order to reduce the total computation time.

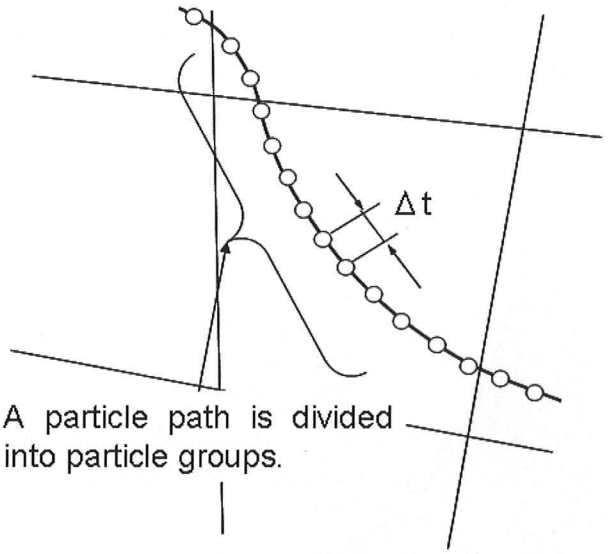

Fig. 77 Steady-state calculation

3.2.3. Influence of a particle diameter distribution

Particle diameter distribution

So far, in the above discussions, particle diameter has been fixed to one kind at a time. However, the size of the aluminum / alumina particles in SRM in fact varies significantly. Therefore, let us investigate the influence of a particle diameter distribution on the flow field.

In an actual SRM, the aluminum particles change their diameter by the combustion during floating. In addition to that, there is coalescence due to particle collisions and/or break-up due to severe shear force. A particle diameter distribution within combustion chamber is usually different from that within the nozzle from these reasons.

However, for the sake of simplicity, the particle diameter distribution obtained from the exhaust combustion gas in static firing tests is used in this section, and no change of diameter of a particle is considered. The mathematical model and analyses on these real effects will be described later in the paper.

It is known that the particle diameter distribution of a particle is well expressed by a log-normal distribution function as

$$\phi(D_p) = \frac{C_1 \exp\left[-\left\{\delta \ln\left(\frac{D_p}{D_{43}}\right)\right\}^2\right]}{D_p^{\,4}}, \tag{194}$$

where ϕ designates probability density function, C_1 constant for normalization defined from $\int \phi(D_p)\, dD_p = 1$, D_{43} the mass-averaged particle diameter, and δ a shape factor of distribution function (usually between 0.9 and 1.1).

The mass-averaged particle diameter D_{43} extracted from exhaust plume has a correlation with the throat diameter D_t, and is approximated by the following formulas.[31]

$$D_{43} = 1.406\, D_t^{\,0.2932} \tag{195}$$

Here the unit of D_{43} is μm and that of D_t is millimeter.

In Fig. 78, the measured distribution from a firing test of a motor with 79mm-diameter nozzle throat and a corresponding log-normal distribution of Eq.(194) are compared.[32] It turns out that the measured distribution is approximated well by Eq.(194), in which δ is set to 1.1.

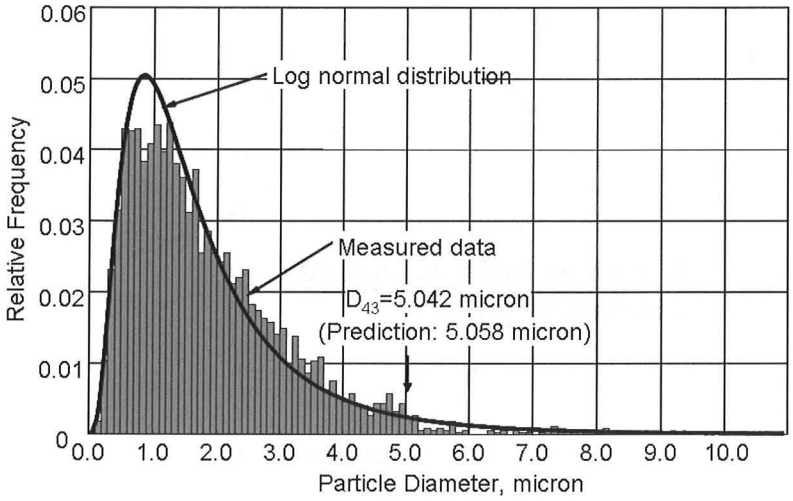

Fig. 78 Particle diameter distribution, and comparison with a log-normal distribution

Numerical experiment to investigate the influence of a particle diameter distribution

The computer code used is based on the Eulerian-Lagrangian method with functions of distributed particle diameter and detailed fluid-dynamic force and heat transfer added, and is called SPEC-3 (Solid Propulsion Enhanced Code, No.3). Here, a gas-particle flow in a model SRM of Fig. 79 is computed for the conditions summarized in Table 4 to investigate the effect of particle diameter distribution.

Since the throat diameter is 200mm, the mass-averaged particle diameter for this case is evaluated as 6.65 μm from Eq. (195). The probability density distribution of Eq. (194) for this case is shown in Fig. 80, and so is a mass-weighted probability density distribution in Fig. 81, where δ is set to 1.0.

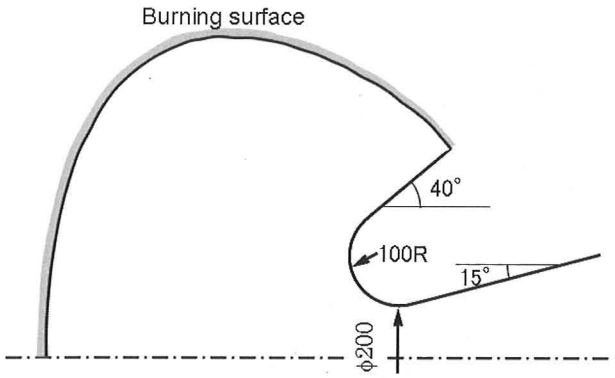

Fig. 79 Model SRM geometry

Table 4 Calculation conditions

Combustion temperature, K		3300
Combustion pressure, MPa		10
Combustion gas	Specific heat ratio	1.22
	Mean molecular weight, g/mol	18.85
Particle (Alumina)	Mass fraction	0.35
	Specific heat, J/kg/K	1427
	Density, kg/m^3	3500

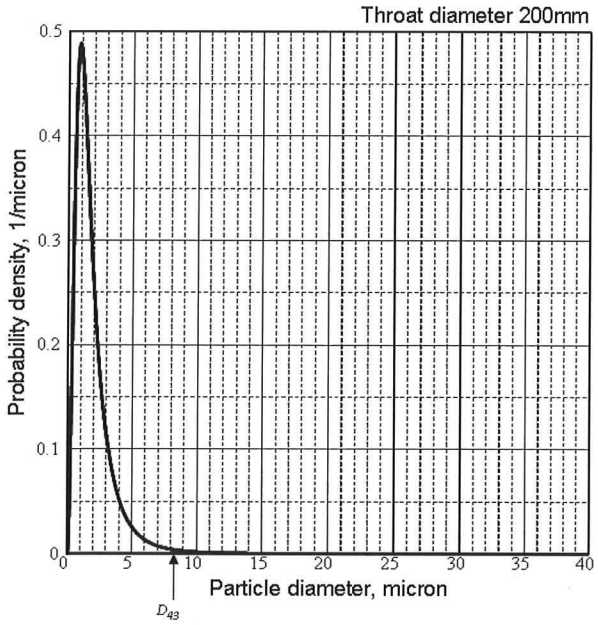

Fig. 80 Probability density distribution of the number of particles to particle diameter (Throat diameter 200mm)

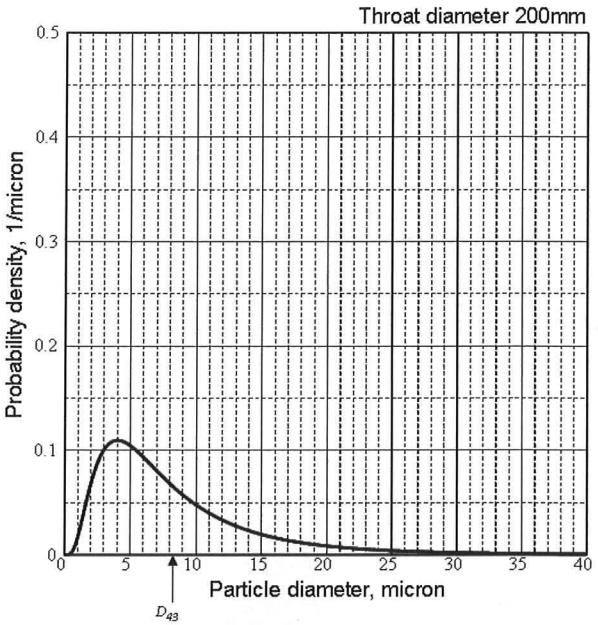

Fig. 81 Mass-weighted probability density distribution (Throat diameter 200mm)

Determination of initial particle diameter

In the simulation, the diameter of a particle is determined by the procedure shown in Fig. 82 for each representative particle generated at a burning surface.

Since the particle with very small diameter follows the gaseous phase without delay, a particle smaller than a certain diameter ($D_{p,\,min}$) is dealt by the phase-equilibrium flow model.

In the analysis, particles are generated from a burning surface with their diameter determined using a random number, the loci of these particles are calculated, and the interaction term between gas and particle, bulk density of particle, etc. are computed. Since the particle groups which each particle represents are determined so that the generated mass flux from a burning surface shall be equal among representative particles, the diameter is determined from a mass-weighted probability density distribution. Moreover, The upper limit of the particle size is defined as $D_{p,\,max}$.

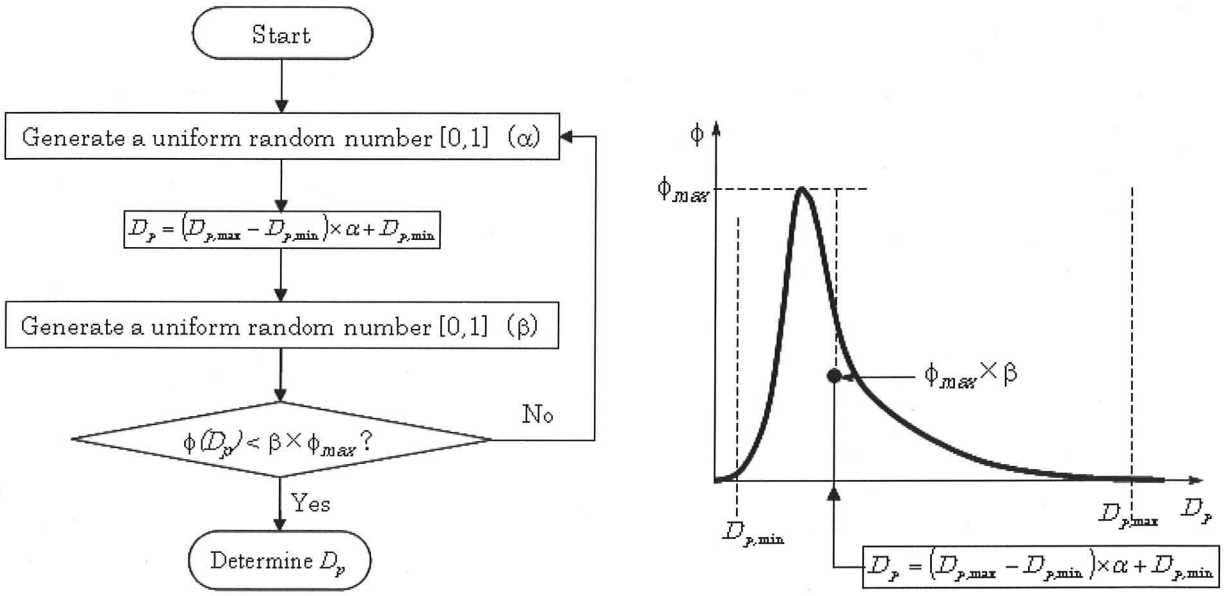

Fig. 82 Particle diameter determination procedure

The histograms of mass-weighted relative frequency and particle number relative frequency for the case of generating 30,000 particles by the above-mentioned procedure ($D_{p,min} = 0$) are shown in Fig. 83 and Fig. 84, respectively. It turns out from these figures that the expected particle diameter distribution can be obtained if there are a sufficient number of sample particles.

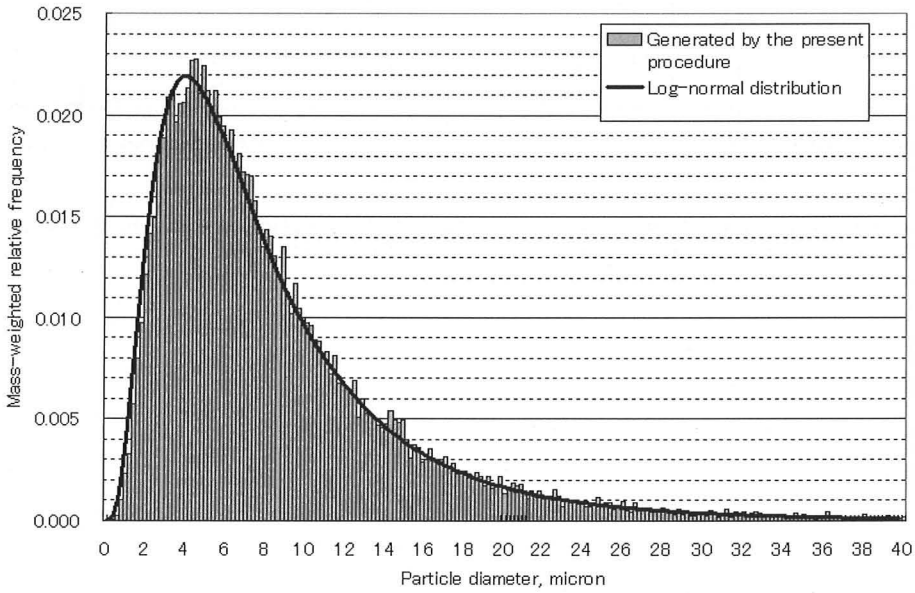

Fig. 83 Mass-weighted relative frequency; comparison with a log-normal distribution

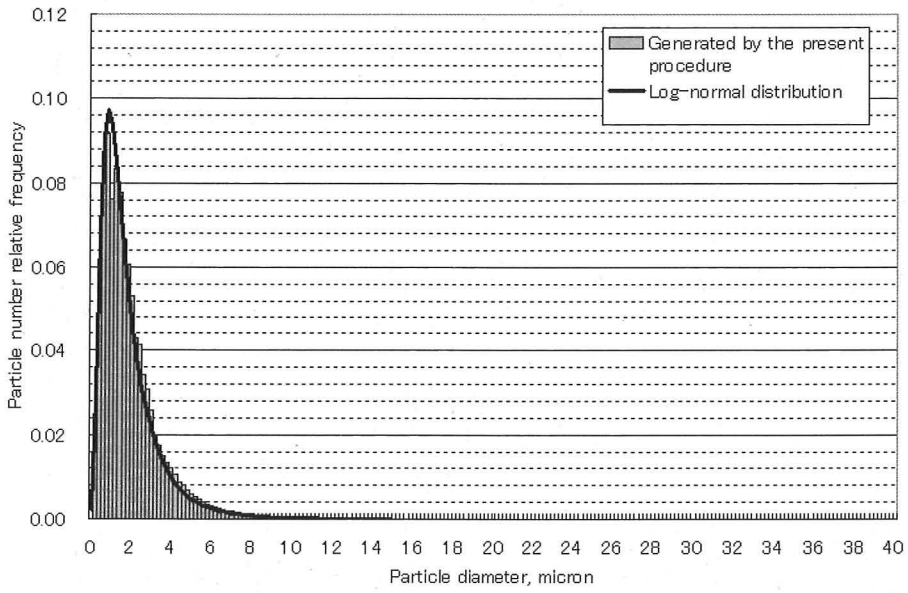

Fig. 84 Particle number relative frequency; comparison with a log-normal distribution

In the flow simulation described below, $D_{p,\,min}$ is set to 0.5 μm and $D_{p,\,max}$ is to six times as large as D_{43}. Since the mass ratio of particles which are smaller than 0.5 μm to the total is about 0.013%, the combustion gas properties are not modified from those of Table 4.

Simulation results

Results of multiphase flow simulation with a particle diameter distribution are shown in each following figure, in which 100 particles per a cell on the burning surface are emitted. Since the burning surface is divided into 40 cells, the total number of particles is 4000.

The bulk number density distribution is shown in Fig. 85, particle temperature in Fig. 86, gas density in Fig. 87, and gas temperature in Fig. 88.

It turns out from these figures that, for the number of particles of this level, statistical error is significant in the flow field because there are too few samples of particles in a calculation cell. Although it is possible to increase the number of particles emitted per one cell to increase the number of sample particles, since a particle path calculations takes a large time, it is not so realistic to increase the number of particle emission extremely.

Next, in order to increase the number of sample particles in a calculation cell within a realistic computation time, a method of time-wise averaging is employed to obtain a smooth steady-state solution. Quantities such as the phase-interaction term, particle bulk density, and particle temperature, etc., are updated, accumulated and time-averaged at each time of a particle locus calculation. By this approach, without increasing much computation time on particle-path calculation, the number of sampled particles per a cell can be increased with the progress of iteration and statistical deviation of an averaged quantity decreases with it.

The simulation results using the time-average technique are shown next. The bulk number density distribution is shown in Fig. 89, particle temperature in Fig. 90, gas density in Fig. 91, and gas temperature in Fig. 92.

In particular, to see the effect of particle diameter distribution, the results of simulations with single particle diameters of 2, 6.65 (D_{43}), and 20 μm, single kind per a simulation, are also shown in Fig. 93, Fig. 94, and Fig. 95, respectively.

Comparison of the particle bulk density distribution along some grid lines is shown in Fig. 97 ~ Fig. 100. Refer to Fig. 96 for the position of a grid line. In domains, such as inside of chamber and near the axis, in which all kinds of particles are

intermingled and distributed with the same particle distribution as is set up at the burning surface, the particle bulk density distribution obtained in distributed-particle- diameter simulation is mostly in agreement with that of single-particle-diameter simulation with the mass-averaged particle diameter, D_{43}.

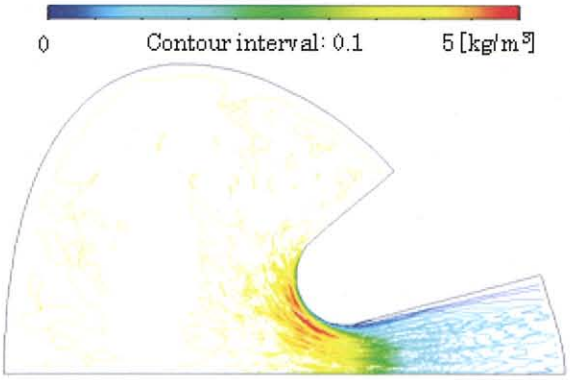

Fig. 85 Particle bulk density distribution

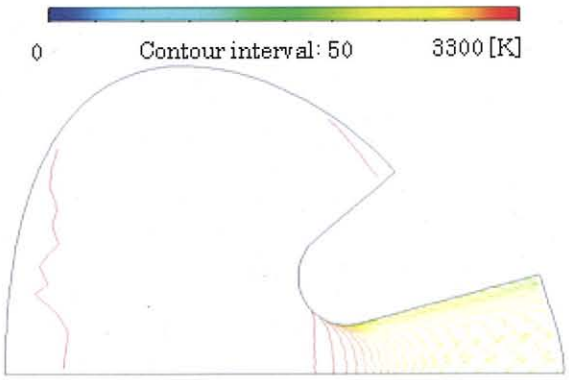

Fig. 86 Particle temperature distribution

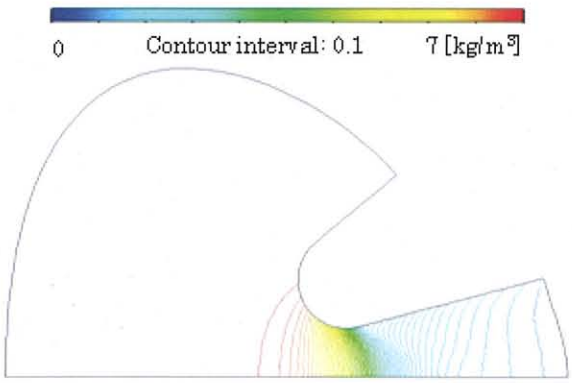

Fig. 87 Gas density distribution

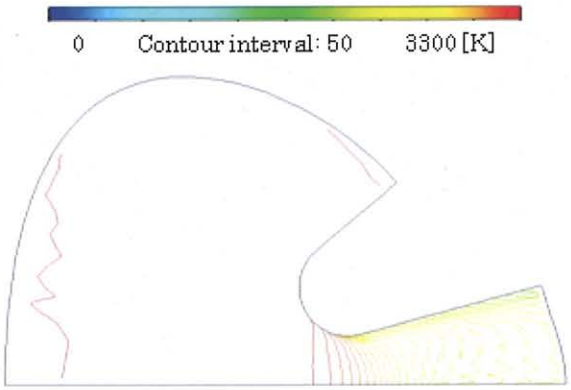

Fig. 88 Gas temperature distribution

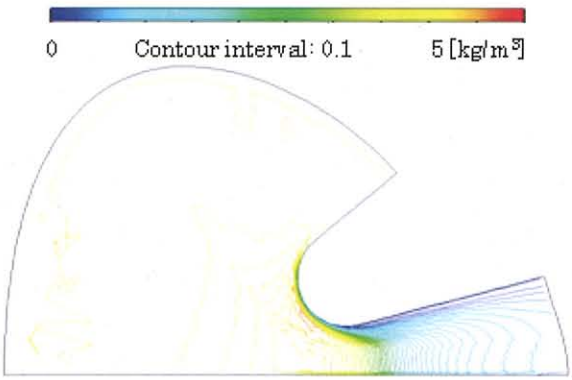

Fig. 89 Particle bulk density distribution, time-averaging technique employed

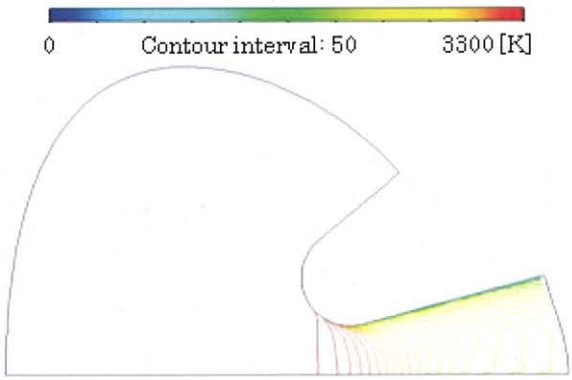

Fig. 90 Particle temperature distribution, time-averaging technique employed

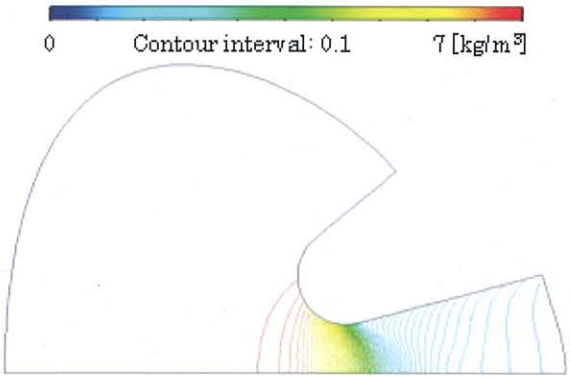

Fig. 91 Gas density distribution, time-averaging technique employed

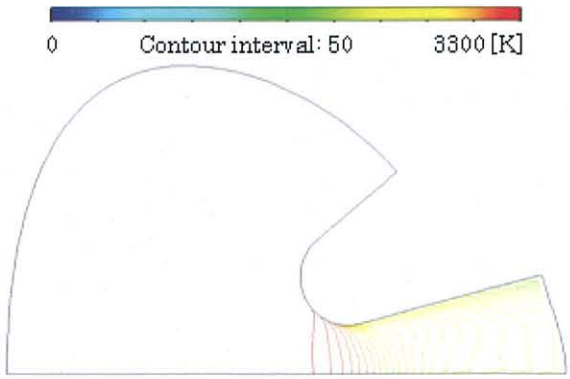

Fig. 92 Gas temperature distribution, time-averaging technique employed

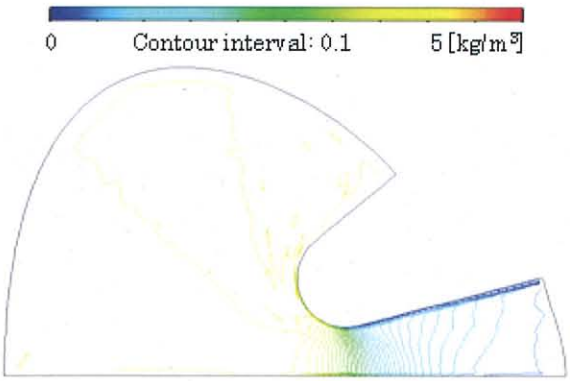

Fig. 93 Particle bulk density distribution, single particle diameter of 2 μm

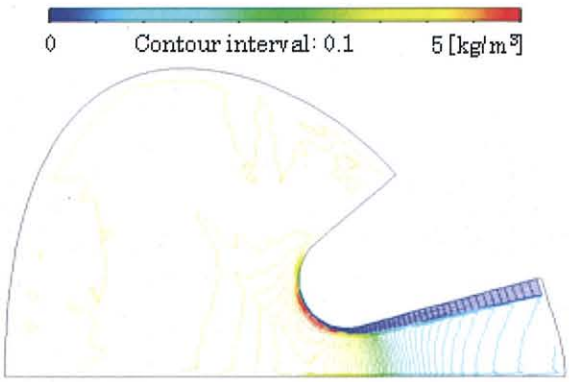

Fig. 94 Particle bulk density distribution, single particle diameter of 6.65 μm

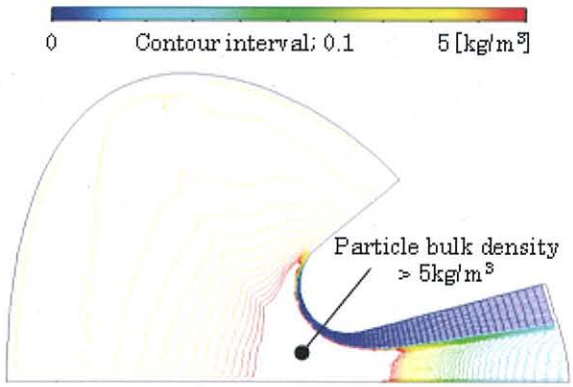

Fig. 95 Particle bulk density distribution, single diameter of 20 μm

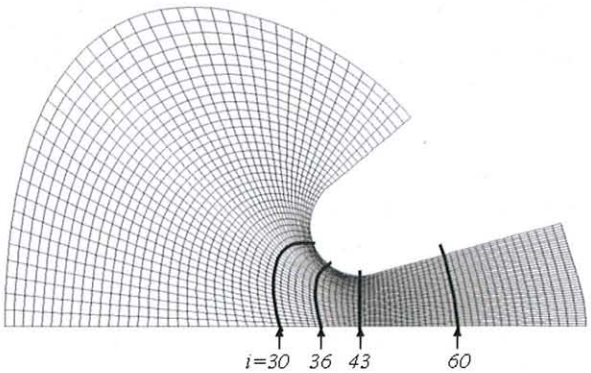

Fig. 96 Grid system for computation

On the other hand, near the surface of a wall, since the size of a particle free zone changes with particle diameter, a local particle diameter distribution differs from the distribution set up at the burning surface. The particle bulk density distribution near the wall surface obtained in distributed-particle simulation looks like a superposition of three simulation results of single particle diameters (2, 6.65, and 20 μm). It has no sharp limiting particle streamline as is seen in single-

particle simulation, but has a distributed bulk particle density which decreases gently-sloping toward the surface of a wall.

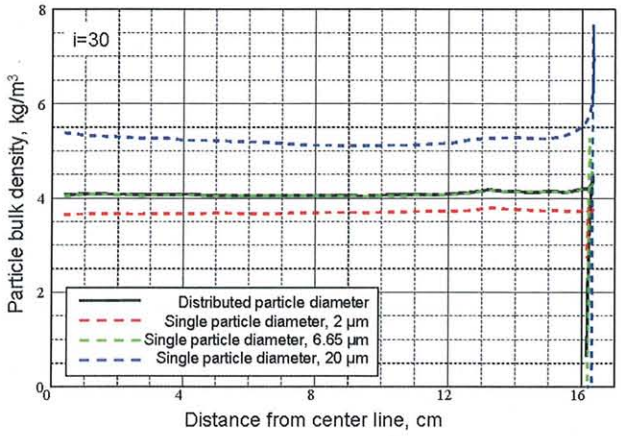

Fig. 97 Comparison of particle bulk density, i=30

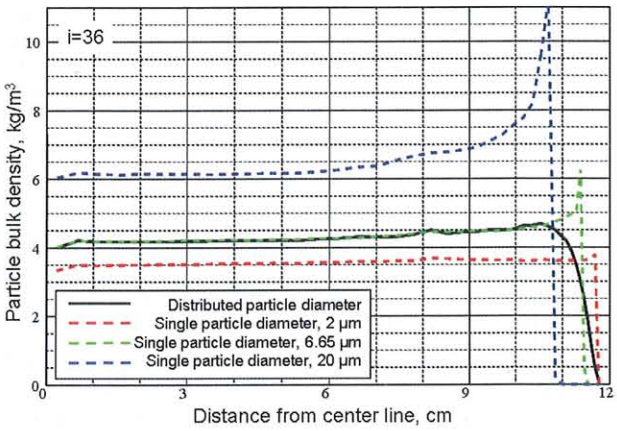

Fig. 98 Comparison of particle bulk density, i=36

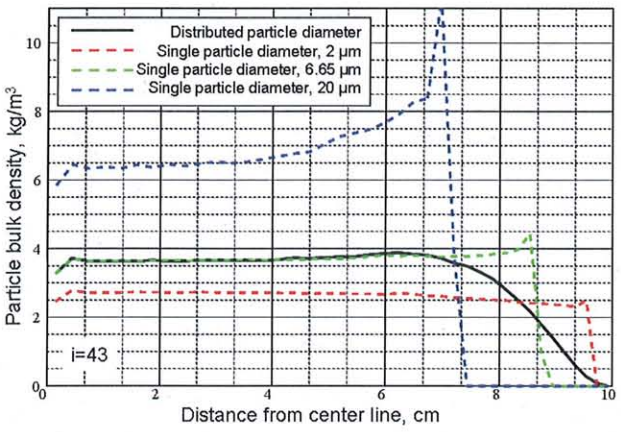

Fig. 99 Comparison of particle bulk density, i=43

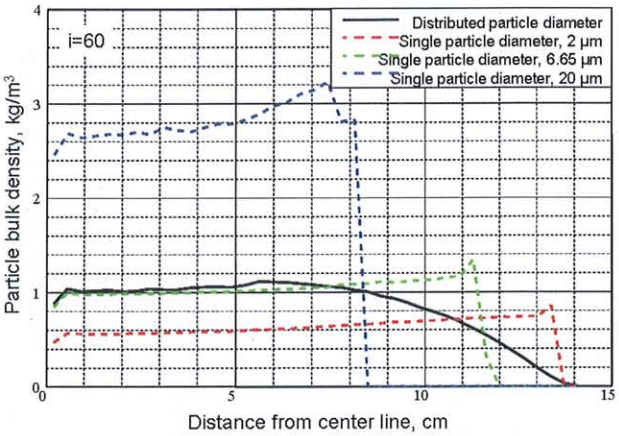

Fig. 100 Comparison of particle bulk density, i=60

3.3. Eulerian-hybrid method

So far, the diameter of a particle is generated from a certain distribution function at a burning surface, including single diameter case, and is fixed throughout the computation. Namely, the change of the particle diameter due to combustion and/or breakup due to shear force has not been taken into account. It is a fact that an agglomerate droplet is too large to represent particles in the nozzle section, whereas an alumina particle at the nozzle-exit is too small to represent particles near a burning surface.

The important role of the distributed combustion is reviewed in recent literatures from the view point of particle effects on the acoustic stability of multiphase flow in SRM. Several researchers are working on constructing a realistic simulation method of distributed combustion.[26] A more realistic model can be built by taking into account the particle-diameter change due to combustion and breakup during the flight inside SRM.[33] (The coalescence of particle by particle collision is not considered here.)

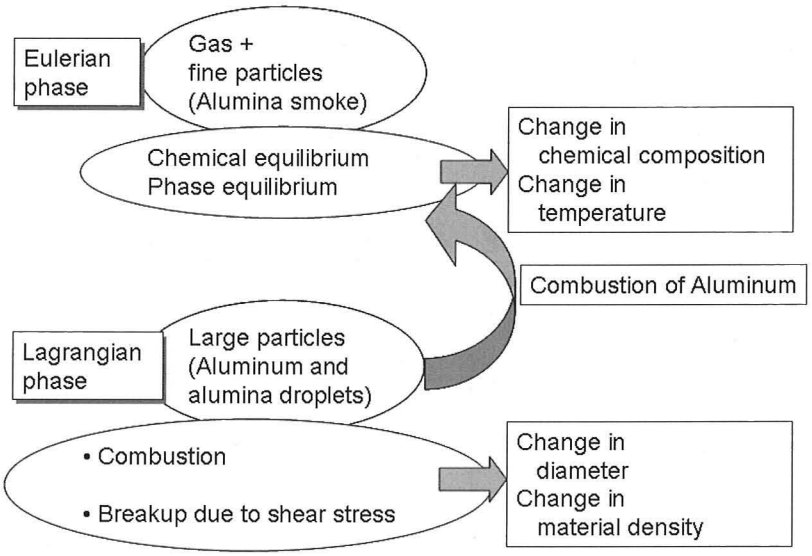

Fig. 101 Schematic of Eulerian-hybrid method

In order to deal with the change of particle diameter, the Lagrangian method is suitable because the governing equation for the particle-phase is written for an individual particle. Therefore, the Lagrangian method is adopted for the simulation of burning particle with comparatively large diameters. The diameter of particle decreases as combustion progresses and combustion affects the gaseous-phase composition and temperature.

Since a fine particle like alumina smoke has strong interaction with the gaseous phase, the gaseous phase containing an alumina smoke can be treated as a single fluid, namely, the concept of phase-equilibrium flow can be applied. Since a phase-equilibrium flow can be computed by the Eulerian method, the analysis method for the particle-phase here is a hybrid method consisting of both the Lagrangian and the Eulerian methods. With the gaseous-phase computed by the Eulerian method, the present method can be called an Eulerian-hybrid method. A schematic explanation of the method is given in Fig. 101.

A computer program is developed along with the Eulerian-hybrid method to calculate multiphase flow in SRM. The program is named SPEC-4 (Solid Propulsion Enhanced Code, No.4).

Assumptions

Let us set the followings as premises here.

- The chemical reaction is sufficiently fast so that chemical equilibrium is established in the gaseous phase in each cell.
- The velocity and the temperature of very small alumina particles (alumina smoke) are always identical with those of the gaseous phase, respectively.
- The volume of a particle is disregarded.
- Particles collision is disregarded and particle coalescence is not taken into account.
- The physical properties of a particle are fixed and independent of the temperature.
- Particles are spherical.
- The temperature distribution within a particle is disregarded.
- Although the gaseous phase is assumed to be inviscid, a viscous effect is taken into account in the phase-interaction term.
- A particle is the mixture of aluminum and alumina at the initial state and the quantity of alumina within a particle does not change during its flight in SRM.

3.3.1. Governing equations

Eulerian phase: Let us use the name, the Eulerian phase, instead of the gaseous phase, because the phase contains gas and alumina smoke. The basic equation for the Eulerian phase can be written as follows for the conservations of the mass, the momentum, the energy, and the aluminum mass, respectively. The gas-particle interaction term S_g and the combustion term S_c are added as source terms.

$$\frac{\partial \mathbf{Q}}{\partial t}+\frac{\partial \mathbf{E}}{\partial x}+\frac{\partial \mathbf{F}}{\partial y}+\frac{\partial \mathbf{G}}{\partial z}=\mathbf{S}_c+\mathbf{S}_g \tag{196}$$

$$\mathbf{Q}=\begin{pmatrix}\rho\\ \rho u\\ \rho v\\ \rho w\\ e\\ \rho_{Al}\end{pmatrix},\quad \mathbf{E}=\begin{pmatrix}\rho u\\ \rho u^2+p\\ \rho uv\\ \rho uw\\ (e+p)u\\ \rho_{Al}u\end{pmatrix},\quad \mathbf{F}=\begin{pmatrix}\rho v\\ \rho uv\\ \rho v^2+p\\ \rho vw\\ (e+p)v\\ \rho_{Al}v\end{pmatrix},\quad \mathbf{G}=\begin{pmatrix}\rho w\\ \rho uw\\ \rho vw\\ \rho w^2+p\\ (e+p)w\\ \rho_{Al}w\end{pmatrix} \tag{197}$$

$$\mathbf{S}_g=\begin{pmatrix}0\\ -\sum_{k=1}^{N_p}\frac{N_{Tk}}{V}A\left(u_g-u_p^k\right)\\ -\sum_{k=1}^{N_p}\frac{N_{Tk}}{V}A\left(v_g-v_p^k\right)\\ -\sum_{k=1}^{N_p}\frac{N_{Tk}}{V}A\left(w_g-w_p^k\right)\\ -\sum_{k=1}^{N_p}\frac{M_k}{V}\left[A\left(u_p^k\left(u_g-u_p^k\right)+v_p^k\left(v_g-v_p^k\right)+w_p^k\left(w_g-w_p^k\right)\right)+B\left(T_g-T_p^k\right)\right]\\ 0\end{pmatrix} \tag{198}$$

$$\mathbf{S}_c=\begin{pmatrix}\dot{w}\\ \dot{w}u_p\\ \dot{w}v_p\\ \dot{w}w_p\\ \frac{1}{2}\dot{w}\left(u_p^2+v_p^2+w_p^2\right)\\ \dot{w}\end{pmatrix} \tag{199}$$

Here, ρ is the density of the Eulerian phase, (u, v, w) the velocity components in (x, y, z) directions, p the pressure, T the temperature, e the total energy per unit volume, and subscripts g and p denote the gaseous phase and the particle phase, respectively. The aluminum bulk density in the Eulerian phase is denoted by ρ_{Al}. The mass generation of the Eulerian-phase alumina due to combustion of the Lagrangian-phase aluminum droplet is denoted by $\dot{w}$. It should be noted that ρ_{Al} represents the bulk density of aluminum, no matter in what molecular state or phase it exists.

The rate of change of momentum or energy is calculated by adding contribution from all the particle groups (denoted by superscript k) contained in an inspection volume, i.e., in each cell in an actual computation, and then dividing it by the volume V of the inspection volume. The total number of particles in the k-th particle group is designated by N_{Tk} and is determined from the amount of particle mass of the k-th group injected at the burning surface and the initial particle diameter, i.e.,

$$N_{Tk} = \frac{M_k}{\left(\frac{\pi}{6} D_{p0}{}^3 \sigma_{m0}\right)_k}. \tag{200}$$

Here the mass injected at the starting point is denoted by M_k, the initial diameter by D_{p0}, and the particle true density at the starting point by σ_{m0}. Among them, the particle diameter and the true density change according to the particle combustion.

The phase-interaction term can be evaluated by the same manner previously described. Here the formula of Henderson[9] is used for the drag coefficient and that of Kavanau-Drake[14] is used for the Nusselt number.

Since the local chemical equilibrium is assumed, chemical composition differs in every cell and the equation of state cannot be expressed by a simple formula like in the case of ideal gas. The temperature, the mean molecular weight, and the specific heat ratio will be computed using the density, internal energy, and the aluminum bulk density of the Eulerian phase, i.e.,

$$T_g = T_g(\rho, e_n, \rho_{Al}), \tag{201}$$

$$M_g = M_g(\rho, e_n, \rho_{Al}), \tag{202}$$

$$\gamma = \gamma(\rho, e_n, \rho_{Al}), \tag{203}$$

where e_n is the internal energy per unit volume and can be written as

$$e_n = e - \frac{1}{2}\rho\left(u_g{}^2 + v_g{}^2 + w_g{}^2\right). \tag{204}$$

Lookup tables of the functions of Eqs. (201)～(203) are implemented in the present method. These tables are created beforehand with chemical equilibrium analysis software CET89[34] (Chemical Equilibrium with Transport Properties, 1989). The method of making the tables and referring them will be mentioned later.

The pressure and the speed of sound are calculated using the temperature, mean molecular weight and the specific heat ratio obtained from lookup tables as

$$p = \rho \frac{\tilde{R}}{M_g} T_g, \qquad a = \sqrt{\gamma \frac{\tilde{R}}{M_g} T_g}, \tag{205}$$

where $\tilde{R}$ is the universal gas constant (8314 J/kg/kmol).

Lagrangian phase: The particle groups with comparatively large diameter dealt with the Lagrangian method will be called the Lagrangian phase. In the Lagrangian phase computation, a particle path is calculated taking the interaction with the Eulerian phase into account. A simulation particle treated as the Lagrangian phase is representing a particle group which consists of many real particles. The behavior of a particle group is computed from the locus of one representative (simulation) particle. The present method, therefore, is premised on the following matters.

A particle group is small enough that its behavior can be represented by the particle which exists at its center. That is, the velocity and the temperature of all the particles belonging to a particle group are equal to those of a representative particle.

The exchanges of the momentum and the energy with the Eulerian phase are presupposed to be equal to the product of the total number of real particles contained in a particle group and the amount of the interaction per a simulation particle.

The basic equation of the Lagrangian phase can be written as follows.

$$\frac{d\mathbf{W}}{dt} = \mathbf{S}, \tag{206}$$

$$\mathbf{W} = \begin{pmatrix} x_p \\ y_p \\ z_p \\ u_p \\ v_p \\ w_p \\ C_{Pp}T_p \end{pmatrix} \qquad \mathbf{S} = \begin{pmatrix} u_p \\ v_p \\ w_p \\ \frac{A}{m_p}(u_g - u_p) \\ \frac{A}{m_p}(v_g - v_p) \\ \frac{A}{m_p}(w_g - w_p) \\ \frac{B}{m_p}(T_g - T_p) \end{pmatrix}, \tag{207}$$

where m_p is the mass of a particle.

In the Lagrangian method, the basic equation shown in Eq. (206) is solved to obtain the particle path and the temperature of the representative particle which has been generated from a burning surface. The position and the temperature of a representative particle are discretely evaluated and updated at appropriate intervals. The phase-interaction terms are calculated based on variables of the Eulerian phase at a certain instantaneous particle position which are interpolated from the data of the Eulerian phase.

Here, the particle diameter changes from time to time according to the combustion of the particle. The change of particle diameter is calculated as follows.

Let us denote the particle-mass-consumption rate due to combustion per a particle per unit time by $\dot{m}$, and the volume fraction of alumina in the particle by ϕ. The mass of a particle before combustion starts can be expressed as

$$m_p = \frac{\pi}{6} D_p{}^3 \left(\phi\sigma_{Al2O3} + (1-\phi)\sigma_{Al}\right), \tag{208}$$

where σ_{Al2O3} and σ_{Al} are the true density of alumina and aluminum, respectively. The true density of a particle σ_m can be defined as

$$\sigma_m = \phi\sigma_{Al2O3} + (1-\phi)\sigma_{Al}. \tag{209}$$

Denoting the state after a small time Δt by the superscript "*new*", the mass of a particle can be written as follows, considering the mass loss due to combustion,

$$\begin{aligned} m_p^{new} &= m_p - \dot{m}\Delta t \\ &= \frac{\pi}{6} D_p^{new\,3} \left(\phi^{new}\sigma_{Al2O3} + (1-\phi^{new})\sigma_{Al}\right). \end{aligned} \tag{210}$$

Since it is assumed that the mass (volume) of the alumina contained in a particle does not change and only aluminum is lost by combustion, the following relationships will hold.

$$V_{Al2O3}^{new} = V_{Al2O3} = \frac{\pi}{6} D_p{}^3 \phi \tag{211}$$

$$V_{Al}^{new} = V_{Al} - \frac{\dot{m}\Delta t}{\sigma_{Al}} = \frac{\pi}{6} D_p{}^3 (1-\phi) - \frac{\dot{m}\Delta t}{\sigma_{Al}} \tag{212}$$

$$\phi^{new} = \frac{V_{Al2O3}^{new}}{V_{Al}^{new} + V_{Al2O3}^{new}} \tag{213}$$

New particle diameter D_p^{new} is determined by solving Eqs. (210) ~ (213).

Combustion of a particle terminates when all the aluminum ingredients contained in the particle have been burnt, ϕ =1. After that, the alumina, the remnants, will fly as the condensed phase without combustion. The particle diameter of final alumina is determined by the amount of the alumina contained in the initial particle left from the burning surface.

The aluminum lost by combustion is added to the Eulerian phase in the source term. The term $\dot{w}$ in Eq. (199) is calculated as

$$\dot{w} = \sum_{k=1}^{N_p} \frac{N_{Tk}}{V} \dot{m}_k \tag{214}$$

The following paragraph describes models for the mass consumption in combustion.

3.3.2. Combustion model of an aluminum droplet

For the moment, the reliable physical model which models the combustion process of an aluminum particle in detail is not available. The combustion models advocated are empirical formulae commonly having the form of Eq. (215) with modifications of a coefficient.

$$\dot{m} = -\frac{\pi}{2}\sigma_{Al}\frac{k}{n}D_p^{3-n} \tag{215}$$

The unit of k is $[m^n/s]$.

Three combustion models are shown below. In the formulae, p denotes the pressure in [Pa], T the temperature in [K], D_p the particle diameter in [m] and X the molar fraction of each chemical species.

Hermsen model[35]

$$\begin{aligned} &n = 1.8 \\ &k = 1.9197\times10^{-9}\cdot A_k^{0.9}\cdot p^{0.27} \\ &A_k = 100\left(X_{CO_2} + X_{H_2O} + X_{O_2} + X_O + X_{OH}\right) \end{aligned} \tag{216}$$

Beckstead model[36]

$$\begin{aligned} &n = 1.9 \\ &k = 3.4891\times10^{-13}\cdot A_k^{0.39}\cdot p^{0.2}\cdot T^{1.57}\cdot D_{rel} \\ &A_k = 0.22X_{CO_2} + 0.58X_{H_2O} + X_{O_2} \\ &D_{rel} = 1 + 2.7X_{H_2} \end{aligned} \tag{217}$$

Modified Beckstead model[37]

$$\begin{aligned} &n = 1.8 \\ &k = 6.2566\times10^{-7}\cdot A_k\cdot p^{0.1}\cdot T^{0.2} \\ &A_k = 0.22X_{CO_2} + 0.6X_{H_2O} + X_{O_2} \end{aligned} \tag{218}$$

In order to see the difference among these combustion models, change of the particle diameter by combustion of the particle of 100% aluminum is compared for constant temperature, pressure, and chemical composition of the surrounding gas. When the temperature, pressure and composition of surrounding gas are set constant, Eq. (215) can be integrated

easily to give the change of particle diameter as

$$D_p^{\ n} = D_{p0}^{\ n} - kt\,, \tag{219}$$

where D_{p0} is the initial particle diameter.

The temperature and the compositions are determined from a chemical equilibrium calculation for the material consisting of 85% AP and 15% HTPB under the pressure of 5 MPa or 10 MPa as listed in Table 5.

Table 5 Parameter values

Pressure		5 MPa	10 MPa
Temperature		2823 K	2842 K
Molar fraction	CO_2	0.09015	0.09050
	O_2	0.00015	0.00009
	H_2O	0.36136	0.36299
	OH	0.00419	0.00323
	O	0.00010	0.00006
	H_2	0.09988	0.09944
Initial diameter		150 μm	150 μm

The particle diameter change with time by each model is shown in Fig. 102 and Fig. 103. In this setup, it turns out that any result of a model resembles each other concerning the burn-out period (characteristic time) of the particle of 150 μm, and is 35 ~ 40 msec for the pressure of 5MPa and 30 ~ 35 msec for 10MPa. It also turns out that Harmsen model gives a little higher combustion rate and that the difference between Beckstead model and modified Beckstead model tends to be conspicuous as the pressure becomes high. It is beyond the scope of this paper to discuss on which combustion model should be used, since it needs the details of the combustion mechanism of an aluminum particle. Although the model of Harmsen will be used in the following calculation, it is comparatively easy to incorporate the other models.

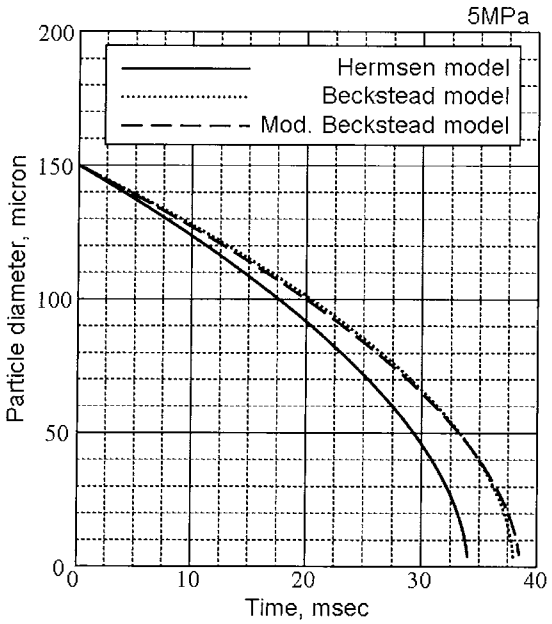

Fig. 102 Comparison of combustion model (5MPa)

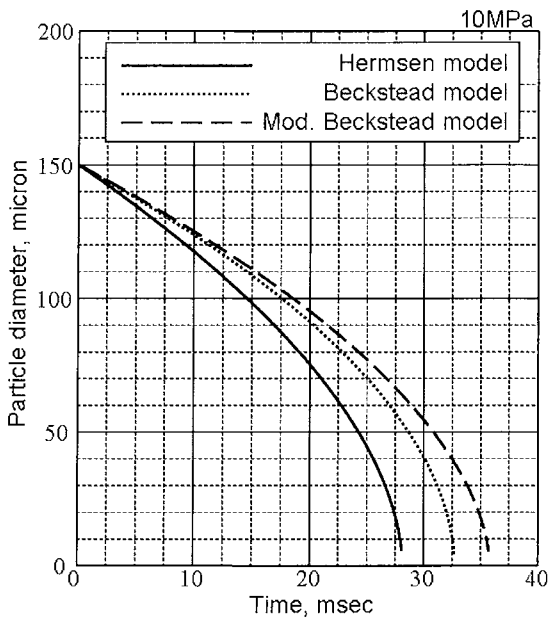

Fig. 103 Comparison of combustion model (10MPa)

3.3.3. Calculation of chemical equilibrium

As mentioned previously, the chemical equilibrium states are computed beforehand by a software like CET89 and summarized in lookup tables. The temperature, mean molecular weight, specific heat ratio, total molar fraction of oxidizing chemical species, and mass fraction of alumina smoke are determined by referring to these lookup tables. Here, the methods of making and referring a table are described.

As a propellant, composite propellant consisting of the chemical composition summarized in Table 6 is assumed.

Table 6 Propellant components

Component	Mass fraction
AP	68%
HTPB	12%
Al	20%

The temperature and species composition in the chemical equilibrium are calculated using CET89. In order to calculate with aluminum fraction as a parameter, it is convenient to use a stoichiometric coefficient and the standard enthalpy of formation for the mixture of 68%-AP and 12%-HTPB. The density, the internal energy, and the aluminum mass fraction are to be parameters in the lookup tables. They are the inputs for the calculations to obtain the temperature, mean molecular weight, specific heat ratio, molar fraction of oxidizing gas species, and mass fraction of alumina smoke. The ranges of parameters are summarized in Table 7. In Table 9 ~ Table 13, the obtained data are listed.

Table 7 Parameter range

Parameter	Range
Mass fraction of Al	0%, 5%, 10%, 15%, 20%, 25%
Internal energy, MJ/kg	-1.0, -2.0, -3.0, -4.0, -5.0, -6.0, -7.0
Density, kg/m^3	0.01, 0.0316, 0.1, 0.316, 1.0, 3.16, 10.0, 31.6

Method of interpolation

In the table-lookup, the input parameters are the density, aluminum mass fraction, and the internal energy. As for the density, $\log_{10}\rho$ is used for an interpolation parameter. Since it is an interpolation with three parameters, firstly the region where the input values are surrounded by the discrete data in the lookup tables are searched for in the parameter space, and then the target value is computed by using a tri-linear interpolation.

Now, let the aluminum mass fraction be denoted by Y_{Al} and the input value shall be between Y_{Al}^{i} and Y_{Al}^{i+1}. Similarly, the internal energy e_n shall be between e_n^j and e_n^{j+1}, and $\log_{10}\rho$ shall be between $(\log_{10}\rho)^k$ and $(\log_{10}\rho)^{k+1}$. Then, e.g., the interpolated temperature can be expressed as

$$\begin{aligned} T = {} & (1-a)(1-b)(1-c)\cdot T(i,j,k) + (1-a)(1-b)c\cdot T(i,j,k+1) \\ & + (1-a)b(1-c)\cdot T(i,j+1,k) + (1-a)bc\cdot T(i,j+1,k+1) \\ & + a(1-b)(1-c)\cdot T(i+1,j,k) + a(1-b)c\cdot T(i+1,j,k+1) \\ & + ab(1-c)\cdot T(i+1,j+1,k) + abc\cdot T(i+1,j+1,k+1) \end{aligned}, \tag{220}$$

where

$$a = \frac{Y_{Al} - Y_{Al}^{i}}{Y_{Al}^{i+1} - Y_{Al}^{i}}, \qquad b = \frac{e_n - e_n^{j}}{e_n^{j+1} - e_n^{j}}, \qquad c = \frac{\log_{10}\rho - \log_{10}\rho^{k}}{\log_{10}\rho^{k+1} - \log_{10}\rho^{k}}. \tag{221}$$

Other properties can be interpolated in the same fashion.

In case that only AP and HTPB burn

The case where only AP and HTPB burn is often referred as an initial condition or boundary conditions for burning surface in the examples of calculation described in the following chapter. Results of chemical equilibrium calculation for this case are summarized in Table 8.

Table 8 Chemical equilibrium results for AP+HTPB burning

Pressure, MPa	Temperature, K	Mole. Weight, g/mol	Mole fraction of oxidizing species	Internal energy, MJ/kg
1	2764.3	24.46	0.453	-3.168
5	2823.8	24.60	0.456	-3.183
10	2842.0	24.64	0.457	-3.187
15	2850.9	24.66	0.457	-3.189
20	2856.4	24.67	0.458	-3.191

3.3.4. Breakup of particle due to shear force

A model of breakup of a particle due to the shear force imposed in the rapidly accelerated flow near the throat is described below. The resisting stress against the shear stress is the surface tension. Therefore, it is thought that breakup of a droplet occurs when the shear stress beats the surface tension. The ratio of a fluid drag and surface tension defines the Weber number and it is necessary to be smaller than the critical value We_c in order for a particle to maintain its shape, i.e.,

$$We = \frac{\rho_g \left| \vec{U}_s \right|^2 D_p}{\sigma_t} < We_c \tag{222}$$

A critical Weber number can be estimated by

$$We_c = \frac{4}{C_D}.^{[26]} \tag{223}$$

In the computation, when the Weber number exceeds the critical value, a particle is assumed to break up into 8 particles of half diameter of the original. When the particle diameter after a breakup is still large, a particle shall be further divided in the next time step.

3.3.5. Setup of initial diameter of a particle

As is mentioned earlier, since aluminum passes through complicated physical processes of melting, agglomeration, departing from the burning surface, and combustion, it is very difficult to determine a particle diameter according to some physical model. Therefore, here, the particle diameter distribution for analysis is set up based on a measured particle diameter distribution. When more detailed particle distribution data is obtained as a result of a newer experiment or advanced combustion research, computational results will be updated.

By using a QPCB (Quenched-Particle Collection Bomb) equipment, the particle diameter distribution near a burning surface can be measured. According to experiments[38], the particle diameter distribution near a burning surface has a bi-modal shape in which there are one peak at the diameter of 1.5 μm and the other at 100 ~ 200 μm. The small particles are combustion products generated near the burning surface and the large particles are mainly unburned droplets consisting of aluminum and alumina. In this research, three kinds of following initial particle diameter distributions are assumed to serve as verification of the computer program, as well as numerical experiments.

Table 9 Temperature, K

Al fraction	Internal energy (J/kg)	Density (kg/m³) 31.6000	10.0000	3.1600	1.0000	0.3160	0.1000	0.0316	0.0100
0%	−1.0E+06	3.7804E+03	3.6327E+03	3.4776E+03	3.3209E+03	3.1669E+03	3.0184E+03	2.8771E+03	2.7438E+03
	−2.0E+06	3.4347E+03	3.3408E+03	3.2327E+03	3.1154E+03	2.9938E+03	2.8718E+03	2.7522E+03	2.6366E+03
	−3.0E+06	2.9695E+03	2.9346E+03	2.8860E+03	2.8236E+03	2.7495E+03	2.6670E+03	2.5794E+03	2.4898E+03
	−4.0E+06	2.3671E+03	2.3634E+03	2.3570E+03	2.3467E+03	2.3304E+03	2.3064E+03	2.2736E+03	2.2321E+03
	−5.0E+06	1.6898E+03	1.6896E+03	1.6894E+03	1.6893E+03	1.6891E+03	1.6887E+03	1.6880E+03	1.6869E+03
	−6.0E+06	1.1036E+03	1.0535E+03	1.0136E+03	9.9154E+02	9.8599E+02	9.8528E+02	9.8520E+02	9.8519E+02
	−7.0E+06	6.2175E+02	6.1683E+02	6.0937E+02	5.9899E+02	5.8565E+02	5.6977E+02	5.5247E+02	5.3390E+02
5%	−1.0E+06	3.9147E+03	3.7547E+03	3.5875E+03	3.4198E+03	3.2558E+03	3.0986E+03	2.9494E+03	2.8092E+03
	−2.0E+06	3.5871E+03	3.4802E+03	3.3589E+03	3.2290E+03	3.0958E+03	2.9632E+03	2.8340E+03	2.7098E+03
	−3.0E+06	3.1583E+03	3.1096E+03	3.0450E+03	2.9661E+03	2.8760E+03	2.7789E+03	2.6784E+03	2.5775E+03
	−4.0E+06	2.6046E+03	2.5955E+03	2.5807E+03	2.5580E+03	2.5253E+03	2.4820E+03	2.4287E+03	2.3674E+03
	−5.0E+06	2.0246E+03	2.0241E+03	2.0232E+03	2.0217E+03	2.0190E+03	2.0145E+03	2.0071E+03	1.9954E+03
	−6.0E+06	1.3429E+03	1.3303E+03	1.3285E+03	1.3282E+03	1.3282E+03	1.3282E+03	1.3282E+03	1.3282E+03
	−7.0E+06	9.6728E+02	9.2414E+02	8.8066E+02	8.3823E+02	7.9785E+02	7.6019E+02	7.2579E+02	6.9536E+02
10%	−1.0E+06	4.0528E+03	3.8803E+03	3.7006E+03	3.5210E+03	3.3464E+03	3.1798E+03	3.0224E+03	2.8749E+03
	−2.0E+06	3.7365E+03	3.6169E+03	3.4825E+03	3.3400E+03	3.1950E+03	3.0518E+03	2.9131E+03	2.7806E+03
	−3.0E+06	3.3346E+03	3.2720E+03	3.1919E+03	3.0973E+03	2.9925E+03	2.8819E+03	2.7695E+03	2.6581E+03
	−4.0E+06	2.8241E+03	2.8066E+03	2.7797E+03	2.7412E+03	2.6902E+03	2.6276E+03	2.5558E+03	2.4778E+03
	−5.0E+06	2.3270E+03	2.3270E+03	2.3270E+03	2.3270E+03	2.3245E+03	2.3039E+03	2.2749E+03	2.2371E+03
	−6.0E+06	1.6746E+03	1.6736E+03	1.6734E+03	1.6732E+03	1.6731E+03	1.6728E+03	1.6722E+03	1.6713E+03
	−7.0E+06	1.1582E+03	1.0962E+03	1.0420E+03	1.0003E+03	9.7828E+02	9.7295E+02	9.7228E+02	9.7221E+02
15%	−1.0E+06	4.1724E+03	3.9876E+03	3.7964E+03	3.6069E+03	3.4240E+03	3.2505E+03	3.0873E+03	2.9347E+03
	−2.0E+06	3.8700E+03	3.7376E+03	3.5909E+03	3.4371E+03	3.2822E+03	3.1305E+03	2.9843E+03	2.8453E+03
	−3.0E+06	3.4942E+03	3.4174E+03	3.3224E+03	3.2134E+03	3.0954E+03	2.9733E+03	2.8508E+03	2.7306E+03
	−4.0E+06	3.0248E+03	2.9964E+03	2.9550E+03	2.8993E+03	2.8302E+03	2.7502E+03	2.6626E+03	2.5709E+03
	−5.0E+06	2.4655E+03	2.4612E+03	2.4540E+03	2.4421E+03	2.4236E+03	2.3966E+03	2.3599E+03	2.3270E+03
	−6.0E+06	2.0179E+03	2.0172E+03	2.0165E+03	2.0151E+03	2.0127E+03	2.0086E+03	2.0018E+03	1.9910E+03
	−7.0E+06	1.3684E+03	1.3286E+03	1.3177E+03	1.3163E+03	1.3161E+03	1.3161E+03	1.3161E+03	1.3161E+03
20%	−1.0E+06	4.2563E+03	4.0610E+03	3.8614E+03	3.6655E+03	3.4779E+03	3.3009E+03	3.1353E+03	2.9809E+03
	−2.0E+06	3.9703E+03	3.8258E+03	3.6688E+03	3.5068E+03	3.3456E+03	3.1889E+03	3.0390E+03	2.8968E+03
	−3.0E+06	3.6233E+03	3.5316E+03	3.4229E+03	3.3019E+03	3.1742E+03	3.0442E+03	2.9154E+03	2.7898E+03
	−4.0E+06	3.1993E+03	3.1570E+03	3.0993E+03	3.0268E+03	2.9417E+03	2.8477E+03	2.7483E+03	2.6466E+03
	−5.0E+06	2.6870E+03	2.6773E+03	2.6614E+03	2.6371E+03	2.6024E+03	2.5564E+03	2.5001E+03	2.4353E+03
	−6.0E+06	2.3270E+03	2.3270E+03	2.3270E+03	2.3270E+03	2.3269E+03	2.3070E+03	2.2787E+03	2.2415E+03
	−7.0E+06	1.6792E+03	1.6724E+03	1.6715E+03	1.6714E+03	1.6712E+03	1.6709E+03	1.6703E+03	1.6694E+03
25%	−1.0E+06	4.2786E+03	4.0799E+03	3.8788E+03	3.6826E+03	3.4953E+03	3.3189E+03	3.1541E+03	3.0007E+03
	−2.0E+06	4.0017E+03	3.8510E+03	3.6906E+03	3.5270E+03	3.3654E+03	3.2088E+03	3.0594E+03	2.9179E+03
	−3.0E+06	3.6729E+03	3.5703E+03	3.4544E+03	3.3291E+03	3.1990E+03	3.0678E+03	2.9385E+03	2.8130E+03
	−4.0E+06	3.2875E+03	3.2283E+03	3.1569E+03	3.0740E+03	2.9817E+03	2.8829E+03	2.7804E+03	2.6768E+03
	−5.0E+06	2.8432E+03	2.8174E+03	2.7842E+03	2.7426E+03	2.6919E+03	2.6322E+03	2.5649E+03	2.4916E+03
	−6.0E+06	2.3324E+03	2.3270E+03	2.3270E+03	2.3270E+03	2.3270E+03	2.3270E+03	2.3270E+03	2.3270E+03
	−7.0E+06	2.3270E+03	2.3270E+03	2.3215E+03	2.3096E+03	2.2928E+03	2.2705E+03	2.2420E+03	2.2069E+03

Table 10 Mean Molecular Weight, g/mol

Al fraction	Internal energy (J/kg)	Density (kg/m³) 31.6000	10.0000	3.1600	1.0000	0.3160	0.1000	0.0316	0.0100
0%	−1.0E+06	2.3781E+01	2.3506E+01	2.3225E+01	2.2947E+01	2.2680E+01	2.2427E+01	2.2191E+01	2.1972E+01
	−2.0E+06	2.4305E+01	2.4126E+01	2.3923E+01	2.3706E+01	2.3484E+01	2.3264E+01	2.3052E+01	2.2850E+01
	−3.0E+06	2.4636E+01	2.4567E+01	2.4473E+01	2.4354E+01	2.4213E+01	2.4057E+01	2.3893E+01	2.3728E+01
	−4.0E+06	2.4740E+01	2.4732E+01	2.4719E+01	2.4699E+01	2.4667E+01	2.4620E+01	2.4556E+01	2.4475E+01
	−5.0E+06	2.4752E+01	2.4750E+01	2.4749E+01	2.4748E+01	2.4748E+01	2.4747E+01	2.4746E+01	2.4744E+01
	−6.0E+06	2.5724E+01	2.5308E+01	2.4980E+01	2.4801E+01	2.4756E+01	2.4750E+01	2.4749E+01	2.4749E+01
	−7.0E+06	2.8555E+01	2.8505E+01	2.8431E+01	2.8329E+01	2.8199E+01	2.8045E+01	2.7868E+01	2.7681E+01
5%	−1.0E+06	2.4861E+01	2.4525E+01	2.4185E+01	2.3851E+01	2.3531E+01	2.3230E+01	2.2949E+01	2.2689E+01
	−2.0E+06	2.5450E+01	2.5215E+01	2.4956E+01	2.4683E+01	2.4408E+01	2.4138E+01	2.3879E+01	2.3634E+01
	−3.0E+06	2.5856E+01	2.5745E+01	2.5601E+01	2.5428E+01	2.5232E+01	2.5024E+01	2.4811E+01	2.4599E+01
	−4.0E+06	2.6026E+01	2.6003E+01	2.5968E+01	2.5917E+01	2.5843E+01	2.5746E+01	2.5627E+01	2.5491E+01
	−5.0E+06	2.6053E+01	2.6050E+01	2.6047E+01	2.6044E+01	2.6038E+01	2.6028E+01	2.6011E+01	2.5986E+01
	−6.0E+06	2.6185E+01	2.6071E+01	2.6054E+01	2.6052E+01	2.6052E+01	2.6052E+01	2.6052E+01	2.6051E+01
	−7.0E+06	2.9460E+01	2.8989E+01	2.8519E+01	2.8065E+01	2.7635E+01	2.7237E+01	2.6875E+01	2.6556E+01
10%	−1.0E+06	2.6043E+01	2.5632E+01	2.5219E+01	2.4818E+01	2.4436E+01	2.4079E+01	2.3746E+01	2.3439E+01
	−2.0E+06	2.6700E+01	2.6400E+01	2.6072E+01	2.5732E+01	2.5393E+01	2.5064E+01	2.4751E+01	2.4457E+01
	−3.0E+06	2.7186E+01	2.7021E+01	2.6816E+01	2.6578E+01	2.6318E+01	2.6048E+01	2.5778E+01	2.5514E+01
	−4.0E+06	2.7435E+01	2.7386E+01	2.7314E+01	2.7213E+01	2.7080E+01	2.6919E+01	2.6736E+01	2.6540E+01
	−5.0E+06	2.7495E+01	2.7485E+01	2.7472E+01	2.7451E+01	2.7414E+01	2.7363E+01	2.7291E+01	2.7199E+01
	−6.0E+06	2.7514E+01	2.7502E+01	2.7499E+01	2.7499E+01	2.7498E+01	2.7497E+01	2.7496E+01	2.7493E+01
	−7.0E+06	2.9471E+01	2.8790E+01	2.8215E+01	2.7785E+01	2.7560E+01	2.7506E+01	2.7500E+01	2.7499E+01
15%	−1.0E+06	2.7322E+01	2.6826E+01	2.6334E+01	2.5861E+01	2.5415E+01	2.4998E+01	2.4610E+01	2.4251E+01
	−2.0E+06	2.8064E+01	2.7683E+01	2.7277E+01	2.6862E+01	2.6454E+01	2.6060E+01	2.5687E+01	2.5338E+01
	−3.0E+06	2.8642E+01	2.8408E+01	2.8128E+01	2.7814E+01	2.7480E+01	2.7141E+01	2.6806E+01	2.6483E+01
	−4.0E+06	2.8986E+01	2.8893E+01	2.8765E+01	2.8596E+01	2.8390E+01	2.8154E+01	2.7899E+01	2.7636E+01
	−5.0E+06	2.9106E+01	2.9088E+01	2.9064E+01	2.9026E+01	2.8969E+01	2.8886E+01	2.8774E+01	2.8603E+01
	−6.0E+06	2.9124E+01	2.9116E+01	2.9112E+01	2.9108E+01	2.9101E+01	2.9089E+01	2.9070E+01	2.9040E+01
	−7.0E+06	2.9715E+01	2.9258E+01	2.9136E+01	2.9119E+01	2.9117E+01	2.9116E+01	2.9116E+01	2.9116E+01
20%	−1.0E+06	2.8683E+01	2.8098E+01	2.7531E+01	2.6991E+01	2.6486E+01	2.6013E+01	2.5573E+01	2.5164E+01
	−2.0E+06	2.9530E+01	2.9060E+01	2.8571E+01	2.8083E+01	2.7608E+01	2.7152E+01	2.6720E+01	2.6313E+01
	−3.0E+06	3.0224E+01	2.9903E+01	2.9538E+01	2.9144E+01	2.8735E+01	2.8325E+01	2.7923E+01	2.7537E+01
	−4.0E+06	3.0693E+01	3.0534E+01	3.0328E+01	3.0076E+01	2.9785E+01	2.9468E+01	2.9137E+01	2.8802E+01
	−5.0E+06	3.0903E+01	3.0858E+01	3.0797E+01	3.0708E+01	3.0584E+01	3.0421E+01	3.0223E+01	2.9998E+01
	−6.0E+06	3.0941E+01	3.0923E+01	3.0905E+01	3.0878E+01	3.0832E+01	3.0768E+01	3.0679E+01	3.0562E+01
	−7.0E+06	3.1048E+01	3.0951E+01	3.0938E+01	3.0936E+01	3.0935E+01	3.0934E+01	3.0932E+01	3.0929E+01
25%	−1.0E+06	3.0074E+01	2.9422E+01	2.8798E+01	2.8212E+01	2.7663E+01	2.7150E+01	2.6672E+01	2.6225E+01
	−2.0E+06	3.1031E+01	3.0486E+01	2.9937E+01	2.9396E+01	2.8874E+01	2.8374E+01	2.7899E+01	2.7450E+01
	−3.0E+06	3.1858E+01	3.1450E+01	3.1014E+01	3.0560E+01	3.0098E+01	2.9640E+01	2.9192E+01	2.8759E+01
	−4.0E+06	3.2506E+01	3.2241E+01	3.1948E+01	3.1621E+01	3.1267E+01	3.0892E+01	3.0508E+01	3.0122E+01
	−5.0E+06	3.2939E+01	3.2791E+01	3.2635E+01	3.2457E+01	3.2249E+01	3.2009E+01	3.1742E+01	3.1451E+01
	−6.0E+06	3.3149E+01	3.3058E+01	3.2994E+01	3.2924E+01	3.2833E+01	3.2705E+01	3.2511E+01	3.2202E+01
	−7.0E+06	3.3150E+01	3.3058E+01	3.2996E+01	3.2934E+01	3.2862E+01	3.2778E+01	3.2677E+01	3.2553E+01

Table 11 Specific Heat Ratio

Al fraction	Internal energy (J/kg)	Density (kg/m³) 31.6000	10.0000	3.1600	1.0000	0.3160	0.1000	0.0316	0.0100
0%	−1.0E+06	1.1621E+00	1.1535E+00	1.1450E+00	1.1370E+00	1.1294E+00	1.1223E+00	1.1157E+00	1.1096E+00
	−2.0E+06	1.1728E+00	1.1621E+00	1.1516E+00	1.1419E+00	1.1331E+00	1.1251E+00	1.1179E+00	1.1113E+00
	−3.0E+06	1.1969E+00	1.1870E+00	1.1752E+00	1.1625E+00	1.1501E+00	1.1389E+00	1.1289E+00	1.1203E+00
	−4.0E+06	1.2209E+00	1.2184E+00	1.2142E+00	1.2078E+00	1.1986E+00	1.1866E+00	1.1729E+00	1.1586E+00
	−5.0E+06	1.2345E+00	1.2346E+00	1.2345E+00	1.2343E+00	1.2339E+00	1.2333E+00	1.2323E+00	1.2304E+00
	−6.0E+06	1.1823E+00	1.1841E+00	1.1956E+00	1.2188E+00	1.2312E+00	1.2332E+00	1.2334E+00	1.2334E+00
	−7.0E+06	1.2603E+00	1.2518E+00	1.2405E+00	1.2270E+00	1.2125E+00	1.1908E+00	1.1780E+00	1.1664E+00
5%	−1.0E+06	1.1541E+00	1.1463E+00	1.1386E+00	1.1313E+00	1.1244E+00	1.1181E+00	1.1123E+00	1.1070E+00
	−2.0E+06	1.1612E+00	1.1523E+00	1.1435E+00	1.1352E+00	1.1275E+00	1.1205E+00	1.1142E+00	1.1084E+00
	−3.0E+06	1.1776E+00	1.1688E+00	1.1586E+00	1.1482E+00	1.1383E+00	1.1293E+00	1.1212E+00	1.1141E+00
	−4.0E+06	1.1980E+00	1.1941E+00	1.1881E+00	1.1798E+00	1.1693E+00	1.1577E+00	1.1459E+00	1.1348E+00
	−5.0E+06	1.2174E+00	1.2171E+00	1.2163E+00	1.2149E+00	1.2124E+00	1.2085E+00	1.2023E+00	1.1935E+00
	−6.0E+06	1.2134E+00	1.2232E+00	1.2251E+00	1.2253E+00	1.2253E+00	1.2253E+00	1.2253E+00	1.2252E+00
	−7.0E+06	1.1648E+00	1.1588E+00	1.1534E+00	1.1486E+00	1.1448E+00	1.1424E+00	1.1422E+00	1.1458E+00
10%	−1.0E+06	1.1482E+00	1.1414E+00	1.1344E+00	1.1276E+00	1.1213E+00	1.1155E+00	1.1102E+00	1.1054E+00
	−2.0E+06	1.1522E+00	1.1450E+00	1.1375E+00	1.1303E+00	1.1235E+00	1.1173E+00	1.1117E+00	1.1065E+00
	−3.0E+06	1.1625E+00	1.1550E+00	1.1467E+00	1.1383E+00	1.1303E+00	1.1228E+00	1.1161E+00	1.1101E+00
	−4.0E+06	1.1778E+00	1.1732E+00	1.1666E+00	1.1582E+00	1.1488E+00	1.1391E+00	1.1299E+00	1.1215E+00
	−5.0E+06	9.9970E−01	9.9970E−01	9.9950E−01	9.9910E−01	1.1848E+00	1.1759E+00	1.1651E+00	1.1534E+00
	−6.0E+06	1.2112E+00	1.2116E+00	1.2116E+00	1.2114E+00	1.2112E+00	1.2108E+00	1.2100E+00	1.2087E+00
	−7.0E+06	1.1622E+00	1.1612E+00	1.1633E+00	1.1737E+00	1.1938E+00	1.2039E+00	1.2054E+00	1.2056E+00
15%	−1.0E+06	1.1417E+00	1.1356E+00	1.1292E+00	1.1228E+00	1.1169E+00	1.1115E+00	1.1067E+00	1.1025E+00
	−2.0E+06	1.1433E+00	1.1373E+00	1.1310E+00	1.1247E+00	1.1188E+00	1.1133E+00	1.1084E+00	1.1039E+00
	−3.0E+06	1.1489E+00	1.1430E+00	1.1364E+00	1.1296E+00	1.1231E+00	1.1171E+00	1.1116E+00	1.1065E+00
	−4.0E+06	1.1597E+00	1.1550E+00	1.1489E+00	1.1417E+00	1.1340E+00	1.1265E+00	1.1195E+00	1.1131E+00
	−5.0E+06	1.1709E+00	1.1695E+00	1.1670E+00	1.1629E+00	1.1572E+00	1.1497E+00	1.1412E+00	9.9130E−01
	−6.0E+06	1.1954E+00	1.1953E+00	1.1948E+00	1.1937E+00	1.1919E+00	1.1889E+00	1.1841E+00	1.1772E+00
	−7.0E+06	1.1835E+00	1.1955E+00	1.2025E+00	1.2037E+00	1.2038E+00	1.2038E+00	1.2038E+00	1.2038E+00
20%	−1.0E+06	1.1351E+00	1.1297E+00	1.1237E+00	1.1177E+00	1.1120E+00	1.1067E+00	1.1021E+00	1.0980E+00
	−2.0E+06	1.1345E+00	1.1296E+00	1.1241E+00	1.1185E+00	1.1131E+00	1.1081E+00	1.1036E+00	1.0996E+00
	−3.0E+06	1.1360E+00	1.1315E+00	1.1262E+00	1.1208E+00	1.1155E+00	1.1105E+00	1.1059E+00	1.1018E+00
	−4.0E+06	1.1419E+00	1.1378E+00	1.1327E+00	1.1270E+00	1.1212E+00	1.1156E+00	1.1105E+00	1.1057E+00
	−5.0E+06	1.1522E+00	1.1502E+00	1.1469E+00	1.1421E+00	1.1361E+00	1.1293E+00	1.1224E+00	1.1158E+00
	−6.0E+06	9.9940E−01	9.9960E−01	9.9940E−01	9.9900E−01	1.1660E+00	1.1590E+00	1.1504E+00	1.1411E+00
	−7.0E+06	1.1880E+00	1.1897E+00	1.1899E+00	1.1898E+00	1.1896E+00	1.1893E+00	1.1886E+00	1.1875E+00
25%	−1.0E+06	1.1299E+00	1.1253E+00	1.1198E+00	1.1141E+00	1.1086E+00	1.1035E+00	1.0989E+00	1.0948E+00
	−2.0E+06	1.1281E+00	1.1241E+00	1.1192E+00	1.1141E+00	1.1091E+00	1.1043E+00	1.1000E+00	1.0961E+00
	−3.0E+06	1.1272E+00	1.1238E+00	1.1195E+00	1.1149E+00	1.1102E+00	1.1057E+00	1.1015E+00	1.0976E+00
	−4.0E+06	1.1273E+00	1.1245E+00	1.1208E+00	1.1165E+00	1.1120E+00	1.1076E+00	1.1033E+00	1.0993E+00
	−5.0E+06	1.1301E+00	1.1279E+00	1.1248E+00	1.1209E+00	1.1166E+00	1.1119E+00	1.1072E+00	1.1027E+00
	−6.0E+06	1.1376E+00	9.9820E−01	9.9830E−01	9.9790E−01	9.9720E−01	9.9590E−01	9.9360E−01	9.8950E−01
	−7.0E+06	9.9630E−01	9.9820E−01	1.1502E+00	1.1463E+00	1.1415E+00	1.1359E+00	1.1298E+00	1.1232E+00

Table 12 Molar Fraction of Oxidizing Species

Al fraction	Internal energy (J/kg)	Density (kg/m³) 31.6000	10.0000	3.1600	1.0000	0.3160	0.1000	0.0316	0.0100
0%	−1.0E+06	0.433630	0.426820	0.419970	0.413320	0.407020	0.401180	0.395810	0.390880
	−2.0E+06	0.448430	0.444040	0.439050	0.433750	0.428380	0.423140	0.418130	0.413440
	−3.0E+06	0.456940	0.455420	0.453320	0.450600	0.447350	0.443750	0.439960	0.436130
	−4.0E+06	0.459250	0.459100	0.458850	0.458450	0.457820	0.456870	0.455570	0.453920
	−5.0E+06	0.459500	0.459440	0.459430	0.459420	0.459400	0.459400	0.459380	0.459330
	−6.0E+06	0.497000	0.480970	0.468330	0.461410	0.459680	0.459450	0.459430	0.459430
	−7.0E+06	0.606880	0.604970	0.602120	0.598180	0.593150	0.587140	0.579890	0.572290
5%	−1.0E+06	0.360100	0.354100	0.348050	0.342020	0.336140	0.330470	0.325070	0.320050
	−2.0E+06	0.369490	0.365270	0.360630	0.355750	0.350780	0.345860	0.341100	0.336590
	−3.0E+06	0.375580	0.373650	0.371220	0.368290	0.364970	0.361380	0.357680	0.353980
	−4.0E+06	0.377750	0.377330	0.376770	0.375970	0.374850	0.373350	0.371500	0.369360
	−5.0E+06	0.377960	0.377890	0.377850	0.377790	0.377700	0.377550	0.377320	0.376940
	−6.0E+06	0.382100	0.378480	0.377970	0.377900	0.377890	0.377890	0.377890	0.377890
	−7.0E+06	0.489440	0.474120	0.458800	0.443960	0.429900	0.416840	0.404960	0.394480
10%	−1.0E+06	0.282650	0.278040	0.273230	0.268170	0.262980	0.257730	0.252540	0.247570
	−2.0E+06	0.287000	0.283510	0.279670	0.275540	0.271210	0.266800	0.262430	0.258230
	−3.0E+06	0.290140	0.288230	0.285910	0.283200	0.280140	0.276860	0.273490	0.270130
	−4.0E+06	0.291570	0.290940	0.290140	0.289050	0.287640	0.285880	0.283860	0.281660
	−5.0E+06	0.291830	0.291650	0.291480	0.291250	0.290860	0.290340	0.289590	0.288620
	−6.0E+06	0.292000	0.291730	0.291700	0.291690	0.291680	0.291670	0.291660	0.291630
	−7.0E+06	0.345240	0.326810	0.311190	0.299480	0.293360	0.291890	0.291710	0.291690
15%	−1.0E+06	0.206950	0.204560	0.201570	0.197850	0.193430	0.188500	0.183230	0.177880
	−2.0E+06	0.204500	0.202500	0.200060	0.197090	0.193560	0.189640	0.185470	0.181230
	−3.0E+06	0.202440	0.201100	0.199480	0.197490	0.195080	0.192300	0.189300	0.186200
	−4.0E+06	0.201140	0.200470	0.199680	0.198690	0.197410	0.195840	0.194020	0.192050
	−5.0E+06	0.200720	0.200480	0.200250	0.199990	0.199630	0.199120	0.198420	0.197340
	−6.0E+06	0.200570	0.200450	0.200400	0.200370	0.200320	0.200250	0.200120	0.199920
	−7.0E+06	0.213450	0.203460	0.200800	0.200450	0.200410	0.200400	0.200400	0.200400
20%	−1.0E+06	0.138300	0.138810	0.138080	0.135980	0.132570	0.128040	0.122670	0.116700
	−2.0E+06	0.127790	0.128280	0.127930	0.126540	0.124030	0.120530	0.116260	0.111450
	−3.0E+06	0.117500	0.117830	0.117870	0.117240	0.115800	0.113560	0.110640	0.107250
	−4.0E+06	0.189750	0.109030	0.109040	0.108940	0.108440	0.107480	0.105990	0.104140
	−5.0E+06	0.105080	0.104660	0.104420	0.104260	0.104080	0.103800	0.103330	0.102660
	−6.0E+06	0.104250	0.103950	0.103780	0.103660	0.103540	0.103360	0.103140	0.102820
	−7.0E+06	0.105410	0.103810	0.103620	0.103590	0.103580	0.103570	0.103570	0.103550
25%	−1.0E+06	0.083040	0.086010	0.087270	0.086740	0.084540	0.080930	0.076170	0.070560
	−2.0E+06	0.067230	0.070140	0.071810	0.072010	0.070710	0.068090	0.064330	0.059700
	−3.0E+06	0.050870	0.053450	0.055420	0.056370	0.056120	0.054680	0.052170	0.048780
	−4.0E+06	0.034580	0.036230	0.038030	0.039500	0.040260	0.040130	0.039090	0.037220
	−5.0E+06	0.020440	0.020370	0.021070	0.022170	0.023310	0.024160	0.024510	0.024240
	−6.0E+06	0.011730	0.009930	0.009090	0.008960	0.009550	0.010810	0.012700	0.015170
	−7.0E+06	0.011670	0.009930	0.008980	0.008560	0.008570	0.008870	0.009280	0.009600

Table 13 Mass Fraction of Alumina Smoke

Al fraction	Internal energy (J/kg)	Density (kg/m³)							
		31.6000	10.0000	3.1600	1.0000	0.3160	0.1000	0.0316	0.0100
0%	−1.0E+06	0.0000000	0.0000000	0.0000000	0.0000000	0.0000000	0.0000000	0.0000000	0.0000000
	−2.0E+06	0.0000000	0.0000000	0.0000000	0.0000000	0.0000000	0.0000000	0.0000000	0.0000000
	−3.0E+06	0.0000000	0.0000000	0.0000000	0.0000000	0.0000000	0.0000000	0.0000000	0.0000000
	−4.0E+06	0.0000000	0.0000000	0.0000000	0.0000000	0.0000000	0.0000000	0.0000000	0.0000000
	−5.0E+06	0.0000000	0.0000000	0.0000000	0.0000000	0.0000000	0.0000000	0.0000000	0.0000000
	−6.0E+06	0.0000000	0.0000000	0.0000000	0.0000000	0.0000000	0.0000000	0.0000000	0.0000000
	−7.0E+06	0.0000000	0.0000000	0.0000000	0.0000000	0.0000000	0.0000000	0.0000000	0.0000000
5%	−1.0E+06	0.0815640	0.0803096	0.0795528	0.0795394	0.0802201	0.0815262	0.0832609	0.0851474
	−2.0E+06	0.0887893	0.0881362	0.0876069	0.0873592	0.0874322	0.0878798	0.0885687	0.0894408
	−3.0E+06	0.0927932	0.0926613	0.0924212	0.0921697	0.0920422	0.0919979	0.0921023	0.0923318
	−4.0E+06	0.0941603	0.0942048	0.0942433	0.0941866	0.0941581	0.0940840	0.0940198	0.0939734
	−5.0E+06	0.0944341	0.0944437	0.0944489	0.0944663	0.0944838	0.0944794	0.0944592	0.0944709
	−6.0E+06	0.0944842	0.0944846	0.0944655	0.0944757	0.0944748	0.0944748	0.0944747	0.0944771
	−7.0E+06	0.0944693	0.0944823	0.0944594	0.0944567	0.0944854	0.0944878	0.0944857	0.0944562
10%	−1.0E+06	0.1669239	0.1644067	0.1628466	0.1625512	0.1636037	0.1657950	0.1687377	0.1721079
	−2.0E+06	0.1783634	0.1769719	0.1758951	0.1753610	0.1755521	0.1764360	0.1778242	0.1795061
	−3.0E+06	0.1853021	0.1848600	0.1842610	0.1837947	0.1835350	0.1836207	0.1839593	0.1845509
	−4.0E+06	0.1881810	0.1882167	0.1881373	0.1880017	0.1878147	0.1876777	0.1876291	0.1876488
	−5.0E+06	0.1887765	0.1888178	0.1888543	0.1888379	0.1888413	0.1888279	0.1887906	0.1887748
	−6.0E+06	0.1889446	0.1889436	0.1889494	0.1889563	0.1889588	0.1889331	0.1889365	0.1889520
	−7.0E+06	0.1889623	0.1889503	0.1889564	0.1889536	0.1889436	0.1889463	0.1889490	0.1889523
15%	−1.0E+06	0.2443908	0.2396603	0.2365902	0.2357051	0.2370769	0.2404176	0.2452804	0.2509830
	−2.0E+06	0.2624549	0.2596231	0.2574208	0.2563426	0.2566608	0.2582614	0.2608792	0.2642018
	−3.0E+06	0.2748780	0.2736349	0.2723565	0.2713534	0.2710179	0.2712961	0.2722409	0.2736572
	−4.0E+06	0.2811718	0.2810717	0.2807051	0.2802438	0.2798591	0.2796073	0.2796169	0.2798425
	−5.0E+06	0.2829802	0.2831141	0.2831443	0.2831365	0.2831174	0.2830236	0.2829707	0.2828378
	−6.0E+06	0.2833468	0.2833760	0.2834059	0.2834010	0.2834035	0.2834190	0.2834081	0.2834162
	−7.0E+06	0.2834134	0.2834160	0.2834207	0.2834188	0.2834323	0.2834086	0.2834086	0.2834116
20%	−1.0E+06	0.3068633	0.2989880	0.2938237	0.2918613	0.2931441	0.2973484	0.3039959	0.3123535
	−2.0E+06	0.3336552	0.3282159	0.3240845	0.3219559	0.3221008	0.3245135	0.3287528	0.3344831
	−3.0E+06	0.3550789	0.3519733	0.3490672	0.3470702	0.3463821	0.3471307	0.3492109	0.3523820
	−4.0E+06	0.3828471	0.3687377	0.3674375	0.3660667	0.3650721	0.3647060	0.3650965	0.3660938
	−5.0E+06	0.3760272	0.3762611	0.3762223	0.3759943	0.3756520	0.3752726	0.3749933	0.3748755
	−6.0E+06	0.3772222	0.3774234	0.3775533	0.3775660	0.3775248	0.3774778	0.3773894	0.3773382
	−7.0E+06	0.3778619	0.3778664	0.3778783	0.3778896	0.3778940	0.3779053	0.3778907	0.3778895
25%	−1.0E+06	0.3459817	0.3355685	0.3286139	0.3254889	0.3261712	0.3303349	0.3373291	0.3464701
	−2.0E+06	0.3789724	0.3709955	0.3649806	0.3616469	0.3611772	0.3635097	0.3681826	0.3748228
	−3.0E+06	0.4072526	0.4016956	0.3969278	0.3936475	0.3922605	0.3928793	0.3954439	0.3996365
	−4.0E+06	0.4309372	0.4278045	0.4245827	0.4217109	0.4197527	0.4190580	0.4196736	0.4215833
	−5.0E+06	0.4493364	0.4488107	0.4475874	0.4459167	0.4441661	0.4427394	0.4419403	0.4419114
	−6.0E+06	0.4606100	0.4617778	0.4624970	0.4625247	0.4617581	0.4601235	0.4576789	0.4543551
	−7.0E+06	0.4607168	0.4617587	0.4626203	0.4630053	0.4629408	0.4625030	0.4619522	0.4615025

(a) Fixed-particle-diameter model: The particle diameter at the burning surface is fixed to 150 μm. It is assumed that a portion of particle is alumina in the initial state and this portion finally remains after the combustion. In the numerical simulation, combustion of a particle ends at the moment when combustion of the aluminum portion completes, and after that moment, the particle path is calculated with a fixed particle diameter. A setup of the initial amount of alumina will be described later.

(b) Mono-modal model: This is a model in which no small particle at a burning surface is generated and all particles are agglomerate droplets leaving from the burning surface and starting the combustion. Suppose that a particle diameter distribution follows a log-normal distribution, probability density function for the particle diameter can be written by the following formulae.

$$f(D)=\frac{\log_{10}e}{\sqrt{2\pi}D}\left[\frac{\exp\left(-z^2/2\right)}{\sigma}\right],\qquad z=\frac{1}{\sigma}\log_{10}\left(\frac{D}{D_m}\right) \tag{224}$$

The cumulative distribution function is

$$F(D)=\int_0^D f(D)dD=\frac{1}{2}\left[1+erf\left(\frac{z}{\sqrt{2}}\right)\right] \tag{225}$$

According to Ref.[38], the variance σ obtained in experiments is roughly 0.2 and this value is adopted here. The mass-averaged diameter D_m is set to 150 μm. The probability density function and the cumulative distribution function for this case are shown in Fig. 104 and Fig. 105, respectively.

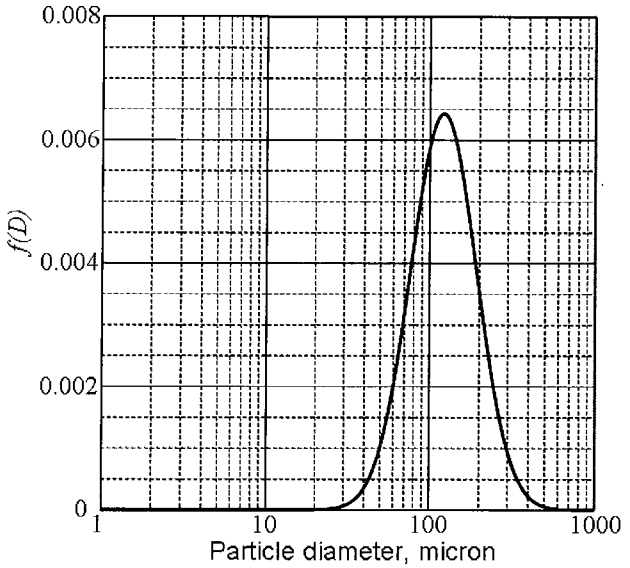

Fig. 104 Probability density function for particle diameter, mono-modal model

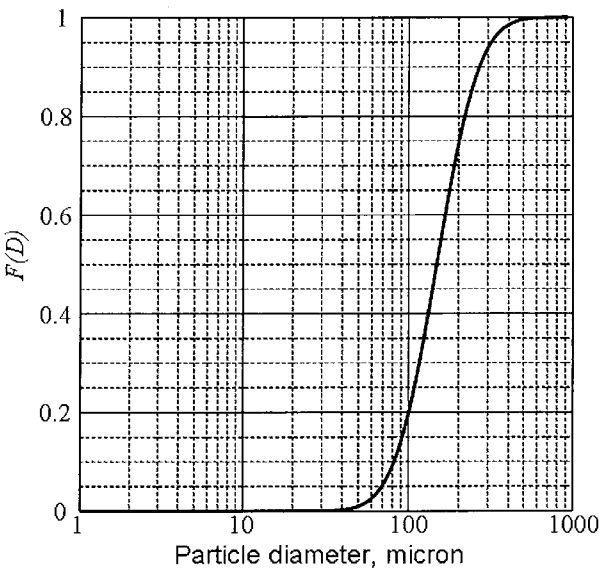

Fig. 105 Cumulative distribution function for particle diameter, mono-modal model

(c) Bi-modal model: According to experiments, the particle diameter distribution at a burning surface is bi-modal like. A bi-modal distribution can be made by superimposing two kinds of mono-modal, log-normal, distributions shown previously.

$$f(D)=\frac{\log_{10}e}{\sqrt{2\pi}D}\left[\frac{\exp\left(-z_1^2/2\right)}{\sigma_1}(1-f_0)+\frac{\exp\left(-z_2^2/2\right)}{\sigma_2}f_0\right] \tag{226}$$

$$z_1=\frac{1}{\sigma_1}\log_{10}\left(\frac{D}{D_{m1}}\right),\qquad z_2=\frac{1}{\sigma_2}\log_{10}\left(\frac{D}{D_{m2}}\right) \tag{227}$$

$$F(D)=\int_0^D f(D)dD=\frac{1}{2}\left[\left(1+erf\left(\frac{z_1}{\sqrt{2}}\right)\right)(1-f_0)+\left(1+erf\left(\frac{z_2}{\sqrt{2}}\right)\right)f_0\right] \tag{228}$$

According to Ref.[38], the mass-averaged diameter of small particles is 1.5 μm and the variance is 0.4 irrespective of propellant and the state of combustion. Taking account of this, coefficients are set as follows.

$$z_1 = 1.5\,\mu\mathrm{m}, \qquad \sigma_1 = 0.4$$
$$z_2 = 150\,\mu\mathrm{m}, \qquad \sigma_2 = 0.2$$

On the other hand f_0 changes significantly with the state of combustion and the kind of propellants. Here, tentatively, f_0 is set to 0.8 and it is assumed that larger particles are generated more than the smaller particles. Only large particles are considered to burn and particles of the small-diameter group are considered to be already burned out. The probability density function and the cumulative distribution function for this case are shown in Fig. 106 and Fig. 107, respectively.

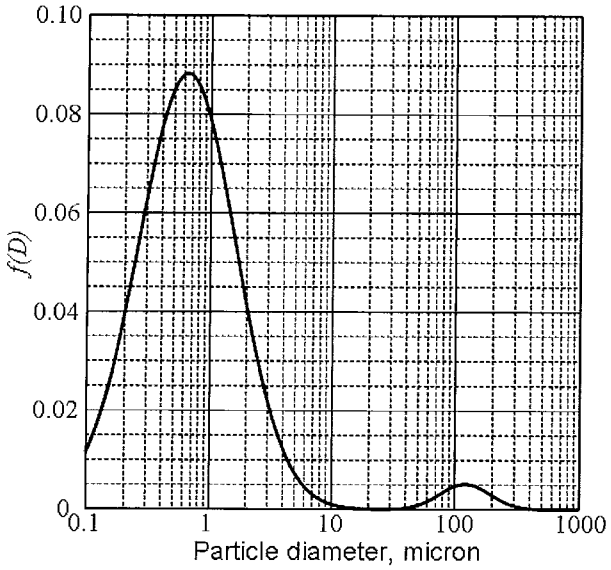

Fig. 106 Probability density function for particle diameter, bi-modal model

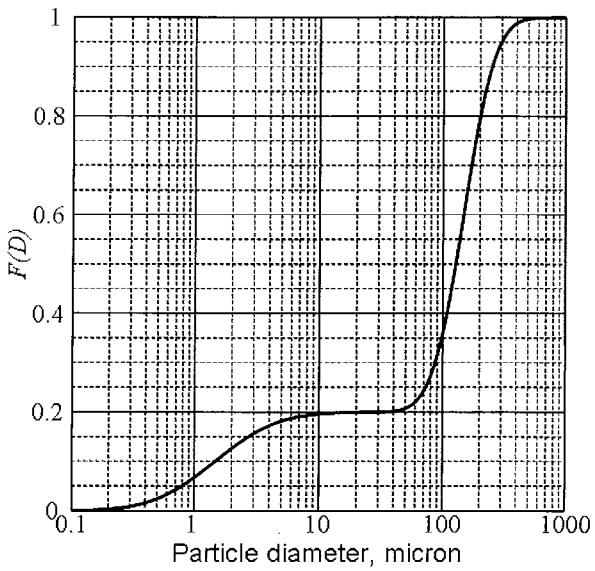

Fig. 107 Cumulative distribution function for particle diameter, bi-modal model

3.3.6. Initial amount of alumina in a particle

Let us denote the ratio of aluminum mass in the alumina cap which finally remains after the combustion to all the aluminum mass in the propellant by ψ, and the mass fraction of alumina in the initial large droplet by β. The bi-modal model is assumed as the particle diameter distribution and all small particle groups are assumed to be alumina particles. For the mono-modal model or the fixed-diameter model, it is necessary to set f_0=1.0 in the following equations. Denoting the propellant mass by M_{prop} and the total mass of the particle by M_p, since the quantity of the aluminum in a generated particle is equal to that of the aluminum contained originally in the propellant, the following relationship holds.

$$M_{prop} \cdot \alpha = M_p(1-f_0)\frac{27}{51} + M_p f_0\left((1-\beta)+\frac{27}{51}\beta\right) \tag{229}$$

The first term in the right-hand side is the amount of aluminum in small particles, and the second term is the amount of aluminum in large particles. The quantity of 27/51 represents the mass fraction of aluminum in alumina. The aluminum mass fraction in the propellant is denoted by α and in this study α=0.2 is considered.

On the other hand, the portion of alumina at the initial state remains as an alumina particle to the end and since the ratio of the aluminum amount in that portion to the total aluminum amount is ψ, the following relationship holds.

$$M_{prop} \cdot \alpha \cdot \psi = M_p(1-f_0)\frac{27}{51} + M_p f_0 \frac{27}{51}\beta \tag{230}$$

By simultaneously solving Eqs. (229) and (230), the relationship between β and ψ is obtained as

$$\beta = \frac{f_0\left(1+\frac{24}{27}\psi\right)-(1-\psi)}{f_0\left(1+\frac{24}{27}\psi\right)}. \tag{231}$$

The relationship between β and ψ is plotted for some values of f_0 in Fig. 108. It turns out from the figure that, if ψ is set to 0.2, β is about 0.15 for the bi-modal model (f_0=0.8) and is about 0.32 for the mono-modal model (f_0=1.0).

The following relationship holds between the volume fraction of alumina in a particle, ϕ and the mass fraction β.

$$\beta = \frac{\phi\sigma_{Al2O3}}{\phi\sigma_{Al2O3}+(1-\phi)\sigma_{Al}} \tag{232}$$

or

$$\phi = \frac{\beta\sigma_{Al}}{(1-\beta)\sigma_{Al2O3}+\beta\sigma_{Al}} \tag{233}$$

The ratio of the final particle diameter at the time of aluminum particle burn-out is summarized in Table 14.

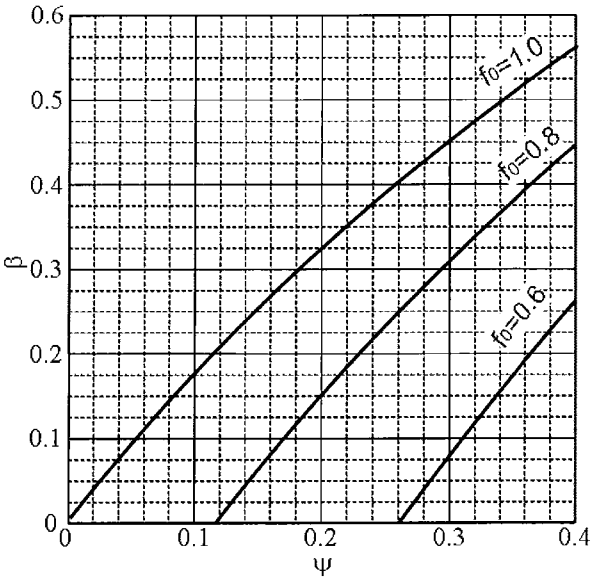

Fig. 108 Relationship between β and ψ

Table 14 Ratio of the final diameter to the initial diameter

Particle diameter distribution	ψ	f_0	β	ϕ	D_{final}/D_0
Fixed/Mono-modal	0.2*	1.0	0.32	0. 34	0. 70
Bi-modal	0.2*	0.8*	0.15	0. 16	0. 54

*tentative values

Therefore, for example, in the fixed-diameter model or the mono-modal model, a particle of the initial diameter of 150 μm is supposed to finish combustion at the time when its diameter reduces to about 105 μm, whereas in the bi-modal model it is 80 μm.

The ratio of total mass of particles to that of the propellant is written from Eq. (230) as

$$\frac{M_p}{M_{prop}} = \frac{51}{27}\frac{\alpha\psi}{(1-f_0)+f_0\beta} \tag{234}$$

The ratio of injecting amounts of mass between the Eulerian phase and the Lagrangian phase is determined by Eq. (234).

4. Numerical Experiments

4.1. Comparison between an Eulerian-Lagrangian method and an Eulerian-Eulerian method

4.1.1. Injection of two-phase jet into two-dimensional nozzle flow[39]

The results are compared between the Eulerian-Lagrangian method and the Eulerian-Eulerian method for a problem of two-dimensional single-phase flow in a Laval nozzle into which a two-phase jet is perpendicularly injected from the side wall downstream the throat as shown in Fig. 109. The conditions of gas and flow properties are summarized in Table 15.

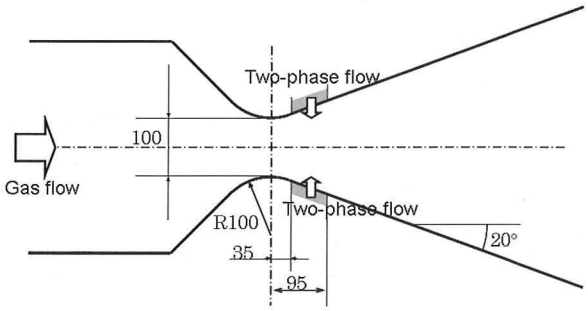

Fig. 109 Injection of two-phase jet into two-dimensional nozzle flow

As for the initial conditions of the nozzle flow, a numerical solution of a phase- equilibrium flow is employed. In the Eulerian-Lagrangian method, the phase-interaction sauce term is calculated by calculating a particle path once in every 40 time-steps, whereas the gaseous phase is calculated by fixing the sauce term for 40 steps. The particle paths of 100 per a cell interface are made to leave from the inlet.

Table 15 Flow conditions

Gas properties	Mean molecular weight, g/mol	28.96
	Specific heat ratio	1.4
Main stream	Chamber pressure, MPa	10
	Chamber temperature, K	1000
Jet	Exit pressure, MPa	2
	Exit temperature, K	1000
	Exit velocity, m/s	1000
	Particle mass fraction, %	35
	Particle diameter, μm	60

The grid system consisting of 101×62 points is shown in Fig. 110.

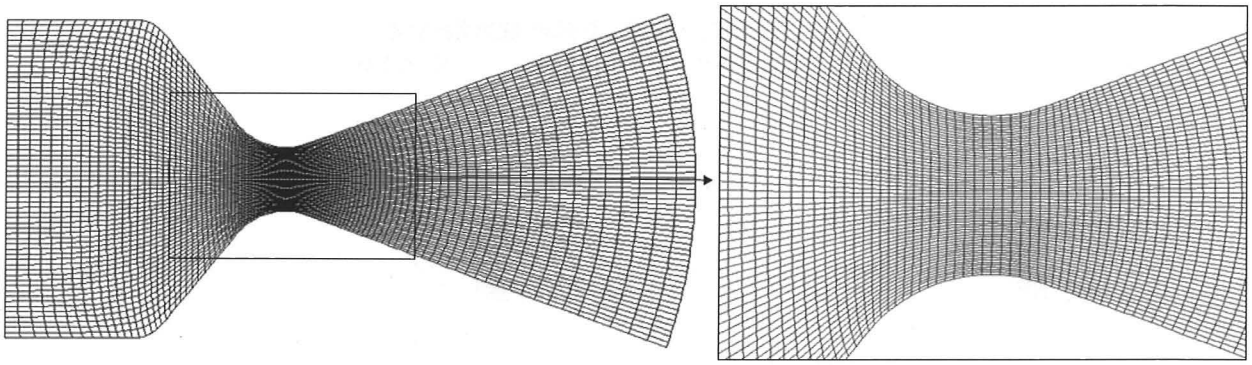

Fig. 110 Grid system

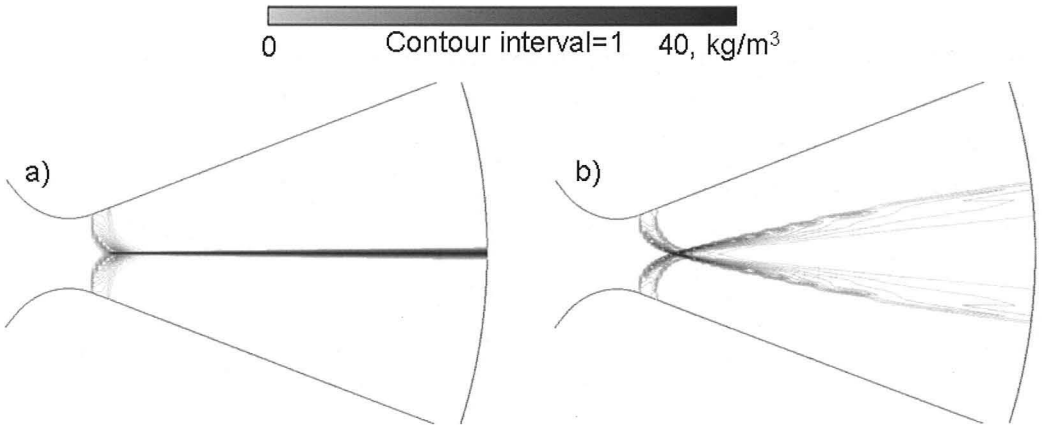

Fig. 111 Comparison of particle bulk density, a) Eulerian-Eulerian method, b) Eulerian-Lagrangian method

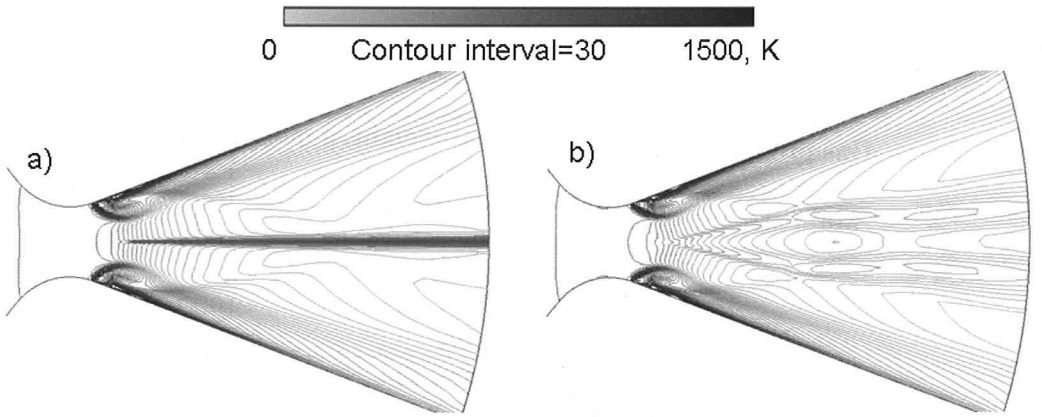

Fig. 112 Comparison of gaseous-phase temperature, a) Eulerian-Eulerian method, b) Eulerian-Lagrangian method

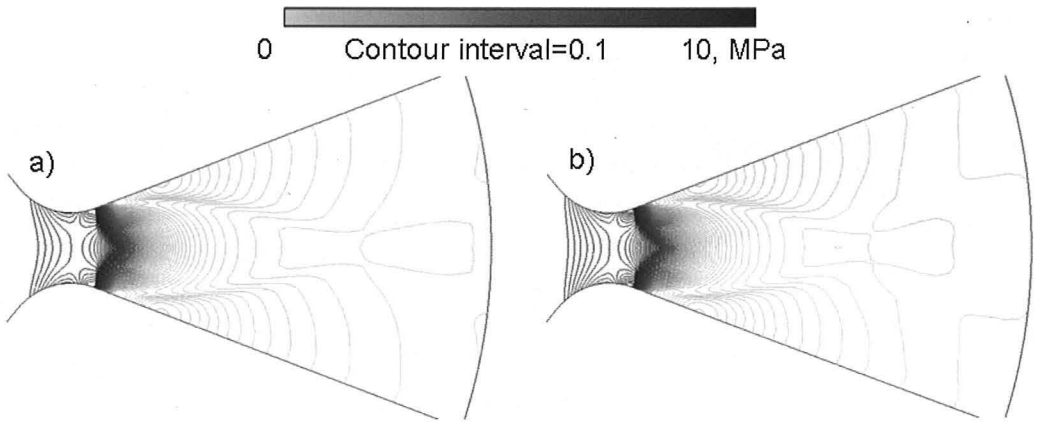

Fig. 113 Comparison of pressure, a) Eulerian-Eulerian method, b) Eulerian-Lagrangian method

Simulation results of the particle bulk density, the gaseous-phase temperature, and the pressure are shown in Fig. 111, Fig. 112, and Fig. 113, respectively. From a comparison of these results, the following remarks can be made.

- In the Eulerian-Eulerian method, since the particle phase is expressed as a continuum, intersecting particle paths cannot be obtained. This is because the physical property must have a single value in a cell even if it is containing crossing particle paths. Therefore, when a jet stream bumps like in this example, the vertical momentum component is cancelled out and only the axial component remains. For this reason, a portion with high particle bulk density is formed in the narrow domain near the axis of center.
- In the Eulerian-Lagrangian method, the flow of a certain particle group does not have direct influence on the flow of other particle groups. Therefore, in this example, the jet streams from the upper and lower sides separate after they cross at the center.
- As for the temperature distribution of the gaseous phase, a difference is found between two methods according to the behavior of two-phase jets.
- In this example, difference in pressure distributions is not significant.

In the above argument, a finite particle-particle interaction is disregarded. Therefore, the Eulerian-Eulerian method serves as a model in which particles interfere very strongly, and, on the other hand, the Eulerian-Lagrangian method becomes a model without particle interaction. It is thought that a finite particle interaction can be treated by introducing a suitable pseudo-diffusion and/or a pseudo-pressure term for the Eulerian-Eulerian method, or introducing appropriate particle collisions into the Eulerian-Lagrangian method.

4.1.2. Two-phase flow inside an SRM[39]

In this example, an SRM of simple form shown previously in Fig. 79 is considered, and an axisymmetric two-phase flow inside the SRM is numerically simulated and compared between the Eulerian-Eulerian method and the Eulerian-Lagrangian method. The particle-phase in the Eulerian-Eulerian method is assumed to have single particle diameter (N_p=1), and three cases of diameters, 2, 20, and 60 μm, are computed for the flow conditions summarized in Table 4 to investigate the behavior of the solution to the particle diameter. The grid system used here is the same as the previous one shown in Fig. 96.

In the Eulerian-Lagrangian method, a burning-surface cell interface is divided into ten, and a particle path is calculated for each segment of the boundary. Since there are 40 cell interfaces of the burning surface, totally 400 paths are calculated. The time step Δt is set so as that it takes about 100 time steps for a particle to cross a representative cell width. Supposing that a particle crosses about 75 cells on the average from the starting point to a terminal point, in total, 400×100×75=3 million particle groups will be treated.

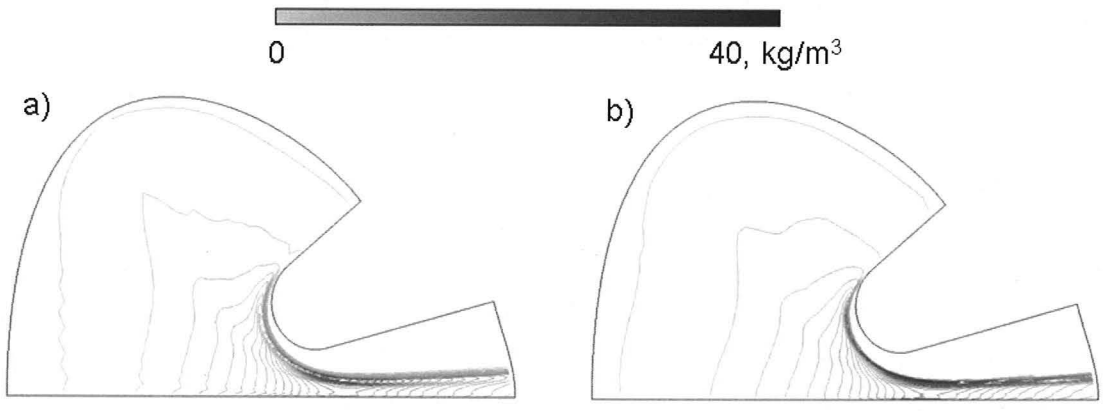

Fig. 114 Comparison of particle bulk density, D_p= 60 μm, a) Eulerian-Eulerian method, b) Eulerian-Lagrangian method

The results of the distribution of particle-bulk density for the case of the particle diameter of 60 μm are compared in Fig. 114. The particle bulk density distributions along some grid lines are shown in Fig. 115 ~ Fig. 117 for all cases of the particle diameter.

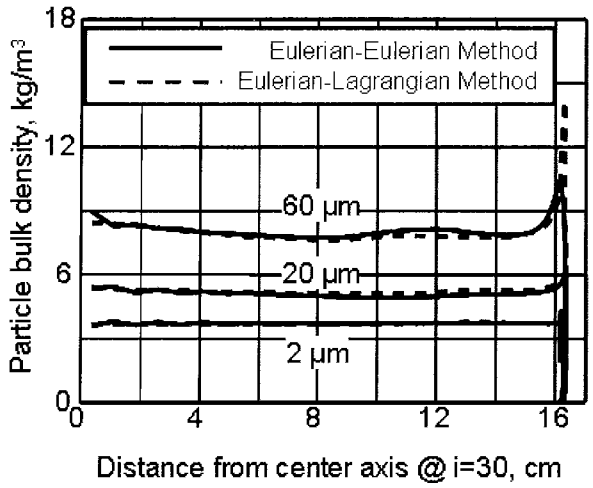

Fig. 115 Comparison of particle bulk density, i=30

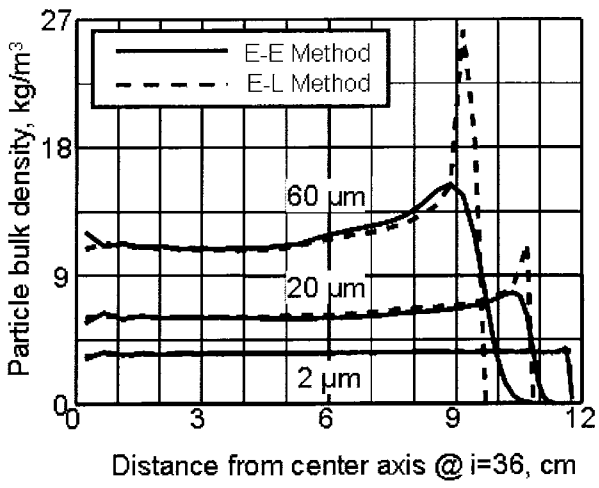

Fig. 116 Comparison of particle bulk density, i=36

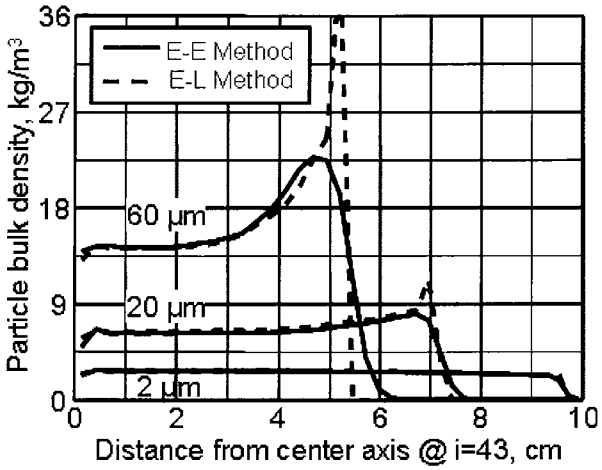

Fig. 117 Comparison of particle bulk density, i=43

From the results the following remarks can be made. The median position of the limiting particle streamline which the Eulerian-Eulerian method and the Eulerian-Lagrangian method compute is mostly in agreement each other. However, whereas a sharp peak appears near the limiting particle streamline by the Eulerian-Lagrangian method, the solution is smeared out due to numerical viscosity automatically introduced by a Riemann-solver-based jump-capturing scheme of the Eulerian-Eulerian method. This difference becomes significant as the particle diameter becomes large, while it hardly appears for the particle diameter of 2 μm.

As for the particle bulk density in the inner region away from the limiting particle streamline, both methods give the same result.

The number of particles used in the Eulerian-Lagrangian method is sufficient to suppress a statistics error, and its

accuracy acquired is equivalent to that of the Eulerian-Eulerian calculation.

The time required for the computations for 10000 time steps is compared between the Eulerian-Eulerian method and the Eulerian-Lagrangian method for the case of the particle diameter of 20 μm. It turns out that, in this case, the Eulerian-Lagrangian method required about 8 times as much time as the Eulerian-Eulerian method for a computer like Hewlett Packard N4000. However, this ratio of computational times depends on the tolerance level of a statistics error.

4.1.3. Two-phase flow in M-34 motor

Axisymmetric simulations of M-34 motor are performed by the Eulerian-Eulerian method and the Eulerian-Lagrangian method as the application to a real-size motor, and the results are compared.

A general view of M-34 motor is shown in Fig. 118. Computation is made assuming axisymmetric flow about geometry of the initial grain shape of the fin-phase cross section.

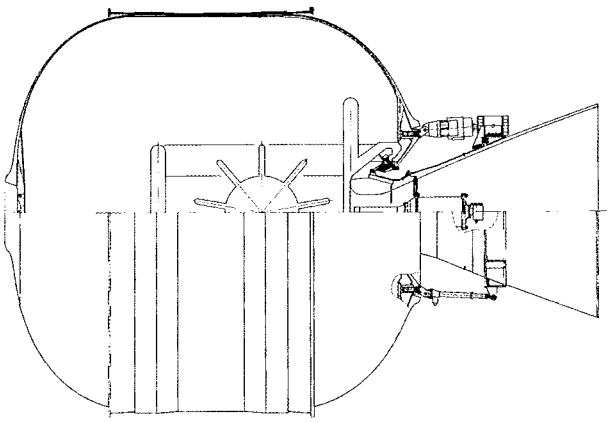

Fig. 118 M-34 motor

Physical properties of the two-phase flow used in the simulation are summarized in Table 16. The transportation coefficients are calculated from the chemical equilibrium composition in the chamber. The particle diameter used is the mass-averaged particle diameter (D_{43}) determined from the throat diameter by a correlation formula. The mass fraction of the particle phase is evaluated assuming that all aluminum are burnt and transformed to alumina. The true density of particle is the value of the solid alumina.

Table 16 Physical properties used in simulation

Combustion pressure, MPa		5.84
Combustion temperature, K		3531
Gas	Specific heat ratio	1.24
	Mean molecular weight, g/mol	18.36
	Prandtl number	0.42
	Viscosity, Pa·sec	$0.364\times10^{-6}\,T^{0.679}$
Particle	Diameter, μm	5.6
	Mass fraction	0.378
	True density, kg/m^3	3590
	Specific heat, J/kg/K	1427

The grid system consisting of 105×71 grid points is shown in Fig. 119. Results of particle bulk density distribution and gaseous-phase temperature distribution are shown in Fig. 120 and Fig. 121, respectively.

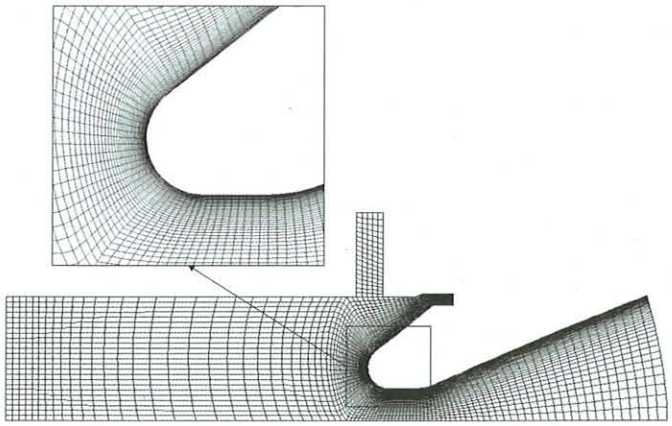

Fig. 119 Grid system for M-34 simulation

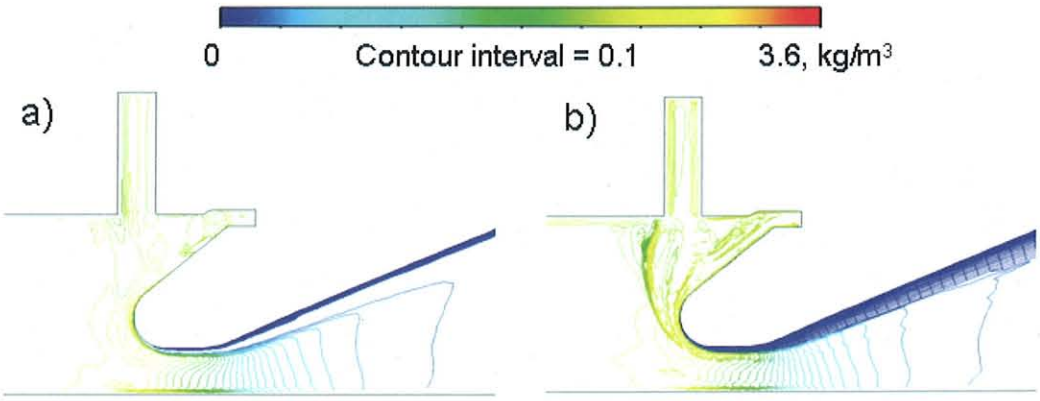

Fig. 120 Comparison of particle bulk density distribution in M-34, a) Eulerian-Eulerian method, b) Eulerian-Lagrangian method

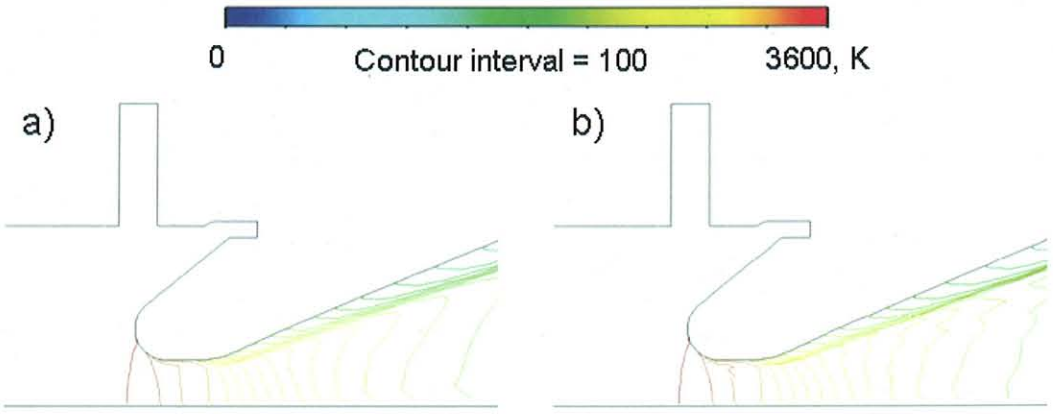

Fig. 121 Comparison of gaseous-phase temperature distribution in M-34, a) Eulerian-Eulerian method, b) Eulerian-Lagrangian method

The result of the Eulerian-Lagrangian method differs in the particle bulk density from that of the Eulerian-Eulerian method in the neighborhood where the flow from the radial slot and the flow in the motor port collide with each other. By the Eulerian-Lagrangian method, a portion with high particle density is formed around the radial slot exit, whereas by the Eulerian-Eulerian method, the flow from the radial slot merges with the core flow of the motor port and the portion does

not appear clearly.

Although the influence of the flow from the radial slot can be seen even in the throat region in the Eulerian-Lagrangian method, the results of the both methods are almost the same in the exit cone region. The size of a separation region, or the position of a limiting particle streamline, is also comparable.

The temperature distribution is almost the same between the two methods.

4.2. Numerical experiments with an Eulerian-hybrid method

4.2.1. Zero-dimensional simulation

In the Eulerian-hybrid method mentioned previously, alumina is supplied to the Eulerian phase according to the combustion of a Lagrangian-phase droplet. The temperature of the Eulerian phase is determined by an interpolation of data in the lookup table with the density, energy, and aluminum fraction being the parameters. Here, in order to verify the function of the chemical equilibrium calculation of the Eulerian-hybrid method, a zero-dimensional simulation in a closed space shown in Fig. 122 is conducted and the result is compared with the chemical-equilibrium calculation.

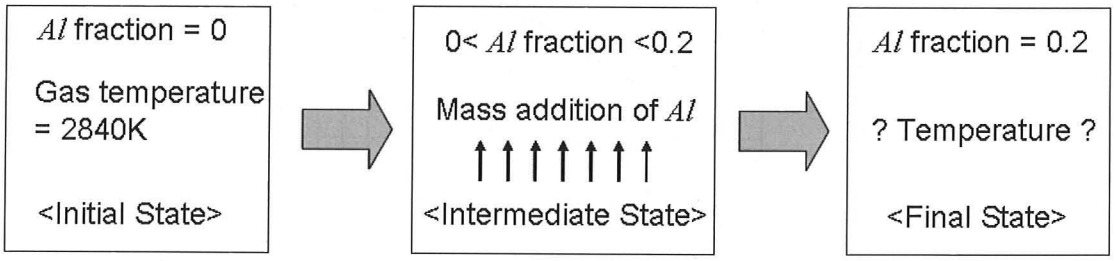

Fig. 122 Zero-dimensional problem

Suppose that a space of constant volume is filled with a stationary combustion gas. Initially, aluminum is not burned and the aluminum fraction in the gas is set to zero. The initial state is such that only AP and HTPB have burned and the chemical equilibrium has been reached. Suppose that mass of aluminum is repetitively added to the gaseous-phase (Eulerian phase) at an appropriate time interval due to aluminum combustion. The density and the aluminum fraction of gas rise with the supply of aluminum. The state variables varying every moment are analyzed by referring the lookup tables. The aluminum supply is continued until aluminum mass fraction finally becomes 20%.

The change of temperature to the aluminum mass fraction obtained from the analysis is shown in Fig. 123. The result is compared with the result obtained by a chemical equilibrium calculation at a constant pressure employing an SP-273[34] code. Although it is not strict comparison because calculation here assumes constant volume whereas the other does constant pressure, the behavior of calculation results for the combustion temperature changing with the aluminum mass fraction is in general in agreement with each other.

4.2.2. Axisymmetric simulation 1 ～ Forced combustion model ～

It turns out by the above-mentioned zero-dimensional simulation that physical properties such as the temperature can be computed appropriately by the table-lookup method in case that there is aluminum mass addition. Next, let us consider the case in which fluid dynamics is coupled with this. As such a case, an axisymmetric end-burning motor with a chamber and a nozzle shown in Fig. 124 is considered. The left-end boundary of the computational domain is the burning surface.

Let us set up a situation in which the aluminum-less combustion gas, which is the product of AP and HTPB burn, is flowing from the burning surface into the computational domain, and as it flows through the chamber, aluminum is gradually added to the Eulerian phase according to a prescribed function of a distance also shown in Fig. 124. The objective here is to confirm the capability of the present simulation of the Eulerian-phase flow for the case where the mass

addition of aluminum to the Eulerian-phase is taken into account by a source term.

The grid system used consists of 121×51 grid points and is shown in Fig. 125. The results of the temperature, the aluminum mass fraction in the Eulerian phase, and the bulk density distribution of alumina smoke are shown in Fig. 126, Fig. 127, and Fig. 128, respectively.

It is confirmed from these figures that, as a result of compulsory source term of aluminum mass addition, the temperature increases from 2800K to 3500K according to the mass fraction of aluminum, and that the changes of the temperature and the density in a nozzle portion are appropriately calculated by using the present lookup table of state.

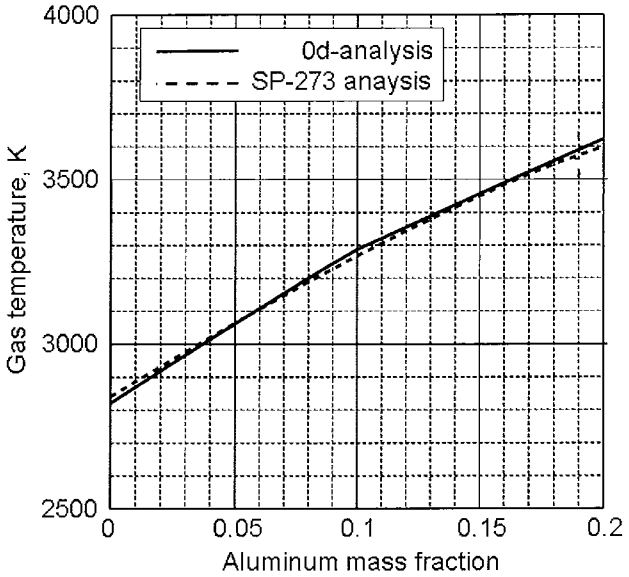

Fig. 123 Comparison of gas temperature results

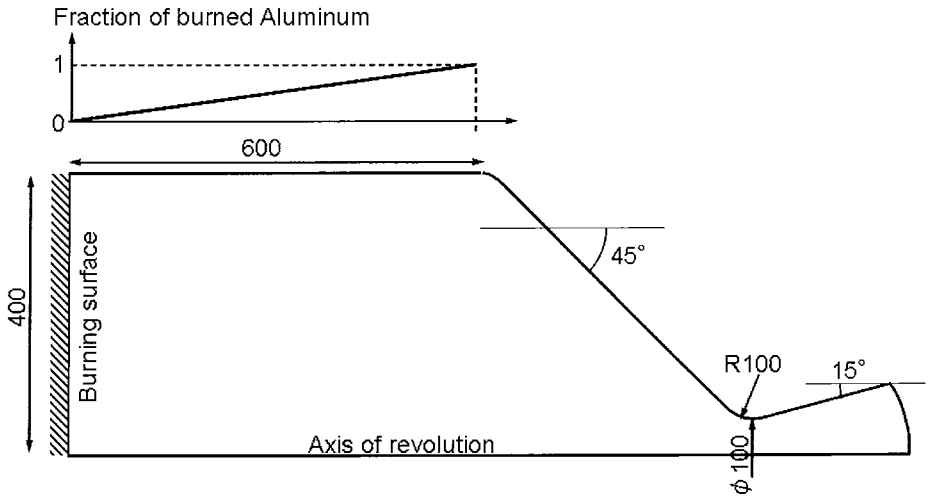

Fig. 124 Axisymmetric SRM model, No.1

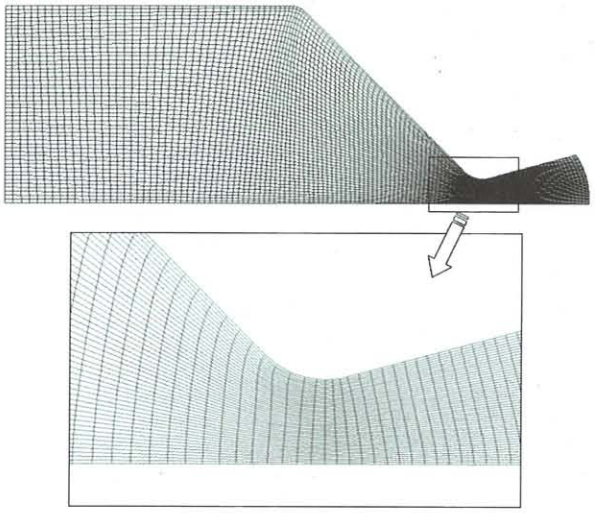

Fig. 125 Grid system

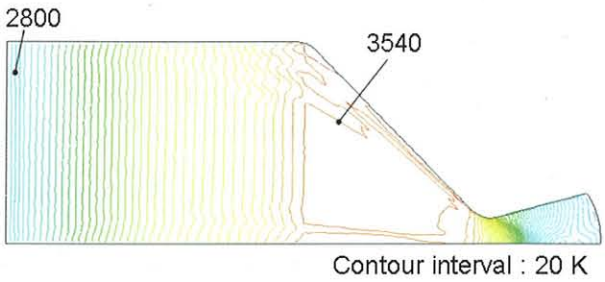

Fig. 126 Temperature distribution

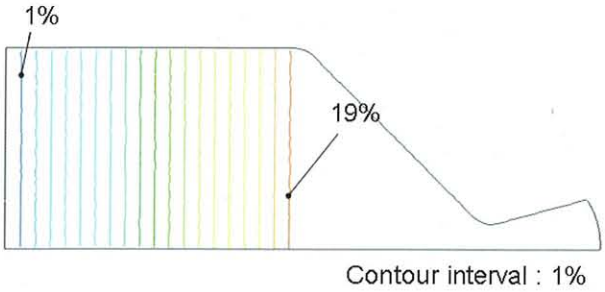

Fig. 127 Aluminum mass fraction

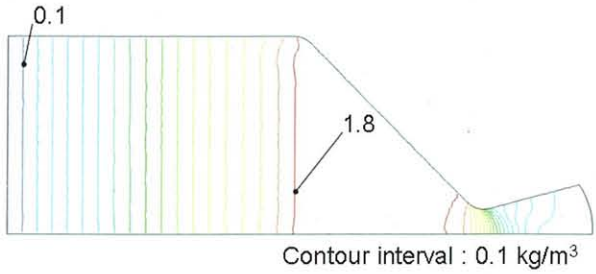

Fig. 128 Bulk density of alumina smoke

4.2.3. Axisymmetric simulation 2 ～ Fixed-initial-particle-diameter model ～

In the forced combustion model of the foregoing paragraph, the aluminum fraction is controlled compulsorily according to a distance function regardless of combustion of a particle and it is confirmed that the Eulerian-phase flow with aluminum mass addition can be properly simulated by the present method. Next, a two-phase flow is considered by introducing particles into this. The SRM model is basically the same as the foregoing paragraph except that simulation particles are generated from the burning surface shown in Fig. 129.

The motion of the particle is solved simultaneously with the change of the particle diameter due to combustion and the supply of the aluminum to the Eulerian phase. In this section, it is assumed tentatively that the initial diameter of generated particles is fixed and no distribution is considered concerning the initial diameter.

The grid system is the same as the one shown in Fig. 125. The flow conditions and simulation parameters are summarized in Table 17. The ratio of aluminum mass in the alumina cap which finally remains to all the aluminum mass in the propellant is denoted by ψ.

The results of the temperature of the Eulerian phase, the aluminum mass fraction in the Eulerian phase, the bulk density distribution of alumina smoke, and the bulk density of the Lagrangian phase are shown in Fig. 130, Fig. 131, Fig. 132, and Fig. 133, respectively.

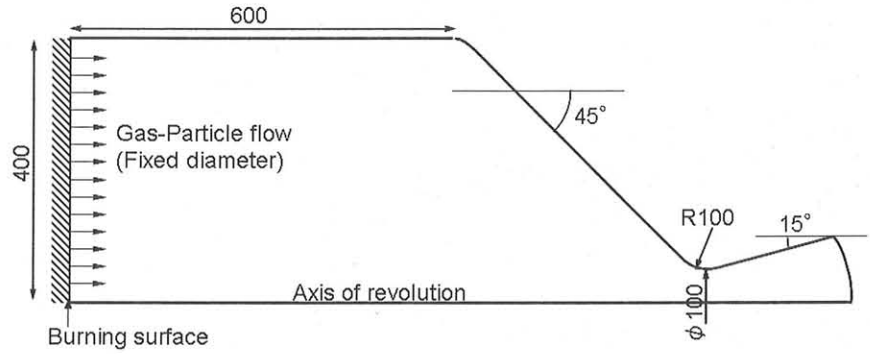

Fig. 129 Axisymmetric model, No. 2

Table 17 Flow conditions and simulation parameters

Combustion pressure, MPa	5
ψ	0.2
Viscous coefficient, Pa·sec	$0.348\times10^{-6}\,T^{0.685}$
Prandtl number	0.42
Particle diameter (fixed), μm	150
The number of particle generated per a boundary segment	40

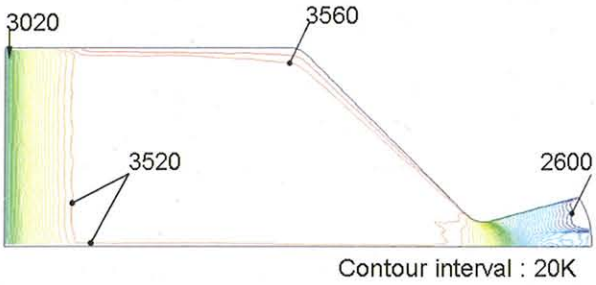

Fig. 130 Temperature of Eulerian phase

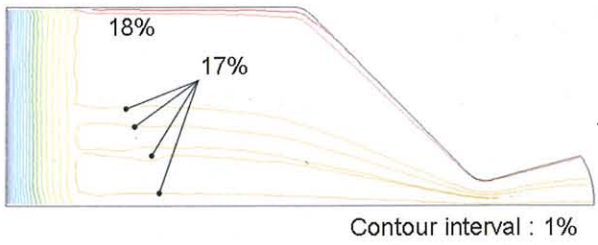

Fig. 131 Aluminum mass fraction of Eulerian phase

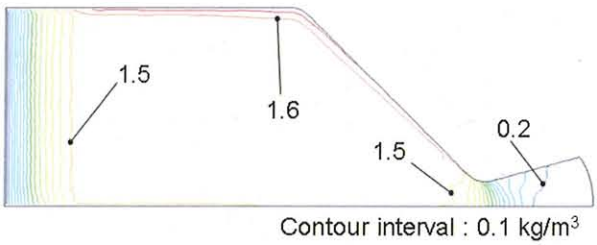

Fig. 132 Bulk density of alumina smoke

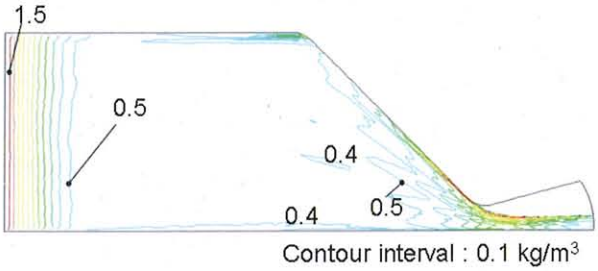

Fig. 133 Bulk density of Lagrangian phase

Combustion of a particle is completed in the distance about 140mm from the burning surface, and an almost uniform-state region is realized in the combustion chamber. While the alumina-smoke bulk density rises according to the combustion, the bulk density of the Lagrangian (condensed) phase declines. Accordingly, the temperature which is about 3000K at the burning surface is rising to more than 3500K at the end of combustion. Since the particle diameter of

Lagrangian phase after combustion is comparatively large (105 μm), the separation of the Lagrangian-phase particle flow in the nozzle exit cone is large.

4.2.4. Axisymmetric simulation 3 ~ Mono-modal model ~

Here in the axisymmetric model No.3 (Fig. 134), the foregoing simulations are modified so that the initial diameter of each particle at the burning surface is given from a log-normal distribution, Eq. (224), with the mass-averaged diameter of 150 μm and the variance σ of 0.2. The flow conditions and simulation parameters are summarized in Table 18.

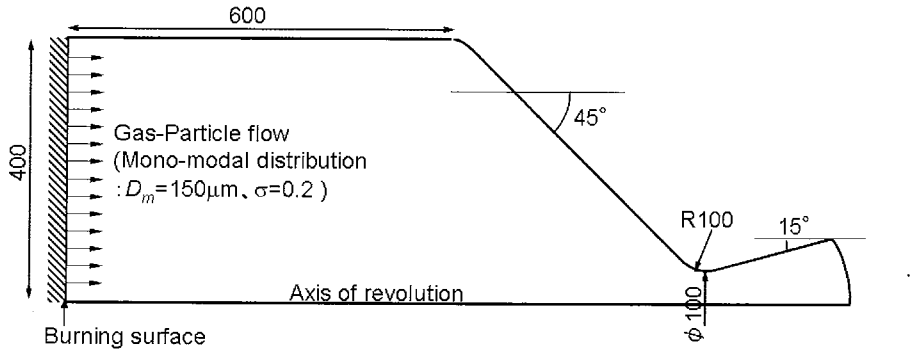

Fig. 134 Axisymmetric model, No. 3

Table 18 Flow conditions and simulation parameters

Combustion pressure, MPa	5
ψ	0.2
Viscous coefficient, Pa-sec	$0.348\times10^{-6}\,T^{0.685}$
Prandtl number	0.42
Particle diameter distribution	Mono-modal
Mass-averaged diameter D_m, μm	150
Variance σ	0.2
The number of particle generated per a boundary segment	40

The results of the temperature of the Eulerian phase, the aluminum mass fraction in the Eulerian phase, the bulk density distribution of alumina smoke, and the bulk density of the Lagrangian phase are shown in Fig. 135, Fig. 136, Fig. 137, and Fig. 138, respectively. The distribution of the particle diameter of the Lagrangian phase discharged from the nozzle is shown in Fig. 139. The total sampling number of the distribution is about 8700.

Although the flow field is roughly the same as the case of single particle diameter, when a particle diameter distribution is taken into account, some heterogeneity arises in the combustion chamber to form a distribution of physical quantities. Some large particles reach the wall surface before having burned completely within the combustion chamber. The particle diameter of Lagrangian phase discharged from the nozzle is a distribution with the peak of 100 μm, and therefore large separation occurs in the nozzle exit cone.

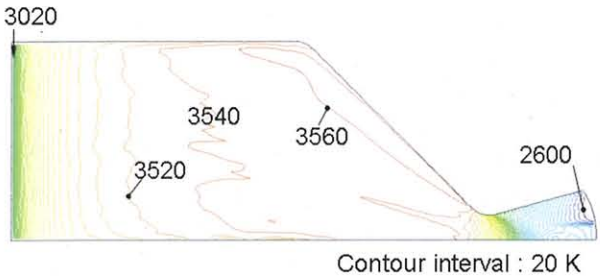

Fig. 135 Temperature of Eulerian phase

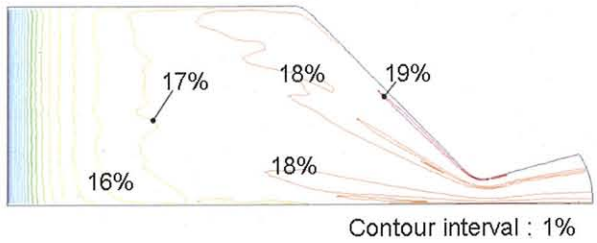

Fig. 136 Aluminum mass fraction of Eulerian phase

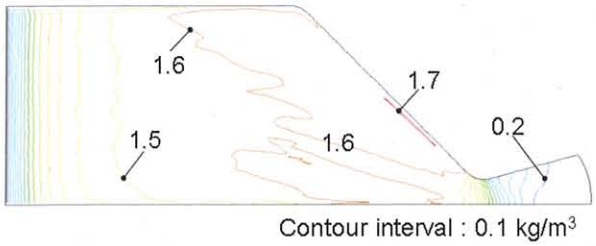

Fig. 137 Bulk density of alumina smoke

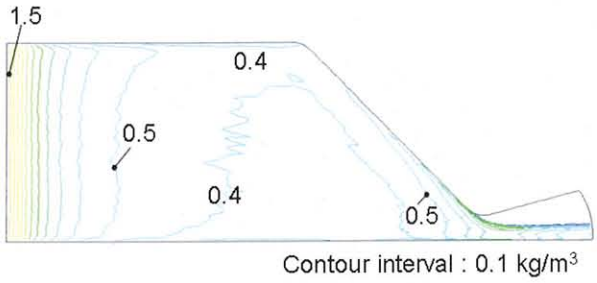

Fig. 138 Bulk density of Lagrangian phase

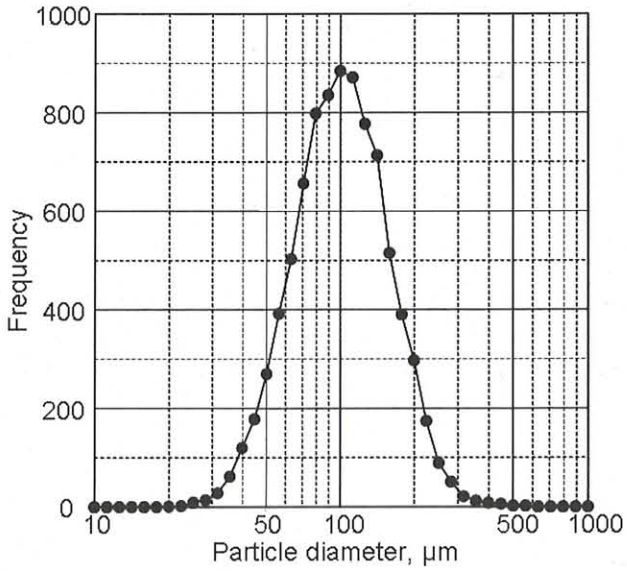

Fig. 139 Diameter distribution of the Lagrangian-phase particles discharged from the nozzle (N ≈ 8700)

4.2.5. Axisymmetric simulation 4 ～ Bi-modal model ～

Here in the axisymmetric model No.4 (Fig. 140), the foregoing simulations are modified so that the initial diameter of each particle at the burning surface is given from a bi-modal distribution, Eq.(226), which is made by superimposing a log-normal distribution with the mass-averaged diameter of 150 μm and the variance σ of 0.2 and another log normal distribution with the mass-averaged diameter of 1.5 μm and the variance σ of 0.4. It is assumed that particles belonging to the second log-normal distribution are all alumina particles and no more combustion occurs in the combustion chamber.

Flow conditions and simulation parameters are summarized in Table 19.

The results of the temperature of the Eulerian phase, the aluminum mass fraction in the Eulerian phase, the bulk density distribution of alumina smoke, and the bulk density of the Lagrangian phase are shown in Fig. 141, Fig. 142, Fig. 143, and Fig. 144, respectively. The distribution of the particle diameter of the Lagrangian phase discharged from the nozzle is shown in Fig. 145. The total sampling number of the distribution is about 9000. It should be noted that a particle below 1 μm is not treated as a Lagrangian-phase particle.

Fundamentally, a similar flow field is formed for the bi-modal distribution as it is for the mono-modal one. The homogeneity in the combustion chamber is a little better with the bi-modal distribution than the mono-modal one because the former has fewer large particles than the latter. Since the distribution of the diameters of Lagrangian-phase particles discharged from the nozzle has the peak of 70 ~ 90 μm, the separation region is still large for this case though it is a little smaller than that of the mono-modal case.

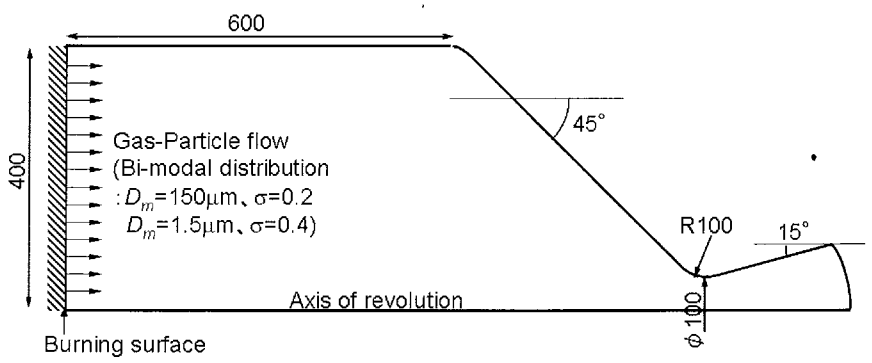

Fig. 140 Axisymmetric model, No.4

Table 19 Flow conditions and simulation parameters

Combustion pressure, MPa	5
ψ	0.2
Viscous coefficient, Pa·sec	$0.348\times10^{-6}\,T^{0.685}$
Prandtl number	0.42
Particle diameter distribution	Bi-modal
Mass-averaged diameter D_m, μm	150, 1.5
Variance σ	0.2, 0.4
f_0	0.8
The number of particle generated per a boundary segment	40

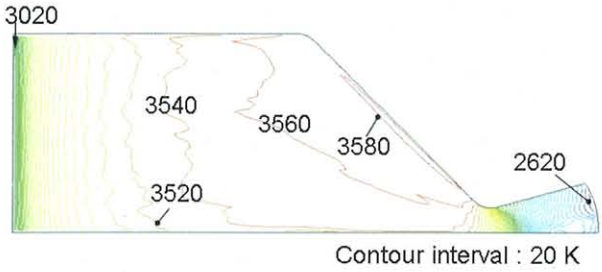

Fig. 141 Temperature of Eulerian phase

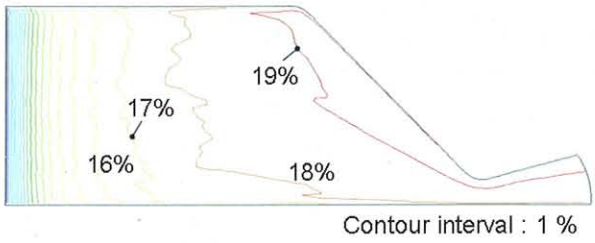

Fig. 142 Aluminum mass fraction of Eulerian phase

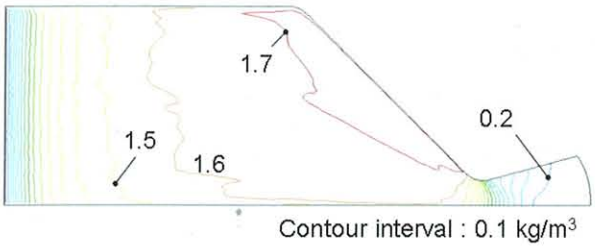

Fig. 143 Bulk density of alumina smoke

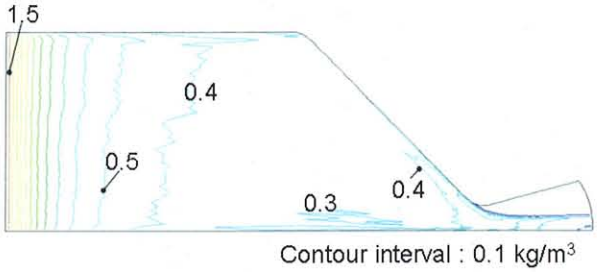

Fig. 144 Bulk density of Lagrangian phase

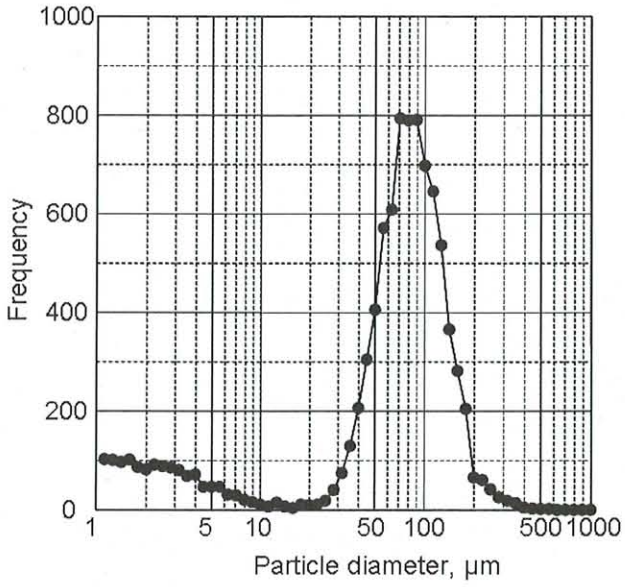

Fig. 145 Diameter distribution of the Lagrangian-phase particles discharged from the nozzle (N ≈ 9000)

4.2.6. Axisymmetric simulation 5 ～ Bi-modal model with particle breakup ～

As is seen previously, particles of the diameter larger than 100 μm stay as large as several tens of microns after the completion of their combustion, and therefore, the particle path separates from the nozzle wall significantly in the exit cone. However, the mass-averaged particle diameter evaluated from samples taken from the exhaust gas in static firing tests is usually several microns and this fact contradicts a result here greatly. One of the major reasons of this difference is particle-breakup phenomena caused by shear stress imposed from the surrounding gas flow which is rapidly accelerated

near the throat region. The fact that the mass-averaged particle diameter of the particles in the exhaust gas has a strong correlation with the throat diameter also suggests that this is one of the reasons.

Here, in the model No.5 (Fig. 146), the effect of particle breakup is incorporated in the analysis of the bi-modal model of the foregoing paragraph. The flow conditions and simulation parameters are summarized in Table 20. The particle-breakup criterion is given by Eq. (222).

The results of the temperature of the Eulerian phase, the aluminum mass fraction in the Eulerian phase, the bulk density distribution of alumina smoke, and the bulk density of the Lagrangian phase are shown in Fig. 147, Fig. 148, Fig. 149, and Fig. 150, respectively. The distribution of the particle diameter of the Lagrangian phase discharged from the nozzle is shown in Fig. 151. The total sampling number of the distribution is about 9000.

Since particle breakup occurs near the throat, the flow field in the combustion chamber up to the throat is almost the same as that of the case without particle breakup. A big particle quickly breaks up into small particles near the throat. For this reason, the separation of the particle path from the wall is much smaller compared with the foregoing paragraph. The distribution of the diameters of discharged particles has the peak around 5 to 8 μm, and the frequency of particles of the size larger than 10 μm becomes very small.

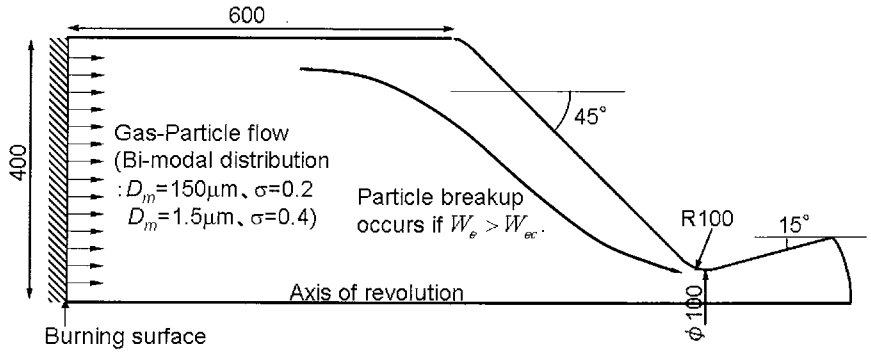

Fig. 146 Axisymmetric model, No.5

Table 20 Flow conditions and simulation parameters

Combustion pressure, MPa	5
ψ	0.2
Viscous coefficient, Pa-sec	$0.348\times10^{-6}\,T^{0.685}$
Prandtl number	0.42
Particle diameter distribution	Bi-modal
Mass-averaged diameter D_m, μm	150, 1.5
Variance σ	0.2, 0.4
f_0	0.8
Surface tension σ_p, N/m	0.84
The number of particle generated per a boundary segment	40

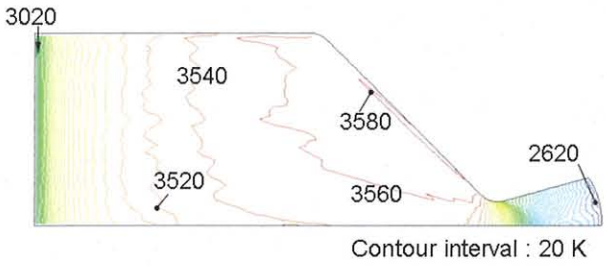

Fig. 147 Temperature of Eulerian phase

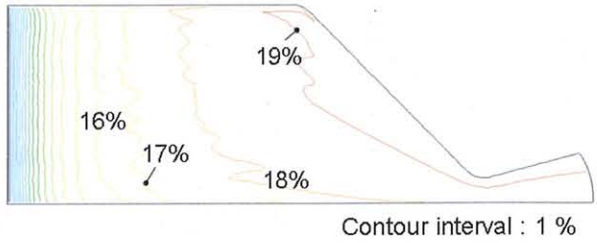

Fig. 148 Aluminum mass fraction of Eulerian phase

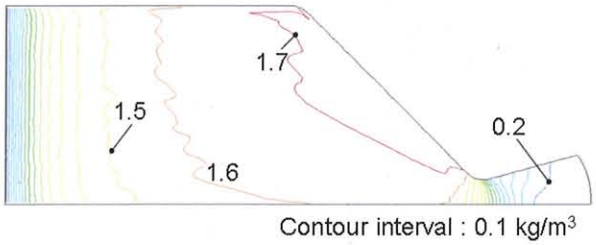

Fig. 149 Bulk density of alumina smoke

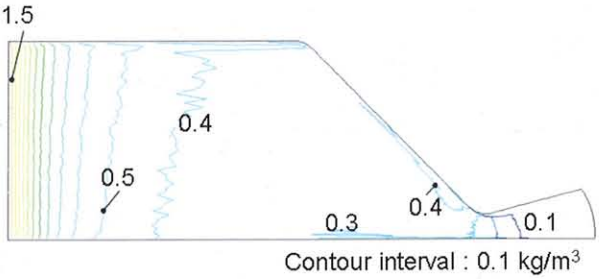

Fig. 150 Bulk density of Lagrangian phase

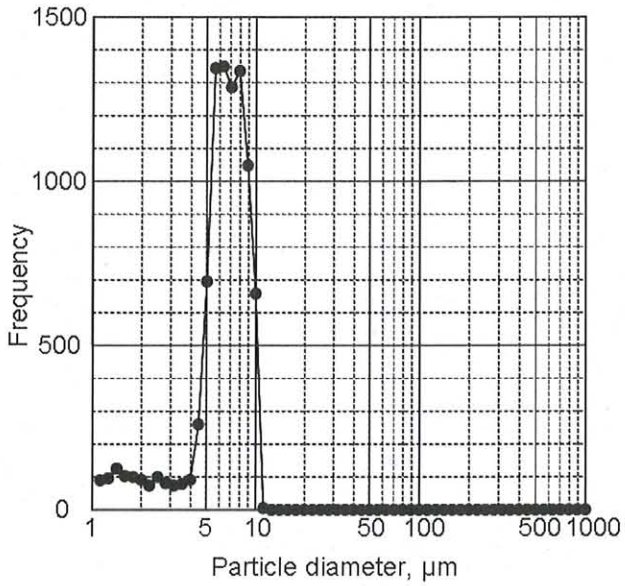

Fig. 151 Diameter distribution of the Lagrangian-phase particles discharged from the nozzle (N ≈ 9000)

4.2.7. Three-dimensional simulation

Here, the present Eulerian-hybrid method is extended to three-dimensional simulation of multiphase flow inside SRM. The initial particle diameter at the burning surface is determined from the bi-modal frequency function and its cumulative distribution function of Fig. 106 and Fig. 107, respectively. The computational process of the particle generation using a random number is shown in Fig. 82. As the maximum and the minimum diameters of the simulation particle, $D_{p,max}$ and $D_{p,min}$, respectively, are set as 1000 μm and 1 μm.

A motor with the throat diameter of 80 mm shown in Fig. 152 is chosen as an object of the three-dimensional simulation. The configuration of the propellant grain is fin-on-cylinder ("finocyl") type and has seven slots in the axial direction. Since the target motor has seven axial slots in the propellant grain, the one fourteenth of the circumference is dealt as the computational region. The flow conditions and simulation parameters are shown in Table 21.

In order to reduce the computational time, the number of particle generated per one boundary-cell segment is set to 1, and the statistical error is reduced by increasing the substantial number of particles with the use of time-averaged phase-interaction term.

The starting position of the influx particle from a boundary segment is randomly scattered within a cell. Particles which collide with a wall including burning surface are assumed to bounce specularly into the computational domain.

The grid system consisting of 95×58×25 points with 2416 burning-surface boundary segments is shown in Fig. 153.

The results of the density, the pressure, and the temperature of the Eulerian phase in the slot-phase, the fin-phase, and their intermediate-phase cross sections are plotted in Fig. 154, Fig. 155, and Fig. 156, respectively. Also the results of the bulk density of alumina smoke, the bulk density, and the temperature of the Lagrangian-phase are shown in Fig. 157, Fig. 158, and Fig. 159, respectively. Those properties in the other cross sections such as cross sections A-A', B-B', and C-C' are shown in Fig. 160, Fig. 161, and Fig. 162, respectively.

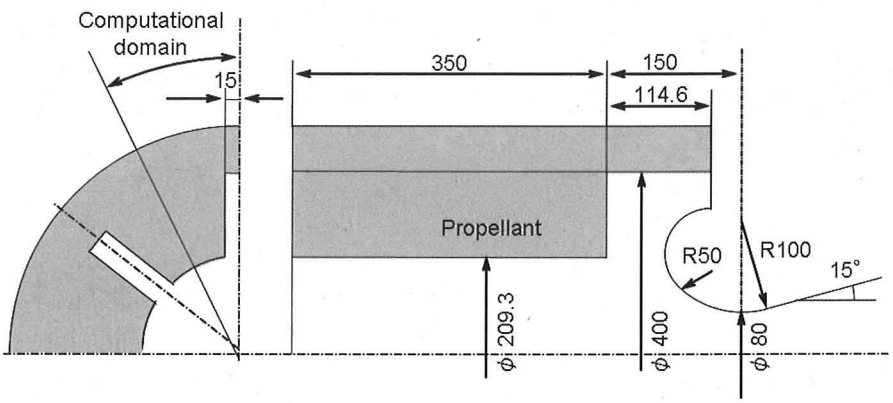

Fig. 152 Model SRM for 3D simulation

Table 21 Flow conditions and simulation parameters

Combustion pressure, MPa	5.4
ψ	0.2
Viscous coefficient, Pa-sec	$0.348\times10^{-6}\,T^{0.685}$
Prandtl number	0.42
Particle diameter distribution	Bi-modal
Mass-averaged diameter D_m, μm	150, 1.5
Variance σ	0.2, 0.4
f_0	0.8
Surface tension σ_t, N/m	0.84
The number of particle generated per a boundary segment	1

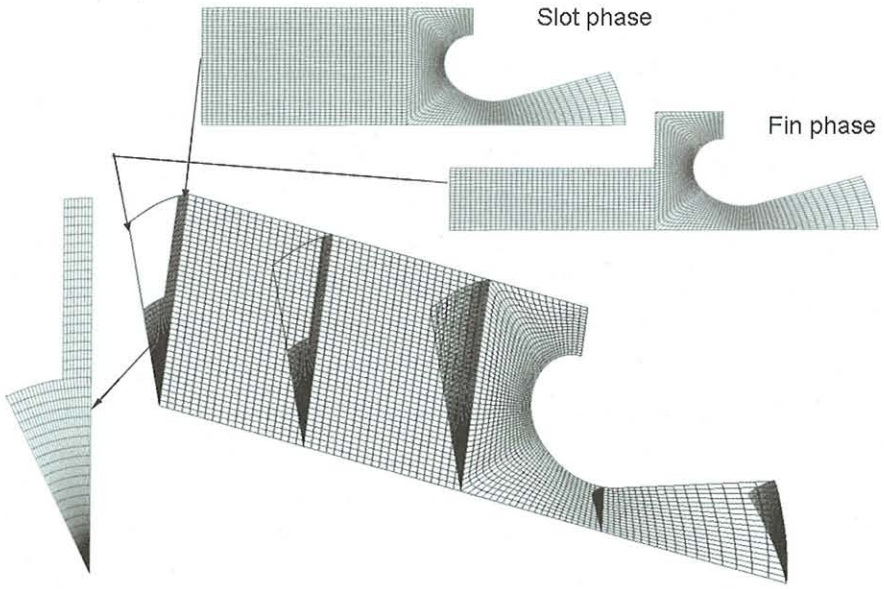

Fig. 153 Grid system

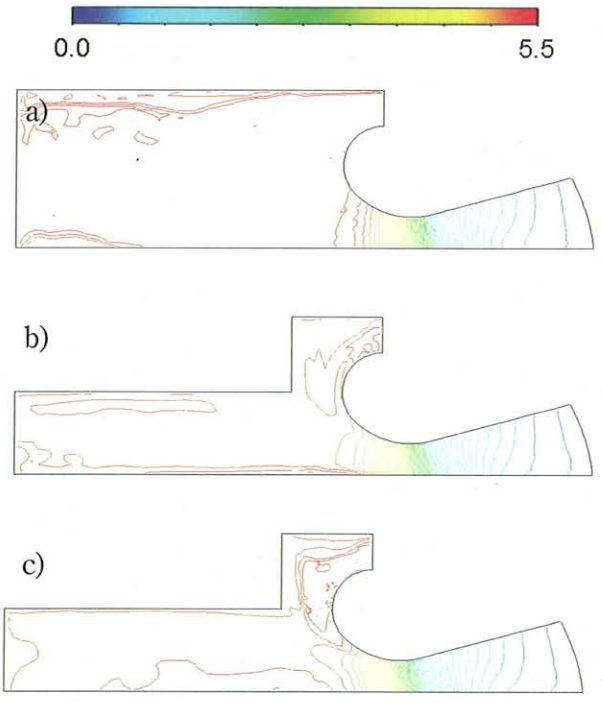

Fig. 154 Density of Eulerian phase, kg/m³ Contour interval: 0.1, a) Slot phase, b) Intermediate phase, c) Fin phase

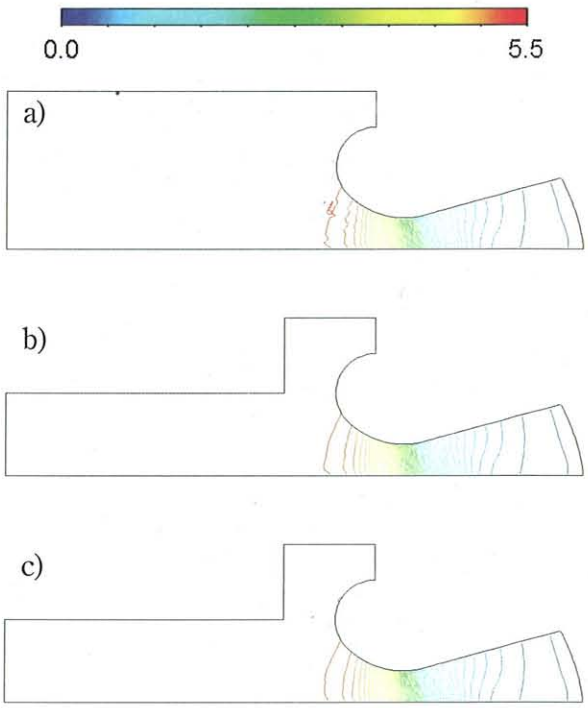

Fig. 155 Pressure, MPa, Contour interval: 0.1, a) Slot phase, b) Intermediate phase, c) Fin phase

Particle paths are shown in Fig. 163, in which paths are thinned out and displayed so that a particle path is legible. The distributions of mass and momentum fluxes of Lagrangian-phase particles which collide with the nozzle surface are shown in Fig. 164 and Fig. 165, respectively.

Finally, the distribution of the particle diameter of Lagrangian phase at the nozzle exit is shown in Fig. 166. It should be noted that a particle of the diameter smaller than 1 μm are not counted as a Lagrangian-phase particle.

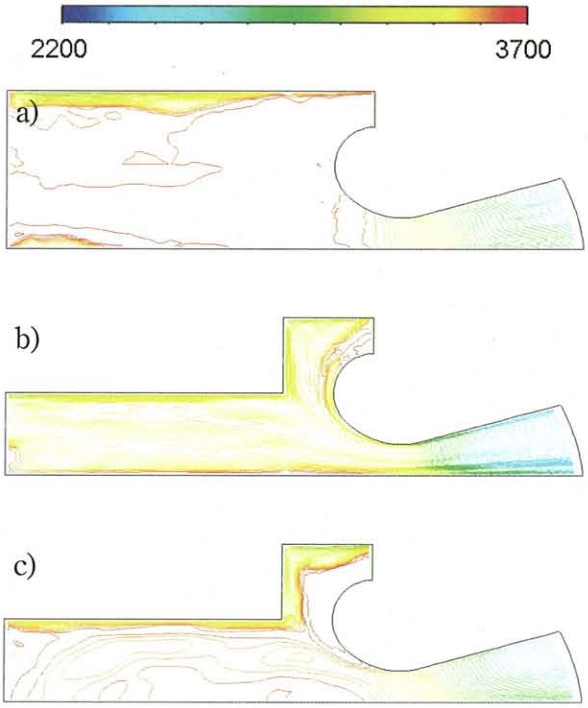

Fig. 156 Eulerian-phase temperature, K, Contour interval: 20, a) Slot phase, b) Intermediate phase, c) Fin phase

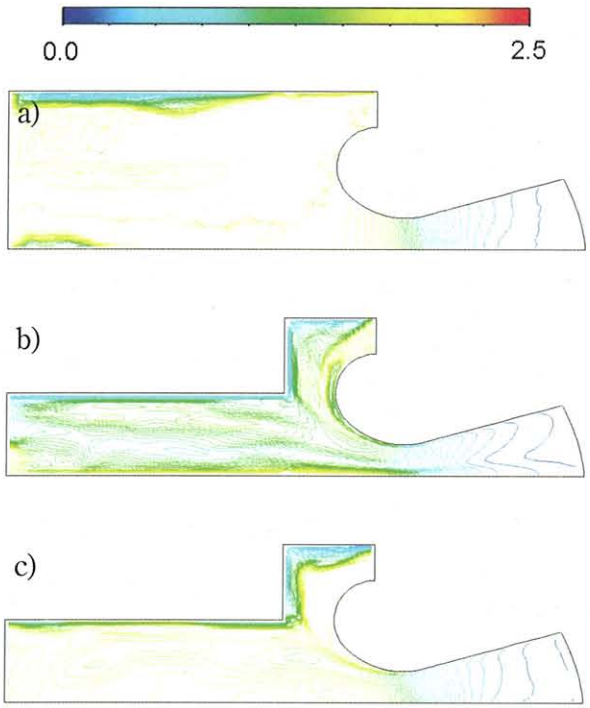

Fig. 157 Bulk density of alumina smoke, kg/m^3, Contour interval: 0.05, a) Slot phase, b) Intermediate phase, c) Fin phase

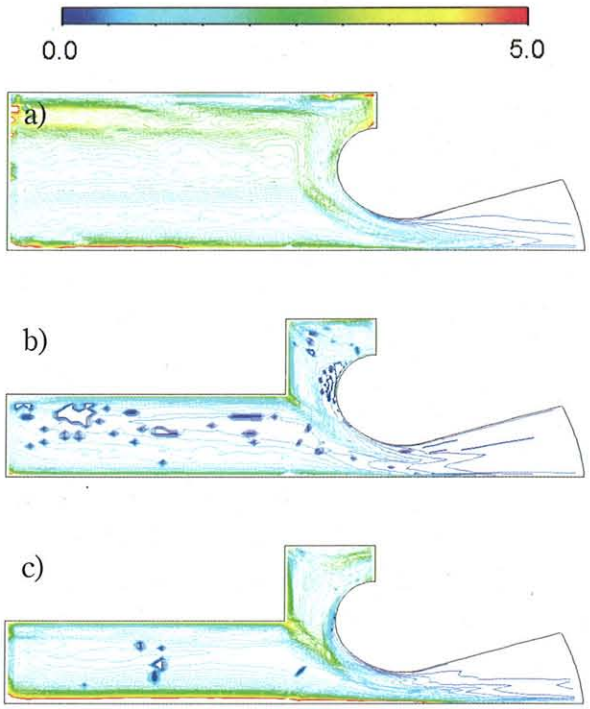

Fig. 158 Bulk density of Lagrangian phase, kg/m^3, Contour interval: 0.1, a) Slot phase, b) Intermediate phase, c) Fin phase

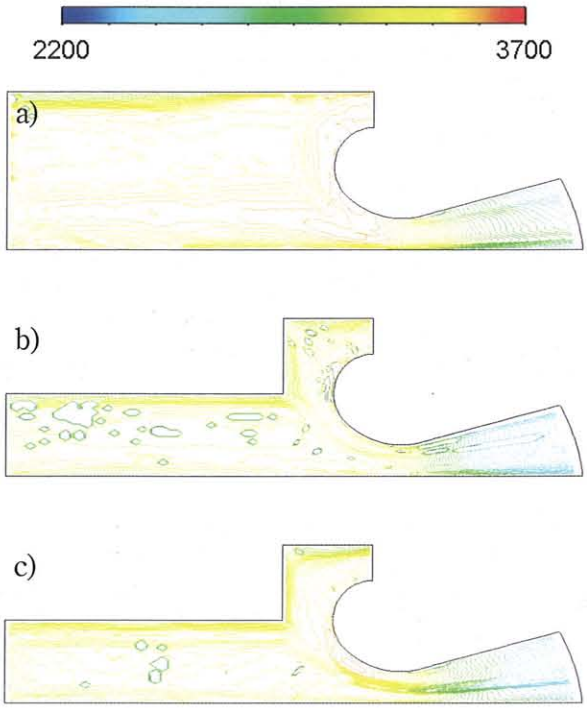

Fig. 159 Temperature of Lagrangian phase, K, Contour interval: 20, a) Slot phase, b) Intermediate phase, c) Fin phase

As a result of employing the Eulerian-hybrid method in which combustion of a Lagrangian particle is considered, the temperature of the both phases is low in the vicinity of burning surface and it rises as the distance from the burning surface increases.

There is a low-temperature region between the slot phase and the fin phase. It is thought that, since the bulk density of the Lagrangian phase is not so low in this region, particles cannot burn easily and the temperature does not go up there.

The effect of slots and fins can be seen in the density distribution and the temperature distribution in the throat cross section (C-C').

The amount of physical properties seems to change a lot on the azimuthal boundary, but this has the possibility of a numerical problem under the influence of the boundary conditions for the Eulerian phase.

As seen in Fig. 158, although a considerable number of particles are sampled, there still are cells in which the physical properties cannot be calculated well because no particle may pass. It is a general trend for three-dimensional calculation that such a cell may appear, therefore, it is considered that there is room of improvement of methods for generating an initial position of particle and for sampling particles.

From the observation of particle paths, it turns out that many particles have collided with a wall surface including a burning surface. Although specular surface reflection has been assumed for convenience here, it will be necessary to examine the particle reflection model.

The distributions of the mass and momentum fluxes by the Lagrangian-particles colliding with a nozzle inlet surface bear a strong resemblance to the erosion pattern seen on the nozzle inlet after a static firing test. Better understanding on the erosion pattern of the TPS materials at the inlet of a nozzle[40] may be obtained through such approach.

The particle diameter distribution at the nozzle exit has a peak at several microns, and this agrees usually with results of static firing tests.

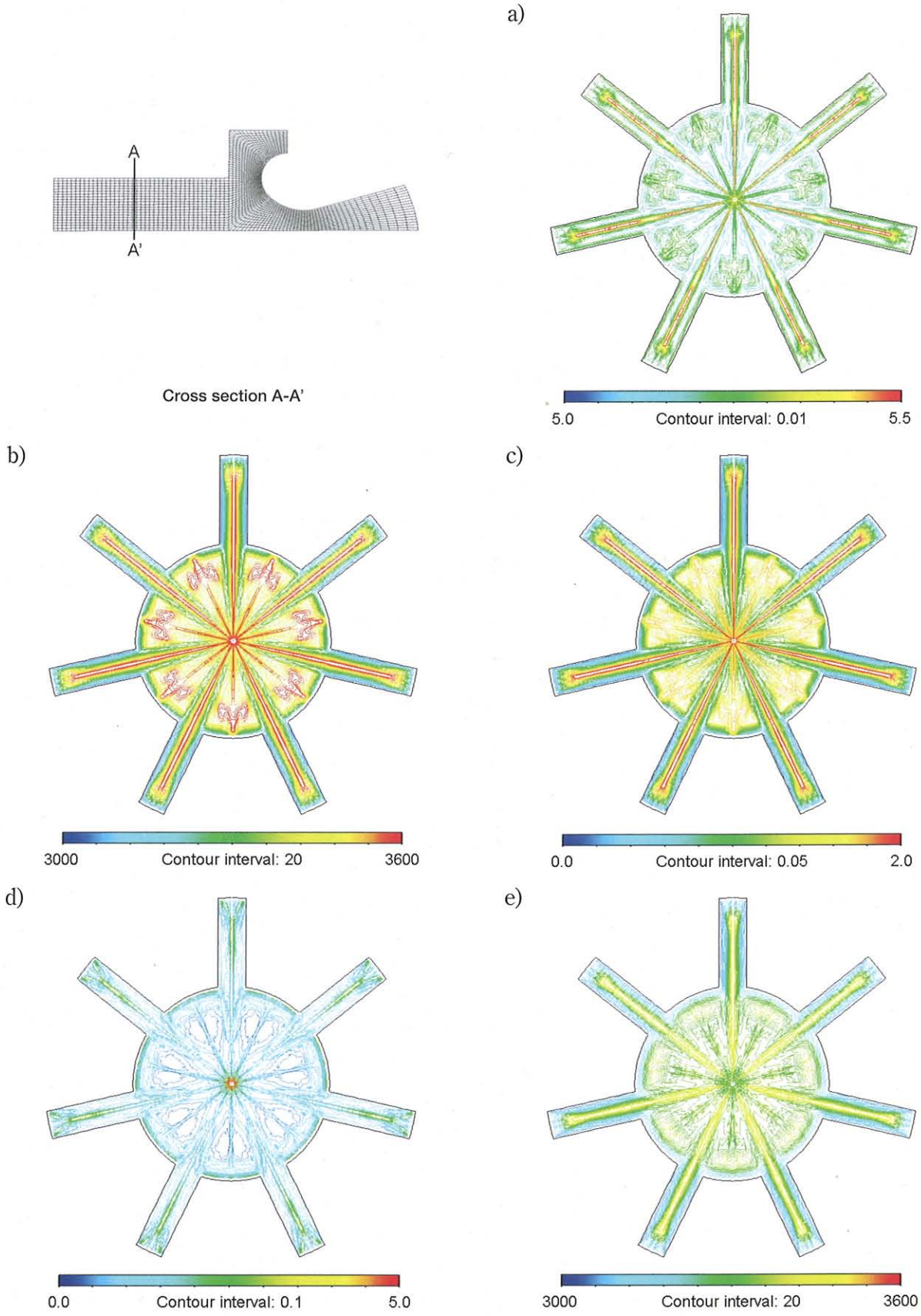

Fig. 160 Properties in A-A' cross-section, a) Density of Eulerian phase, kg/m³, b) Eulerian-phase temperature, K, c) Bulk density of alumina smoke, kg/m³, d) Bulk density of Lagrangian phase, kg/m³, e) Lagrangian-phase temperature, K

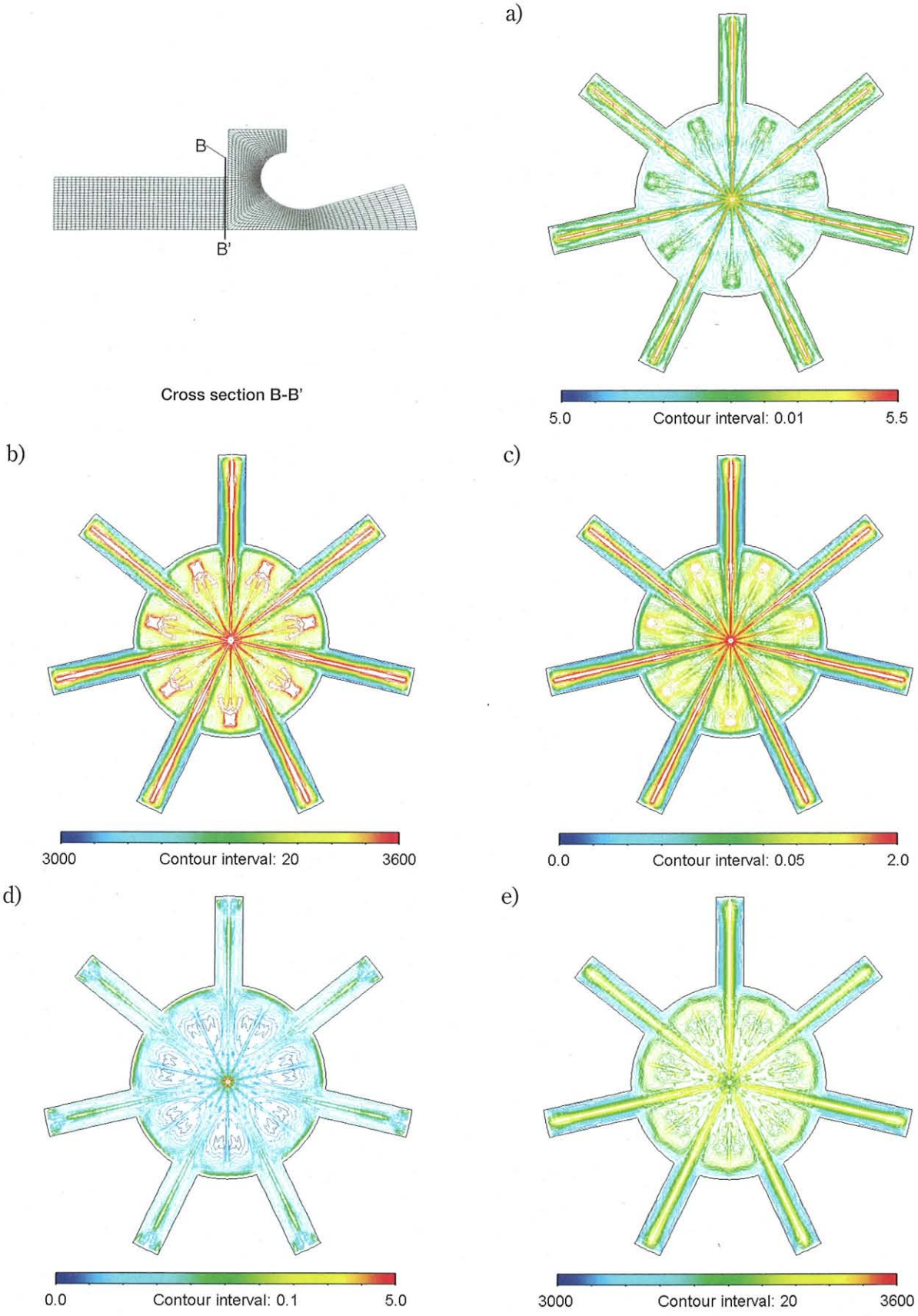

Fig. 161 Properties in B-B' cross-section, a) Density of Eulerian phase, kg/m³, b) Eulerian-phase temperature, K, c) Bulk density of alumina smoke, kg/m³, d) Bulk density of Lagrangian phase, kg/m³, e) Lagrangian-phase temperature, K

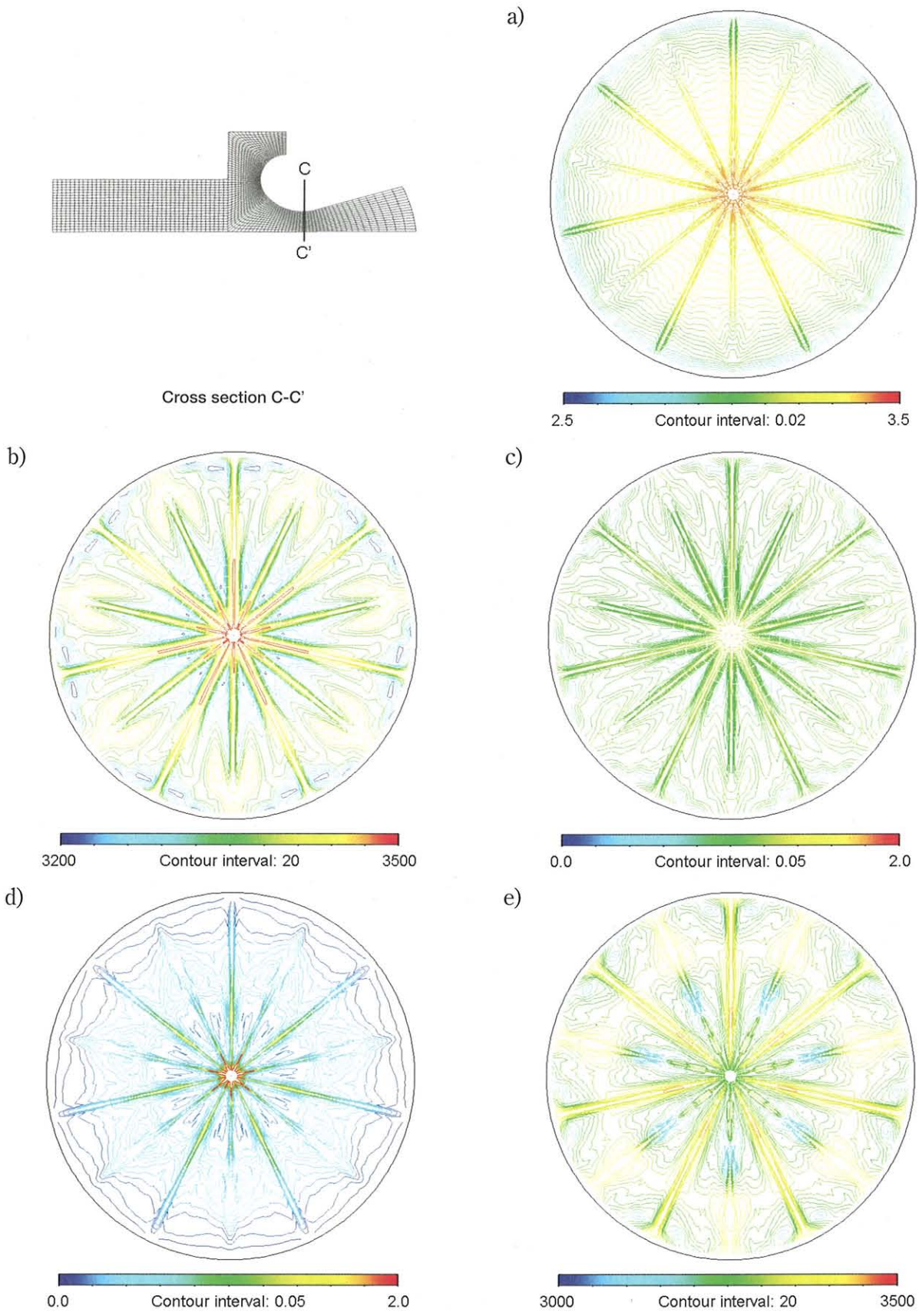

Fig. 162 Properties in C-C' cross-section, a) Density of Eulerian phase, kg/m³, b) Eulerian-phase temperature, K, c) Bulk density of alumina smoke, kg/m³, d) Bulk density of Lagrangian phase, kg/m³, e) Lagrangian-phase temperature, K

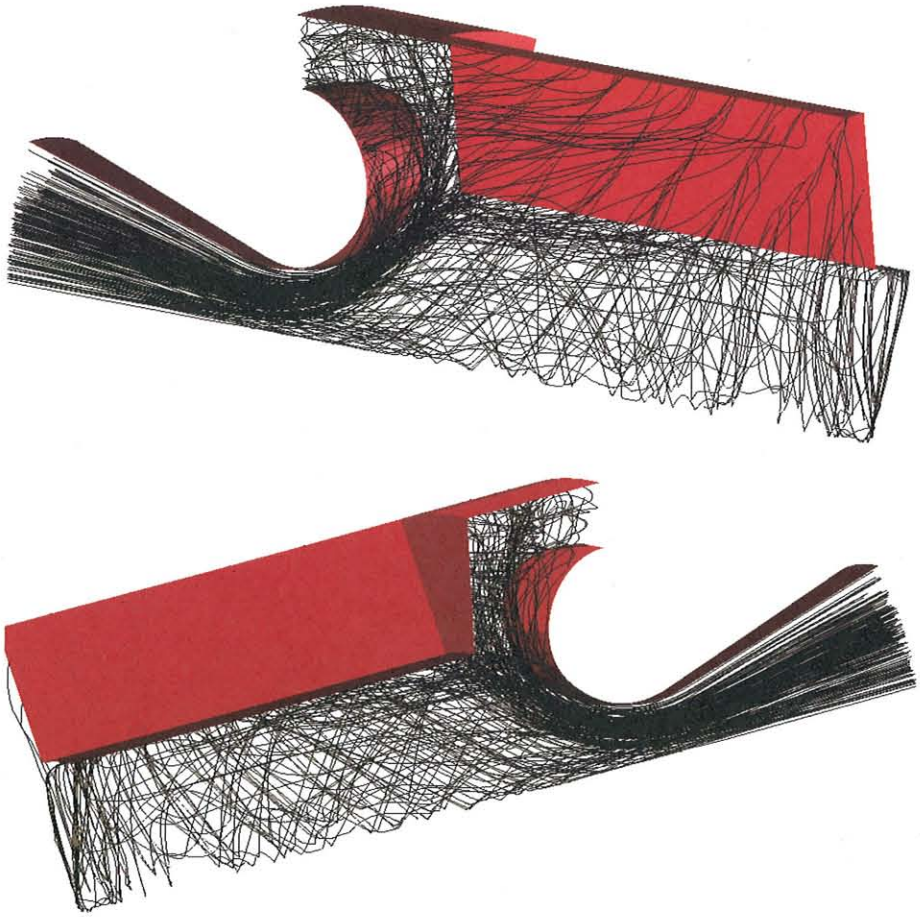

Fig. 163 Particle paths (thinned out)

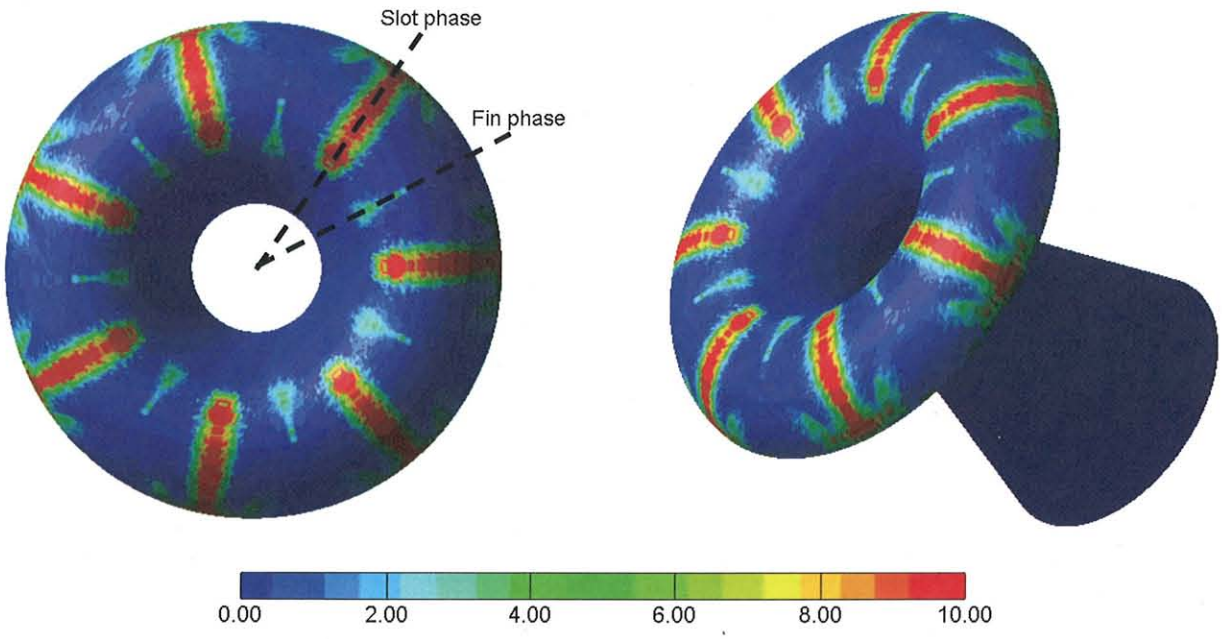

Fig. 164 Mass flux of Lagrangian-phase particles colliding with the nozzle surface, kg/m²/s

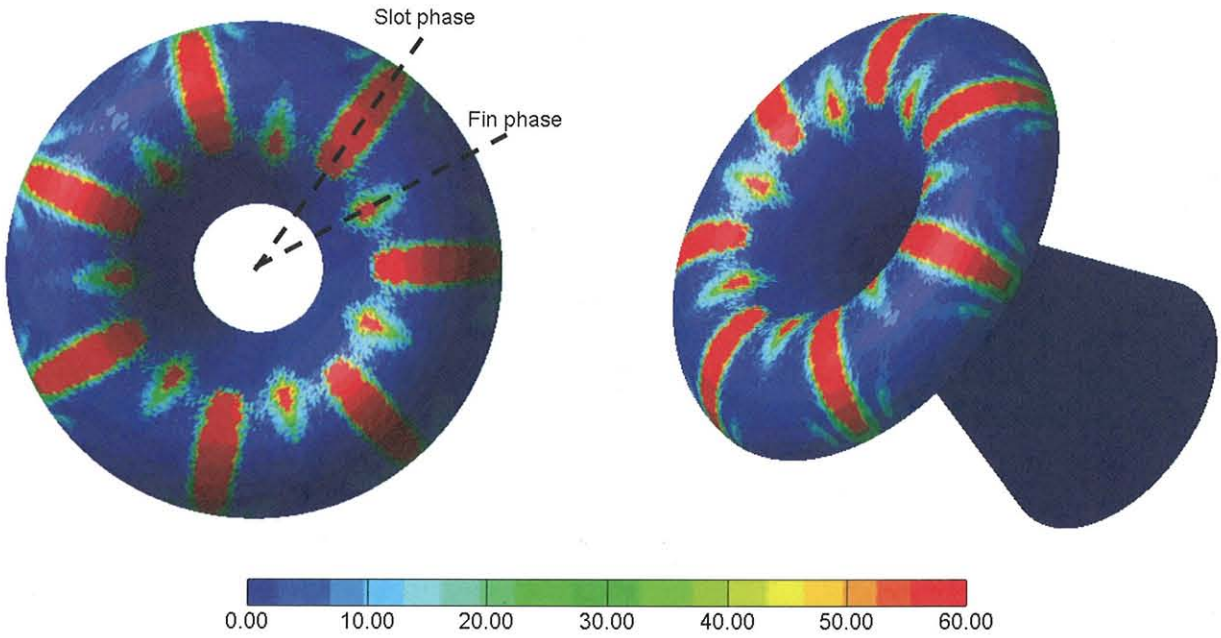

Fig. 165 Momentum flux of Lagrangian-phase particles colliding with the nozzle surface, Pa

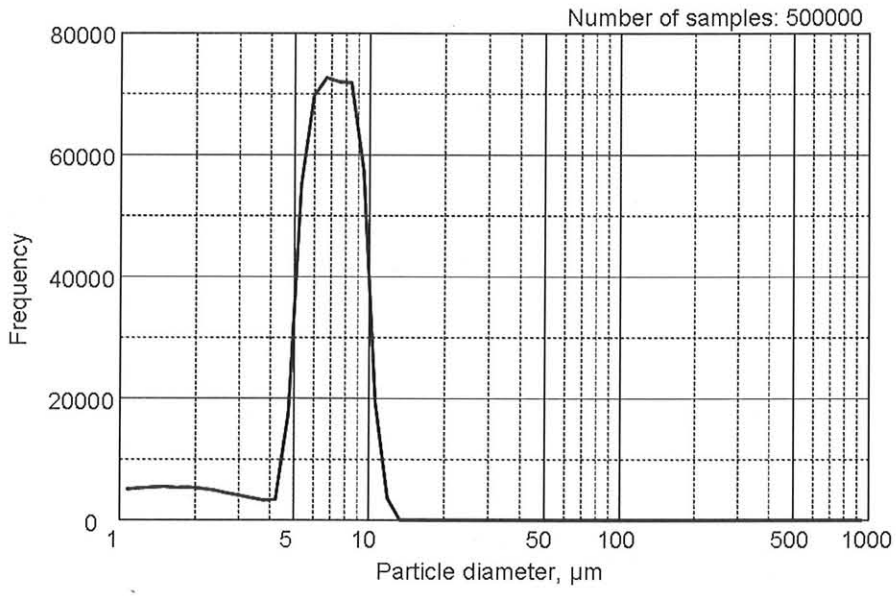

Fig. 166 Diameter distribution of the Lagrangian-phase particles discharged from the nozzle N ≈ 500000)

5. Conclusion

In this booklet the authors have tried to provide practical information on the computational fluid dynamics of the multiphase flows in a solid rocket motor, by describing mathematical models on the forces and the heat transfer to particles in the flow, the computational methods for the multiphase flows, and many numerical experiments on the verification of these models and methods.

As a feature of the multiphase flow in a solid rocket motor, the particle size distribution changes according to the combustion and breakup of particles as they flow from the burning surface to the nozzle exit. It is difficult to perform a

practically meaningful simulation without treating these effects. In this booklet, the Eulerian-Eulerian method, the Eulerian-Lagrangian method, and the Eulerian-hybrid method are explained in detail, and the information is provided towards the construction of more realistic simulation tools.

The authors are pleased if this booklet serves as a reference for engineers and a textbook for students in this field. Since many problems are still left unsolved, the contents of this booklet are due to be updated with the progress of future research.

Acknowledgment

This production is partially based on the result of the collaborative project (FY2002 and FY2003) of former ISAS, NAL and NASDA, which are now united as JAXA.

References

[1] Price, E.W., "Combustion of Metalized Propellants," Fundamentals of Solid-Propellant Combustion edited by Kuo, K.K. and Summerfield, M., AIAA, Progress in Astronautics and Aeronautics, Vol. 90, pp. 479-513, 1984.

[2] Crowe, C., Sommerfeld, M., and Tsuji, Y., "Multiphase Flows with Droplets and Particles," CRC Press LLC, Boca Raton, Florida, Chapter 4 Particle-fluid Interaction, pp. 57-112, 1998.

[3] Schlichting, H., "Boundary Layer Theory," McGraw-Hill Inc., Mar, 1958.

[4] Schiller, V.L. and A Naumann, Z., Vereines Ingenieure, Vol. 77, 318, 1933.

[5] Wen, C.Y. and Yu, Y.H., Chemical Engineering Progress Symposium Series, Vol. 6, p.100, 1966.

[6] Putnum, A., "Integrable form of droplet drag coefficient," ARS Journal., Vol. 31, 1467, 1961.

[7] Clift, R. and Gauvin, W.H., "The motion of particles in turbulent gas stream," Proc. Chemeca '70, 1, 14, 1970.

[8] Carlson, D.J. and Hoglund, R.F., "Particle drag and heat transfer in rocket nozzles," AIAA Journal, Vol. 2, No.11, 1964.

[9] Henderson, C.B., "Drag Coefficient of Spheres in Continuum and Rarefied Flows," AIAA Journal, Vol.14, No.6, 1976.

[10] Crowe, C.T., et al., "Measurement of Particle Drag Coefficients in Flow Regimes Encountered by Particles in a Rocket Nozzle," UTC 2296-FR, United Technology Center, 1959.

[11] Hermsen, R.W., "Review of Particle Drag Models," JANAF Performance Standardization Subcommittee 12th Meeting Minutes, CPIA, 113, 1979.

[12] "Solid Rocket Motor Performance Analysis and Prediction," NASA-SP-8039, 1971.

[13] Ranz, W.E. and Marshall, W.R., "Evaporation from drops - I and II," Chem. Engr. Prog., 48, 141 and 173, 1952.

[14] Kavanau, L. L. and Drake, R. M., Jr., "Heat Transfer from Sphere to a Rarefied Gas in Subsonic Flow," Univ. of California, Rept. HE-150-108, p.9, 1953.

[15] Siegel, R. and Howell, J.R., "Thermal Radiation Heat Transfer, Third Edition," Taylor and Francis, Philadelphia, 1992.

[16] Kliegel, J.R. and Nickerson, G.R., "Flow of Gas-Particle Mixtures in Axially Symmetric Nozzles," Progress in Astronautics and Rocketry, Vol. 6, Academic Press, New York, 1962, pp. 173-194

[17] Hoglund, R.F., "Recent Advances in Gas-Particle Nozzle Flows," ARS Journal, Vol. 32, May 1962, p. 662

[18] Crowe, C.T., Sharma, M.P., and Stock, D.E., "The Particle-Source - In Cell (PSI-CELL) Model for Gas-Droplet Flows," Journal of Fluids Engineering, Vol. 99, June 1977, pp. 325-332.

[19] Chang, I-S, "One- and Two-Phase Nozzle Flows," AIAA Journal, Vol. 18, No. 12, December 1980, pp.1455-1461.

[20] Chang, I-S., "Three-Dimensional, Two-Phase Supersonic Nozzle Flows," AIAA Journal, Vol . 21, No. 5, 1983, pp. 671-678.

[21] Hwang, C. J., and Chang, G.C., "Numerical Study of Gas-Particle Flow in a Solid Rocket Nozzle," AIAA Journal, Vol. 26, No. 6, 1988, pp. 682-689

[22] Lupoglazoff, N., and Vuillot, F., "Numerical Simulation of Nonsteady Two-Dimensional Flows in Solid Propellant Propulsion System," Recherche Aerospatiale, No. 2, 1992, pp. 21-41

[23] Vasenin, I. M., Narimanov, R. K., Glazunov, A. A., Kuvshinov, N. E., and Ivanov, V. A., "Two-phase flows in the nozzles of solid rocket motors," Journal of Propulsion and Power, Vol. 11, No. 4, 1995, pp. 583-592

[24] Bondarchuk, S.S., Vorozhtsov, A.V., Kozlov, E.A., and Feshchenko, Y.V., "Analysis of multidimensional and two-phase flows in solid rocket motors," Journal of Propulsion and Power, Vol. 11, No. 4, 1995, pp. 593-599

[25] Daniel, E., "Eulerian Approach for Unsteady Two-Phase Solid Rocket Flows with Aluminum Particle," Journal of Propulsion and Power, Vol. 16, No. 2, 2000, pp. 309-317

[26] Sabnis, J.S., "Numerical Simulation of Distributed Combustion in Solid Rocket Motors with Metalized Propellant," Journal of Propulsion and Power, Vol. 19, No.1, 2003, pp. 48-55

[27] Cai, W., Ma, F., and Yang, V., "Two-Phase Vorticoacoustic Flow Interactions in Solid-Propellant Rocket Motors," Journal of Propulsion and Power, Vol. 19, No. 3, 2003 pp. 385-396.

[28] Shimada, T. and Sekino, N., "Numerical Simulations of Flows around Re-entry Vehicle and Evaluation of Heating Rate," Special Publication of National Aerospace Laboratory, NAL SP-34, pp. 83-88, 1997.

[29] Shimada, T., Yamamoto, Y., Hirose, N., Ueda, S., and Itoh, K., "Computation of HYFLEX Aerodynamic Heating at HEK Shock-Tunnel Test Conditions," AIAA Paper 99-3493, AIAA 33rd Thermophysics Conference, 1999.

[30] Shuen, J.S. and Yoon, S., "Numerical Study of Chemically Reacting Flows Using an LU Scheme," NASA TM180882, AIAA-88-0436, 1988.

[31] Ikeda, H., Tanno, H., Tokudome, S., and Kohno, M., "Particle Impingement in SRM Nozzles," Proc. of 17th ISTS, 1990.

[32] Nakamura, T., Yagi, H., et al., in Space Transportation Symposium, in Japanese, Institute of Space and Astronautical Science, 2002.

[33] Sekino, N. and Shimada, T., "Eulerian-Lagrangian Approach for Numerical Simulation in Solid Rocket Motors," Proceedings of 24th International Symposium on Space Technology and Science, Miyazaki, Japan, May 30-June 6, 2004, ISTS 2004-a-22, pp.57-63, 2004.

[34] Gordon, S. and McBride, B.J., "Computer Program for Calculation of Complex Chemical Equilibrium Compositions, Rocket Performance, Incident and Reflected Shocks, and Chapman-Jouguet Detonations," NASA-SP-273, 1971. also, Mcbride, B. NASA Center for AeroSpace Information (CASI), LEW-15113, 19940101; Jan 1, 1994.

[35] Hermsen, R.W., "Aluminum Combustion Efficiency in Solid Rocket Motors", AIAA-81-0038, 1981.

[36] Widener, J.F. and Beckstead, M.W., "Aluminum Combustion Modeling in Solid Propellant Combustion Products", AIAA-98-3824, 1998.

[37] Beckstead, M.W., "Modeling Aluminum Combustion," RTO AVT/VKI special course, Von Karman Institute for Fluid Dynamics, May 2002.

[38] Salita, M, "Quench Bomb Investigation of Al2O3 Formation from Solid Rocket Propellants (Part II): Analysis of Data," 25th JANAF Combustion Meeting, CPIA 498 (Vol. I), 1988.

[39] Shimada, T. and Sekino, N., "Numerical Simulation of Internal Multi-phase Flow in Solid Rocket Motor," NAL SP-57, National Aerospace Laboratory of Japan, ISSN 0289-260X, pp.154-159, 2003.

[40] Shimada, T., Sekiguchi, M., and Sekino, N., "Numerical Analysis of Flow inside M-14 Motor with Relation to Nozzle Inlet Ablation," ISAS Research Note, 798, Institute of Space and Astronautical Science, Sagamihara, Nov. 2005.

JAXA Special Publication JAXA-SP-05-035E

Date of Issue : March 31, 2006
Edited and Published by : Japan Aerospace Exploration Agency
7-44-1 Jindaiji-higashimachi, Chofu-shi, Tokyo 182-8522, Japan
URL: http://www.jaxa.jp/
Printed by : FUJIPLANS Co., Ltd.